Integrated AFM-Raman for molecular characterization of peptide nano– and micro– tubes

by Faris Sinjab MPhys. (Hons.)

supervised by Dr. I. Notingher

Thesis submitted to the University of Nottingham

for the degree of Doctor of Philosophy

September 2014

School of Physics and Astronomy

Abstract

This work is focused on exploring a unique integration of techniques, Raman micro–spectroscopy and atomic force microscopy (AFM), which when combined offer more than the sum of their respective parts. The non–invasive chemical specificity afforded by Raman spectroscopy, combined with the nanoscale–resolution topographic imaging of AFM offer much individually.

The physics underlying the practical application of each technique is very general; Raman spectroscopy detects molecular vibrational shifts using light, and AFM uses a physical probe to interact with a surface to provide topographic (and mechanical) information. As a result, there are few restrictions to the possible samples that can be studied with these techniques, from semiconductors and geological crystals, through to simple organic chemical structures all the way to complex biological molecules and systems such as cells and tissue. In this work, a synthetic biomaterial composed of diphenylalanine (FF) peptide units which self–assemble into strong tubular structures is used as a sample of interest when exploring the different possibilities available from a combined Raman–AFM instrument. First, the combined system was set up in order to perform tip–enhanced Raman spectroscopy (TERS), a technique promising Raman spectroscopic imaging at the resolution of AFM imaging. A relatively young technique, TERS has huge potential in extending the reach of Raman spectroscopic imaging to the nanoscale, at a regime where a great deal of structure exists, but is usually blurred by conventional diffraction–limited Raman microspectroscopy. A major focus in this work is addressing a current problem with TERS: the fabrication of suitable probes. TERS typically utilizes

AFM tips modified to have a silver nanoparticle, capable of locally enhancing the Raman signal, attached at the probe apex. A new method is presented here that promises several improvements over existing approaches, as the entire fabrication can be performed *in–situ* on the instrument. Tips produced in this way are then characterized by electron microscopy and tested on FF nanotubes.

Following this, several techniques for the synthesis of silver nanoparticles are explored for use in TERS. Here, the focus is particularly on decahedral nanoparticles, which can be grown into rod shaped particles with well–defined shapes and sizes. These are important considerations for obtaining the desired enhancing properties for TERS probes.

Finally, the AFM-Raman instrument is used to investigate the mechanical properties of FF tubes using several methods. AFM force spectroscopy of tubes suspended across a gap can be used in conjunction with a bending beam theory to measure the Young's modulus of individual tubes. A new type of co–localized experiment using polarized Raman spectroscopy on a suspended tube under various forces from the AFM is tested, and subsequently information relating to the hydrogen bonding network is used, in conjunction with existing X–ray data, to determine the molecular contributions to the modulus using a simple model for amyloid fibrils. Each experiment operates at the single fibril level, with the same fibrils being used, such that different methods can be compared for a single FF tube.

List of publications

- **Faris Sinjab**, Banyat Lekprasert, Richard AJ Woolley, Clive J. Roberts, Saul JB Tendler, and Ioan Notingher. *"Near-field Raman spectroscopy of biological nanomaterials by in situ laser-induced synthesis of tip-enhanced Raman spectroscopy tips."* Optics letters 37, no. 12 (2012): 2256-2258.

- **Faris Sinjab**, Georgi Bondakov, and Ioan Notingher. *"Co-localised Raman and force spectroscopy reveal the roles of hydrogen bonds and $\pi - \pi$ interactions in defining the mechanical properties of diphenylalanine nano-and micro-tubes." Applied Physics Letters* 104, no. 25 (2014): 251905. 2014.

Conference contributions

- **Faris Sinjab**, Banyat Lekprasert, and Ioan Notingher, "*Raman spectroscopy of biological nano-materials*", International Conference on Raman Spectroscopy 2012, IISc. Bangalore, India.

- **Faris Sinjab**, and Ioan Notingher "*Near-field Raman spectroscopy using photochemically prepared nanoparticles as optical antennae*", European Microscopy Congress 2012, Manchester, UK.

- **Faris Sinjab**, and Ioan Notingher "*Combined Atomic Force Microscopy-Polarized Raman Micro-Spectroscopy for Investigating the Mechanical Properties of Biomimetic Fibrils*", International Conference on Raman Spectroscopy 2014, Friedrich–Schiller University, Jena, Germany.

Acknowledgements

Firstly, I'd like to thank my supervisor, Ioan Notingher, for giving me the opportunity to pursue a PhD. He has been a great supervisor, allowing me lots of freedom in the projects I undertook, whilst also pushing me to do the best work I could. I feel that I've developed greatly as a scientist in the past few years under his guidance.

I must also thank the people, past and present, of the Nottingham nanoscience group. Marta was a great friend and helped me find my footing in the lab when I first started, as did Banyat and Claire. Also Kenny, Cristian, and Rich patiently helped me whenever I had a novice question about anything to do with lab equipment. Outside of the labs, Andy, Pete, Dave, Maria, Alex, and many others regularly provided comedy and interesting discussions at tea break, as well as generally being great company.

I also want to thank my long–time friend Eddie as without him I wouldn't have survived my A-levels in order to get here! I also want to thank Hazel who has been a great friend over the years and is one of the best human beings I know.

Also thanks must go to my Mum, Uncle Andrew, and my younger sisters, Amanda and Shereen as well as other family members. While they may not necessarily understand what I "do", they always ask about my work and show great support.

Finally, I want to pay tribute my late grandfather, Michael Davies. He was responsible for sparking my interest in the natural world when I was a child, and was an incredibly kind, unassuming, thoughtful man, who always encouraged me in any endeavor I pursued. I dearly miss him not only as a grandfather, but as a great friend. I dedicate my thesis to him.

. . . "The best thing for being sad," replied Merlin, beginning to puff and blow, "is to learn something. That's the only thing that never fails. You may grow old and trembling in your anatomies, you may lie awake at night listening to the disorder of your veins, you may miss your only love, you may see the world about you devastated by evil lunatics, or know your honour trampled in the sewers of baser minds. There is only one thing for it then – to learn. Learn why the world wags and what wags it. That is the only thing which the mind can never exhaust, never alienate, never be tortured by, never fear or distrust, and never dream of regretting. Learning is the only thing for you. Look what a lot of things there are to learn."

- excerpt from "The Once and Future King" by T.H. White

Contents

1. Introduction

Nanoscale materials are defined as having properties that diverge from the macroscopic norm as one of more dimensions is reduced to typically below one micrometer. In order to investigate the structures at these smaller length scales, a multitude of characterization techniques are needed. The past century has seen the development of a range of specialized techniques for investigating particular aspects of nanoscale materials. Mechanical and topographical information can be obtained from scanning probe microscopies (SPM), electron microscopy offers high-resolution three-dimensional imaging, and a wide range of optical techniques can give detailed spectral information in addition to intensity and phase imaging. As new techniques develop and as technology becomes more sophisticated, the quality of the information obtainable from these techniques should improve, and will subsequently enhance the understanding of materials at these small scales. The limitations of current measurements are constantly being tackled with new approaches, and modifications or combinations of current techniques. The work presented here concerns one such combination of techniques: Raman spectroscopy and atomic force microscopy (AFM). These techniques individually have matured over several decades since their invention to the point where they are well established for characterizing an impressive array of samples across the natural sciences. However the combination of Raman spectroscopy and AFM in particular has great potential for allowing much more than the sum of the individual parts offered by the techniques; entirely new types of experiment can be explored using such a combined system.
Raman scattering is a process whereby an incident monochromatic light source (usually a laser) interacts with the vibrational modes of the molecules in a sample. This interaction can cause radiation of a slightly

shifted frequency from that of the laser to be emitted, which depends on the particular vibrations in the sample. Analyzing the scattered radiation using a suitable spectrometer, a Raman spectrum can be observed, where peaks can be assigned to particular vibrational transitions, giving information on chemical composition and conformation of the sample. When combined with an optical microscope, it is possible to reduce the sampling volume to approximately half the wavelength of the illuminating light. Raman micro-spectroscopy allows spectral imaging of samples such as microparticles, cells and other structures equal to or greater than this length scale. Spectral imaging produces a three dimensional data set, with a full Raman spectrum acquired at each point of a two-dimensional map. While this resolution is sufficient for many samples, there are countless structures with surface chemistry features below this diffraction-limited regime. Raman microspectroscopy on these samples just produces an average of all the nanoscale chemical variations on the surface within the sampling volume, offering no spatial discrimination.

In AFM, a sharp probe is used to detect the surface mechanically, with an electronic feedback system being used to control the distance between probe and sample. Raster scanning the probe across a surface reveals the topography of the surface, with the resolution determined by the convolution of the tip with the sample. In ambient conditions, imaging resolutions of 10nm are regularly obtained. Force spectroscopy an also be carried out, which involves approaching the tip into contact with the sample and pressing until a defined setpoint force is reached. This can give additional information about the mechanical structure of the sample.

The majority of the work presented here concerns the relatively young technique of tip-enhanced Raman spectroscopy (TERS), a combination of AFM and nanoparticle-enhanced Raman spectroscopy. Such a technique allows the simultaneous acquisition of topographic features and vibrational

spectra of materials at length scales far below the typical diffraction limit of visible light. While these techniques have been used individually to much success, AFM by itself lacks the chemical specificity of Raman spectroscopy, and conversely Raman spectroscopy lacks the nanoscale imaging resolution of AFM. The integration of AFM and Raman allows a new type of measurement: the label-free imaging of surface chemistry with nanoscale resolution.

The combination of AFM and Raman spectroscopy in TERS is mediated by the emerging subject of plasmonics, which concerns the manipulation of light at nanometer length scales. Nanoparticles composed of certain metals can produce what is known as a localized surface plasmon resonance (LSPR), where the free electrons oscillate at their resonant frequency which is typically in the UV-visible-NIR spectral region. Radiation with frequency close to this LSPR frequency can induce these oscillations in the nanoparticles, creating strong electric fields close to the nanoparticle surface. The high spatial accuracy of AFM is used to position a single nanoparticle probe capable of LSPR close to a sample, whereby a laser can be used to excite the nanoparticle. The enhanced oscillating field close to the nanoparticle will induce Raman scattering in any materials in close enough proximity. This probe can then be raster scanned to produce an image as in AFM, except that now each image pixel will contain a full Raman spectrum. This means that TERS allows for materials with surface properties that vary at nanometer length scales to be imaged with high chemical specificity.

The label-free non-invasive nature of TERS gives it a broad range of potential applications across a number of disciplines. The focus of the work in this thesis will be towards the investigation of biologically relevant samples, in particular self-assembled diphenylalanine (FF) peptide nanostructures. These structures are used as models for self-assembled amyloid-β fibrils which play a key part in neurodegenerative conditions such as Alzheimer's

disease. The structures formed are also of interest from a materials science perspective as they are mechanically strong and biologically compatible and so may be of use as cell scaffolds in tissue engineering, and for cell membrane transport and drug delivery.

The major factor in all TERS experiments is the preparation of a suitable probe. This has been approached several ways in the literature, resulting in variable success, but low reproducibility of results and a poor yield of working probes. In this study we propose growing nanoparticles at the apex of an AFM tip using simple methods which allow for tailoring properties. Recent advances in nanoparticle synthesis allow highly specific geometries to be obtained, which have thus far not been applied to the fabrication of TERS probes. This thesis will explore a novel method for preparing TERS tips which has many advantages over conventional methods, and has a greater scope for customization and control.

In addition to TERS, the combined AFM–polarized Raman spectroscopy setup is used to investigate the mechanical properties of the FF structures using different approaches at a single fibril level. Polarized Raman spectroscopy (PRS) is a powerful extension to the system, as it not only reveals chemical information, but also the orientation distribution of the vibrational modes. The FF tubes had previously been investigated with PRS (B. Lekprasert PhD thesis [1]), and using two particularly important vibrational modes for peptides, the amide I and III modes, information about the molecular structure was obtained for FF tubes at equilibrium. As these FF tubes are biologically compatible and have impressive mechanical properties, they have great potential as a biomaterial for structures such as artificial cell scaffolds. Thus it is important to be able to measure and understand the origin of its mechanical properties at the molecular scale. The combined AFM–PRS instrument is well placed for such a task, and several approached have been utilized in order to work towards this. First,

a bending beam experiment for tubes suspended across a gap is adapted from the literature to be compatible with the AFM–Raman setup, allowing the measurement of the Young's modulus for a single fibril. Then, for the same tube, polarized Raman spectra can be obtained whilst the tube is subjected to a range of forces from the AFM tip, with the aim of elucidating any spectral changes that may correlate with the applied stress. Finally, a model for the peptide fibrils is used to work out the molecular contributions to the total modulus. Using data from the PRS experiment, and known X-Ray data, the Young's modulus for a single tube can be calculated, and compared with that measured by the bending beam experiment, and other values in the literature.

1.1 Outline

Chapter 2 covers the background literature for TERS, with specific focus on the probes, but also some discussion of basic operational principles and a brief discussion of applications. Following this, methods for nanoparticle synthesis will be introduced, with particular attention paid to methods allowing for control over the size and shape, and thus the optical properties, which is critical for TERS.

Chapter 3 presents the necessary theoretical background for the work presented in the later chapters. First, Raman micro-spectroscopy will be introduced, together with a discussion on the limits of spatial resolution for optical imaging and a brief overview of polarized Raman spectroscopy. This will lead on to the introduction of the plasmonic effects of noble metal nanoparticles, in particular the conditions for producing localized surface plasmon resonances necessary for TERS. This chapter will then end with a brief introduction to the fundamental principles of AFM and force spectroscopy.

Chapter 4 will introduce the first experimental results for novel fabrication of TERS probes. Here, the new method for *in-situ* TERS probes is tested as a proof-of-principle, where the probes are characterized by electron microscopy, and TERS measurements are tested on FF peptide nanotubes.

Chapter 5 will present an experimental investigation into further optimizing the nanoparticle properties. At nanometer-length scales, the optical properties of such materials can vary significantly with changes in size and shape. Obtaining highly reproducible nanoparticles with simple control of such parameters has been reported by several groups. Here, a selection of these methods have been reproduced and studied by UV-vis-NIR spectroscopy and TEM to assess their viability for TERS probes.

Chapter 6 concerns the mechanical measurements and combined AFM-PRS experiments on single FF tube fibrils. This begins with a small literature review discussing what is currently known about the structure and mechanical properties of the FF tubes. Following this, the bending beam experiment is detailed, followed by the co–localized PRS-AFM force experiment. Finally, calculations of the FF tube strength are presented, which are then compared with other measurements.

Chapter 7 presents the conclusion for the work on the integrated system, and suggests future areas in which research can be directed.

2. Literature Review

2.1 Tip-Enhanced Raman Spectroscopy

2.1.1 High-resolution imaging

There are a diverse set of tools available to researchers in nanoscience, ranging from SPM techniques and electron microscopy, to mass spectrometry and vibrational spectroscopy. The combination of these approaches offers a wide variety of information obtainable over many orders of magnitude of length scale, with applications across a broad range of sciences (see Figure 2.1). Individual techniques, however, still have their restrictions, whether it be a limit on spatial resolution or the character of the information being obtained.

A drawback common to many techniques is the irreversible alteration

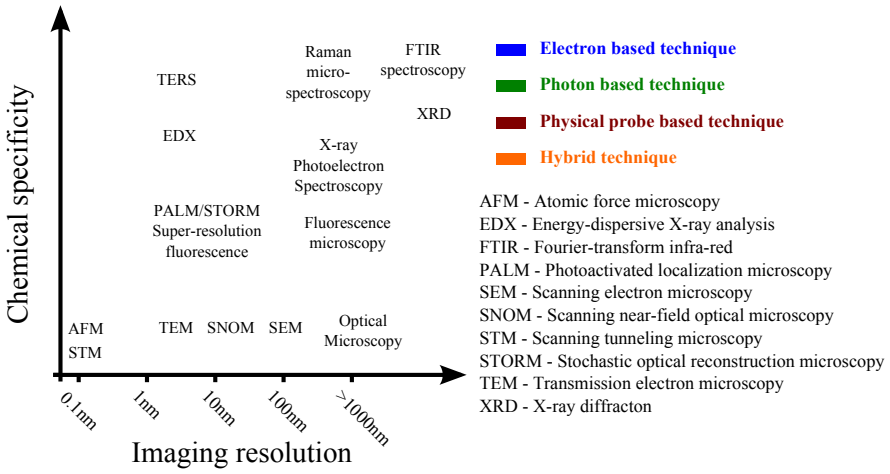

Figure 2.1: Graphical illustration of various techniques and how their chemical specificity and best imaging resolution vary.

of a sample during investigation. This is particularly undesirable in biological studies where, ideally, experiments should be non-invasive so as to observe the system in a relatively unperturbed state. Vibrational spec-

troscopy is a popular choice in such cases as the interaction only involves low-energy molecular vibrations. Raman spectroscopy is particularly useful for biological samples as the water typically found in such systems does not contribute significantly to spectra [2]. Other advantages include fewer restrictions on sample preparation, high chemical sensitivity and specificity, structure-specific conformational information, and the availability of high-power lasers and spectrometers with CCD readouts allowing rapid data acquisition. However, optical microscopy and spectroscopy rely on radiation in the UV-IR range which is typically diffraction-limited to a few hundred nanometers depending on the wavelength (Figure 2.1). Thus these techniques cannot generally be used to spatially resolve nanoscale variations in samples.

SPM techniques (STM and AFM in particular) are required for superior

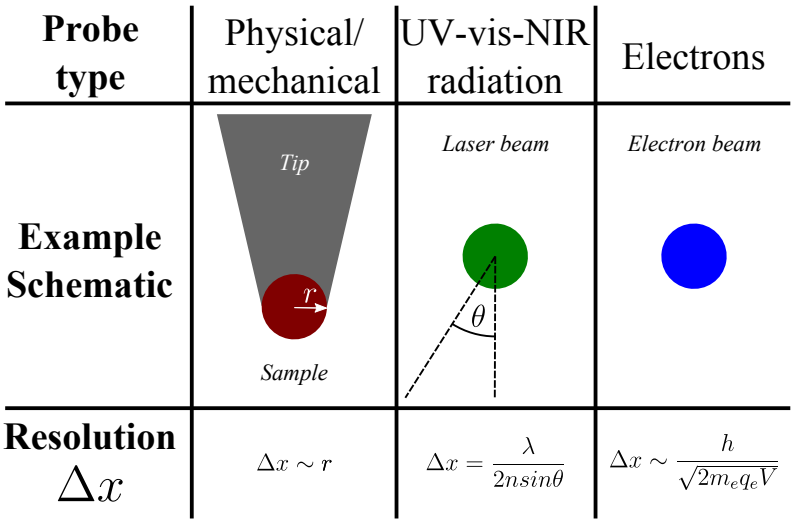

Figure 2.2: Illustration of three general imaging principles common to many techniques. The resolution of scanning probes is usually determined by the tip radius of curvature. The resolution of optical imaging relies on the refractive index of the surrounding material n, the maximum angle from the axis of propagation of the focused beam θ and the wavelength λ. Resolution in electron microscopy is determined by the de Broglie wavelength, which can be written in a form dependent on the electron mass m_e, charge q_e and electric field potential V which is used to accelerate the electrons.

spatial resolution. While topographic images are usually obtained, chemical composition is difficult to determine for complex samples. STM also

requires a conductive substrate which is usually not practical or possible for biological samples. Additionally, SPM techniques are inherently surface specific and often must be prepared to be very flat with surface roughness less than the probe size.

Electron microscopy can attain high resolution imaging with a large field of view. This relies on a beam of high energy electrons which are focused, using magnetic lenses, onto a sample. Imaging contrast depends on the type of chemical element present in the sample. Biological specimens usually have to be coated or treated with heavier elements to enhance contrast.

The techniques mentioned above rely on different physical mechanisms for imaging with different resolutions, portrayed in Figure 2.2. The equation for optical resolution is generally true in microscopy, but is not a fundamental law. Certain techniques allow the diffraction limit to be circumvented by exploiting the ways in which light interacts with matter.

2.2 Nanoscale micro-spectroscopy

One technique for sub-diffraction optical imaging and spectroscopy is far-field super-resolution fluorescence microscopy[3, 4]. The simplest example is stimulated emission depletion (STED) whereby a standard excitation beam is overlapped with an annular depletion beam which quenches fluorescence, thus improving the resolution to the inner region of the annulus as seen in Figure 2.3. Extensions of this idea which essentially perform this switching of fluorescent probes in different ways can be found in [3]. In particular, photo-activated localization microscopy (PALM) and stochastic optical reconstruction microscopy (STORM) are two methods which promise the highest resolutions. These techniques can theoretically image features separated by 1.5nm with the additional capability of three-dimensional imaging. However, prior knowledge about the samples is required as the technique

is fluorescence based[5]. PALM and STORM in particular depend upon the post-processing of the data to obtain their high resolution, not direct imaging.

Electron microscopy can be used to give element-sensitive information

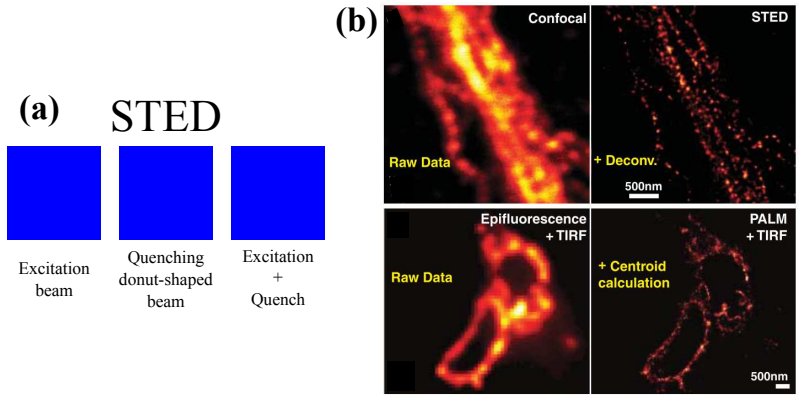

Figure 2.3: Examples of various high resolution fluorescence techniques. (a) Stimulated emission depletion demonstrates the basic idea of reducing the volume in which a fluorescent probe is able to be active. (b) An example of STED and PALM (using total internal reflection fluorescence (TIRF)) imaging of microtubules in a neuron. Image modified from [3].

using energy dispersive X-rays (EDX) analysis. This relies on the X-rays emitted from atoms in the sample due to excitation by the electron beam. This is often expensive, cannot be performed in ambient conditions and samples are often unable to be used further after investigation. High-resolution mass spectrometry techniques also suffer from this problem of irreversible sample damage.

The first combination of SPM and optical microscopy was developed in the 1980s by D. Pohl and colleagues[6], based on an idea several decades before by E.H. Synge[7]. Here, a useful analogy with sound was presented in the form of a doctor's stethoscope, which has the ability to pinpoint the location of the heart to within a few centimeters, even though the sound waves have a wavelength on the order of tens of meters. The optical equivalent consists of a small fiber cable coated in aluminium with a small aperture at

the tip apex through which the scattered near-field radiation could be detected. This technique was termed scanning near-field optical microscopy (SNOM). While typically used for microscopy, variants of the technique attempted optical spectroscopy measurements in the near-field. However, the intensity of the signals obtained from SNOM probes are typically very low, which is a problem for detecting relatively weak processes such as Raman scattering.

Another more recent development utilizing scanning probe techniques for

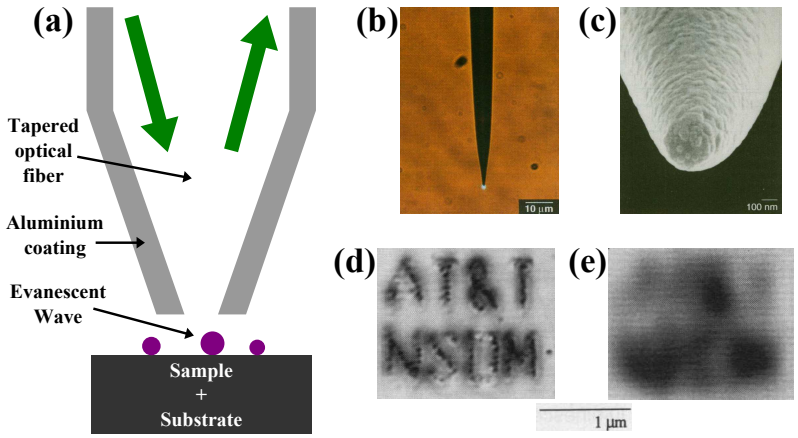

Figure 2.4: Demonstration of SNOM. (a) Schematic of a SNOM tip showing the optical near-field created at the aperture. Optical (b) and scanning electron (c) micrographs of SNOM probes. (d) and(e) show SNOM micrographs of an electron beam pattern, for the probe in near-contact (d) and retracted 400nm (e). Images modified from [8]

optical spectroscopy is the concept of AFM-infrared spectroscopy (AFMIR) [9–11]. Here, an IR laser pulse is directed at the sample via an attenuated total reflectance (ATR) prism and absorbed causing a temporary expansion. The local transient response of the sample can be measured by an AFM tip in contact with the sample. The cantilever deflection measured can be Fourier-transformed to give a spectrum which correlates with corresponding FT-IR spectra. This method relies on the photo-thermo-acoustical properties of the sample, and can be performed using standard AFM tips. While sub-diffraction limited spectral imaging is possible with this technique, the

best current resolution is of the order of 100nm, and measurements are not possible in water (see Figure 2.5).

A similar technique for imaging optical effects at the nanoscale, termed

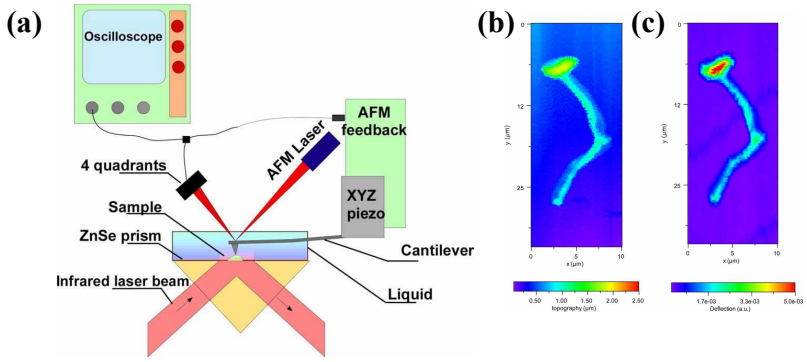

Figure 2.5: Demonstration of AFMIR. (a) Schematic of typical experimental setup. (b) AFM topography of a *Candida albicans* fungi cell and (c) the corresponding AFMIR spectral map for the cantilever response at 57kHz. Image modified from [11].

image-force microscopy (IFM), utilizes the interaction between an optical mirror image created in a tip by an irradiated sample[12] (see Figure 2.6).

Essentially, this technique detects the optical response in the near-field

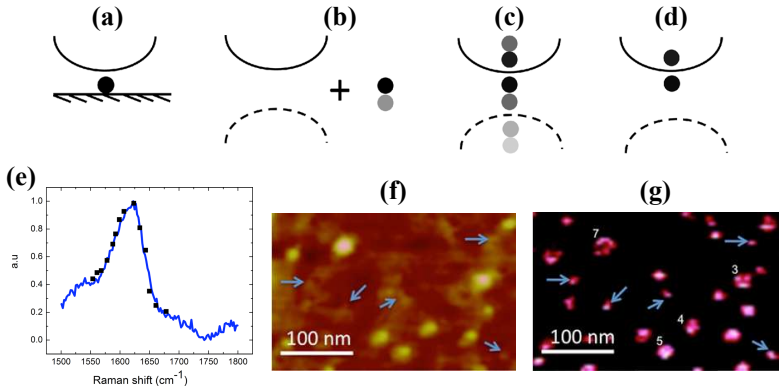

Figure 2.6: Demonstration of image-force Raman micro-spectroscopy. (a) Image and sample which can be viewed as a combination of tip reflection and sample reflection (b). The multiple reflections from the object/image pairs can be approximated as seen in (c), which to first order can be modelled as shown in (d). (e) shows a Raman scattering peak of Coomassie brilliant blue G250 dye molecules on glass from bulk sample (blue) and from IFM detection (black squares). (f) shows a topographic image, and (g) the corresponding IFM Raman image for molecular clusters of the dye. Image modified from [11, 12].

using aperture-less probes, as opposed to the far-field detection in SNOM using apertured probes. This concept has been used to obtain Raman spectra with true nanoscale resolution (see Figure 2.6 (g))[13]. However, full spectra cannot be acquired in one measurement, only individual points corresponding to the laser wavelength used to irradiate the sample. This makes it difficult in principle to obtain Raman spectra with sufficient spectral range, and without prior knowledge of the Raman peak positions.
In order to obtain Raman spectra from sample sizes approaching the single molecule scale, the weak scattering must be enhanced. One technique was discovered by chance by researchers studying molecules adsorbed to silver electrodes.[14] The large Raman scattering signal was attributed to the excitation of surface plasmons at the metal surface. The greatly enhanced local electric field from the surface plasmons typically extends no further than 10-20nm away from the silver surface and is responsible for the dramatic enhancement of Raman scattering. This enhancement of the Raman scattering from very small sample volumes or weak scatterers, known as surface-enhanced Raman scattering (SERS), has become a popular technique for sensing across many disciplines. However, while the sensitivity of SERS is high, the resolution is still diffraction limited.

2.2.1 Introduction to TERS

A novel concept for a technique with high resolution imaging and chemical specificity via Raman spectroscopy was first explored by J. Wessel[15]. Here, an experimental setup was proposed involving a generic optical probe particle controlled by piezoelectric translators (an idea influenced by the then recent invention of STM). Such a particle could probe the near-field of a sample and produce a Raman signal with a gain dependent on the particle material and optical parameters as well as the frequency of the in-

cident laser. This is essentially an inverted SERS experiment with a single, translatable enhancing site. Such a technique fulfills the requirement of non-destructive chemical imaging with nanoscale spatial resolution. One caveat with this method is the restricted axial resolution, which is directly linked to the exponentially decaying enhanced electric field.

In the early 1990s, experimental realisations of Wessel's concept were attempted by the Kawata group using a steel tip coated in Al_20_3[16]. The exponential decay of the evanescent field was measured, but no spectra were obtained as various parameters such as the tip material and sharpness were not optimal. Other attempts at high-resolution Raman spectroscopy were carried out using SNOM instruments, whereby sharpened optical fibers are used as a light source and signal collector[17–20]. While near-field spectra and images were presented, the spatial resolution was typically of the order of 100nm due to the size of the fiber apertures.

The first successful TERS experiments were performed using apertureless

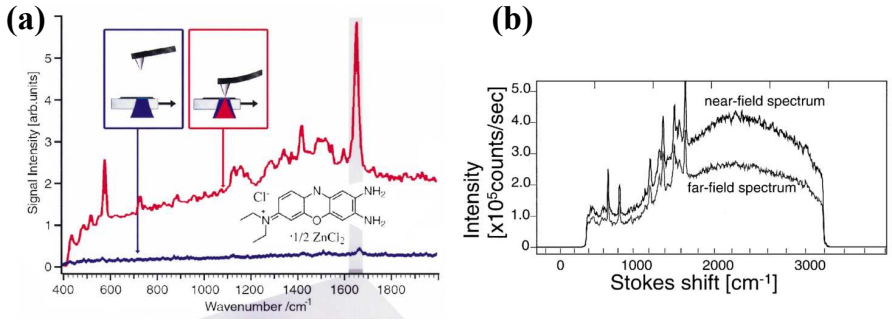

Figure 2.7: Results from the first successful TERS experiments. (a) Measurement of BCB crystals (modified from [21]) and (b) of Rhodamine-6G (modified from [22])

metal-coated probes, and were published in 2000 by the Zenobi group on a brilliant cresyl-blue (BCB) sample[21], M.S. Anderson on sulfur/C60[23] and the Kawata group on rhodamine 6G (R6G)[22]. Anderson presents spectra with the tip approached and retracted, which clearly shows the presence and absence of Raman bands. This technique has since been used for separating far-field Raman scattering from TERS. The results of the Kawata

and Zenobi groups also show near-field Raman spectra, with additional line scans used to estimate the spatial resolution, which was found to be roughly 50nm. The tips used were produced by coating commercial AFM tips with a thin film (10-40nm) of silver or gold. A major consequence of these results was the transition to antenna-like (i.e. non-apertured) probes, as higher spatial resolution and greater enhancement is achievable. Subsequently, TERS experiments has been carried out using various SPM methods, the most popular being cantilever AFM (tapping and contact modes), shear-force tuning-fork AFM, and STM. Early TERS studies focused on simple samples such as dye molecules and carbon nanomaterials, but have gradually incorporated biological systems[24].

In addition to the array of SPM techniques used, the optical setup of

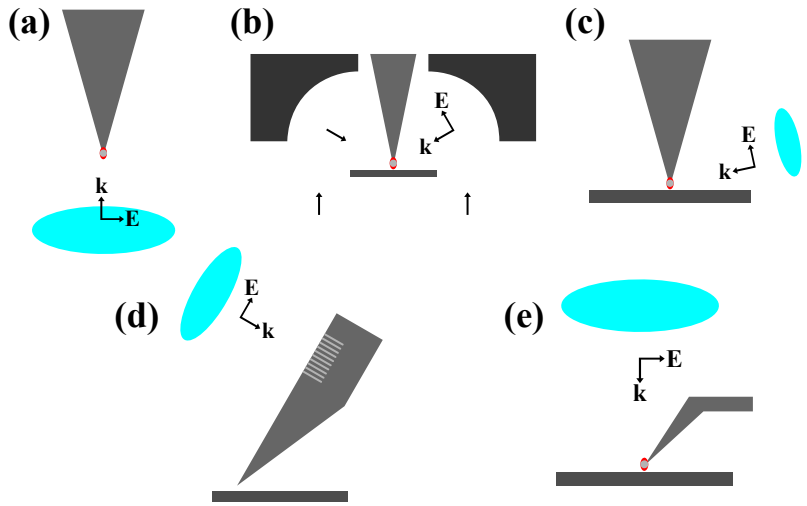

Figure 2.8: Variations in experimental realizations of TERS in terms of the tip-sample coupling setup. (a) Backscattering setup: the Raman scattered light is collected through the same microscope objective as the incident laser. (b) Parabolic mirror setup. (c) Side-illumination setup: allows TERS on any substrate, but requires longer working distance objectives, also the natural geometry for exciting a dipolar LSPR at the tip apex. (d) Grating-tip setup: near-field only excitation removes far-field background. (e) Top–illumination geometry allows opaque samples to be studied using high NA objectives, but requires special AFM probes with outward–pointing tips.

TERS experiments also varies considerably (see Fig 2.8); backscattering and side-illumination using an optical microscope objective are the two

most common, though parabolic mirror configurations have also been used [4,25]. Parabolic mirrors offer large signal collection, but are very sensitive to calibration. Side-illumination has the advantage that the direction of the incident electric field is close to optimal for exciting the dipolar LSPR mode at the correct orientation for a linearly polarized beam (assuming a spherical particle at the tip apex). Transmission setups, however, offer greater signal collection due to availability of high numerical aperture (NA) objectives, but this is restricted to transparent samples. High N.A. objectives also solve the polarization dependence of the plasmon resonances as the high collection angle ensures that some of the incident light has polarization along the tip axis. The proportion of axially polarized incident light can also be increased further with the use of a radial polarizer, which is a common inclusion in many TERS systems[26]. Top–illumination is another possible geometry which allows the possibility of high–NA objectives, as in the backscattering geometries, together with the compatibility of opaque samples.[27] This requires a special class of probes, where the tip axis is not perpendicular to the cantilever, but at an angle such that the apex is accessible from above. A different method which has been suggested utilizes advances in plasmonics for creating a near-field light source in a metal tip by forcing a plasmon created at a grating further up the tip (Fig 2.8(d))[28]. This method would completely remove the far-field background, but requires sophisticated techniques for fabricating the tips. While such probes have been fabricated and studied, few TERS experiments have been demonstrated using such probes thus far[29,30].

While experimental setups vary considerably, all share one common feature: a tip exhibiting localized surface plasmon resonances (LSPR) used to enhance the Raman signal in a volume in close proximity. This enhancement mechanism is predominantly electromagnetic in origin and is responsible for a majority of the enhancement. However, there is also thought to be some

contribution from chemical charge transfer effects if the tip and sample are in close enough contact. The electromagnetic effect has three components: the LSPR mode, lightning-rod effect and antenna resonances[4]. The LSPR contribution has been mentioned already, the lightning-rod effect results from the sharp (or high-curvature) geometry which results in the "bunching" of electromagnetic field lines, and the antennae effect results from resonances that occur due to matching between the wavelength of the incident radiation and the size of the nanoparticle[31]. The lightning-rod effect increases the sharper the tip apex is, while the antenna effect can be ignored for structures which are not half-integer multiples of the wavelength. The LSPR contribution is often of primary importance as it is the most generally applicable and contributes the greatest to the overall enhancement. The properties of the LSPR depend on the dielectric properties of the tip material (and also the surrounding material), as well as the shape and size of the tip apex. These can be controlled during the fabrication of TERS probes to try to match the LSPR frequency to the laser frequency to maximize coupling and thus enhancement. The dielectric properties of the underlying substrate have been shown to be important for determining the exact enhancement volume[32]. A metallic substrate (gold is often desirable for low surface roughness) can also be chosen to further enhance the Raman scattering in a technique known as gap-mode TERS[33].

Estimations of the enhancement vary over many orders of magnitude [34] and are usually calculated experimentally from the difference between spectra when the tip is approached and retracted. When the appropriate scattering volumes are taken into account, an enhancement ϵ_F can be calculated by

$$\epsilon_F = \frac{I_{app} V_{spot}}{I_{ret} V_{tip}} \tag{2.1}$$

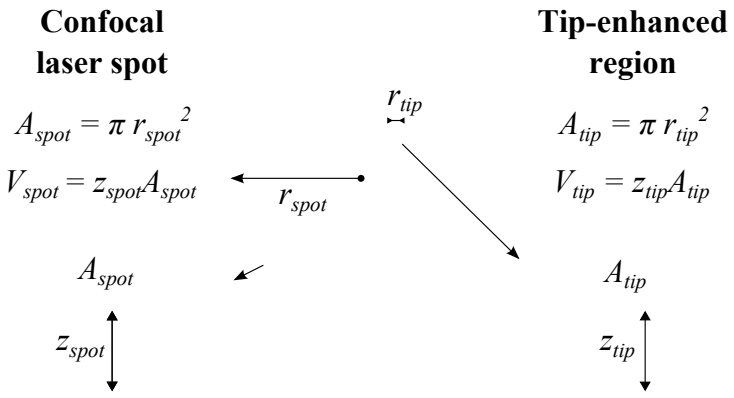

Figure 2.9: Schematic of the simple model used to calculate the enhancement factor from a TERS measurement. Examples of typical values are $r_{spot} = 500nm$, $r_{tip} = 10nm$ and $z_{tip} = 5nm$ (z_{spot} depends on the thickness of the sample).

where I_{app}/I_{ret} corresponds to the ratio of intensities between approached and retracted spectra (usually taken from the area of a particular band), V_{spot} is the volume of the sample in the diffraction limited laser spot, and V_{tip} is the estimated enhancement volume at the tip. This equation assumes both approached and retracted spectra have the same acquisition time and the sample was unchanged during both measurements.

As the sample volume is typically small, temporal fluctuations have been reported not just in TERS, but also in single/few molecule SERS studies [5,35] and thought to be due to diffusion of small particles in and out of the enhancement region. This is likely to always be a problem for experiments performed in ambient conditions, though it can be reduced by maintaining a clean sample surface. Other problems include sample heating and nonlinear optical effects due to the large electric field which can effect or even destroy the sample[36].

2.2.2 Preparation of SPM tips for TERS

The most important aspect of any TERS experiment is the tip. As mentioned, a tip must exhibit a LSPR at the apex in order to provide suitable

enhancement. Tips coated with silver and gold are almost exclusively used due to their unique optical properties. As will be shown in section 3.3, silver tips offer a greater enhancement over the most desirable spectral ranges, though they suffer from rapid degradation and lack of commercial availability. Gold tips are commonly used for experiments on carbon nanotubes and other relatively efficient Raman scatterers, but lack the high enhancement for investigating weaker scatterers, such as biological materials.

With the aim of improving TERS tips, simulations of enhanced elec-

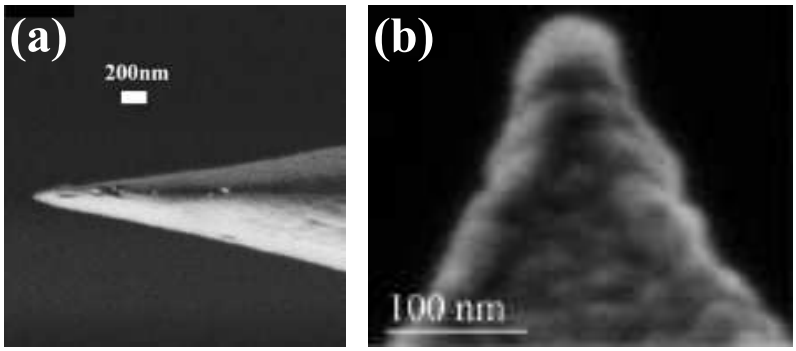

Figure 2.10: Electron micrographs of TERS tips prepared by (a) electrochemical etching and (b) chemical vapor deposition (modified from [5])

tric fields around metallic tip-geometries have regularly been seen in the literature. For the geometries relevant to TERS, solutions to Maxwell's equations are difficult to solve analytically, thus computational methods are preferred. Finite element (FE) simulations are frequently used in such cases, where the problem space is split into discrete segments of as simple geometry in which the equations are solved such that the boundary conditions between the elements are satisfied. This allows the field distribution to be investigated for complex structures and for different materials. These methods can be used to great use, one example being the previously mentioned substrate dependencies[32]. Such studies are useful tools for optimization of the tip structure and investigating enhancement for comparison with experiment.

The two most common methods for preparing TERS tips are electro-

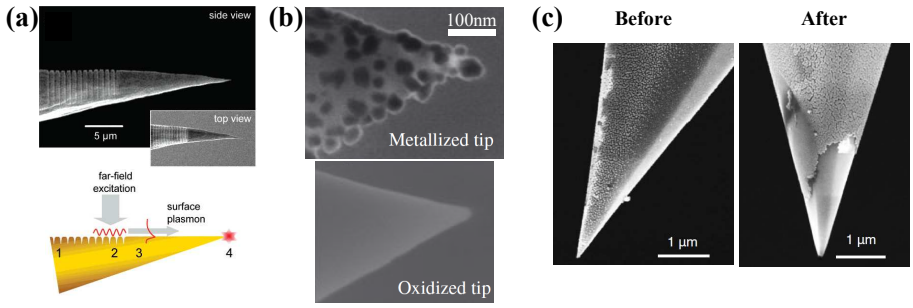

Figure 2.11: Recent advances in tip-fabrication. (a) Surface-plasmon grating tips allowing far–field background–free TERS [29], (b) reproducible oxide-protected metal tips [37], (c) solid silver AFM tip and cantilever before and after a TERS experiment [38]

chemical etching (ECE) of gold/silver wires or chemical vapor deposition (CVD) of the desired metal onto commercial probes. Examples of these can be seen in Figure 2.10. While ECE methods can be reproducible [39], such tips are typically only usable in STM or shear–force AFM systems. For CVD of gold/silver onto commercial AFM tips, a major problem with these preparation methods is the yield of tips which produce an enhanced Raman spectrum. The success rates for tips produced by CVD are typically quite low, and explanations as to how to prepare reproducibly active tips often lack sufficient detail.

Other new approaches have been suggested, a selection of which are seen in Figure 2.11. As shown in Figure 2.8 (d), a grating on a metal tip can be used to produce a background-free plasmon resonance at a tip apex. Figure 2.11 (a) shows both a schematic and electron micrographs of such tips. The schematic shows how far-field excitation at the grating can be used to induce surface-plasmons along the edge of the tip, which will bunch at the apex, effectively creating a near-field radiation source. While the spectral range of the near-field radiation was much broader than the lasers typically used for Raman spectroscopy, TERS measurements were shown from dye molecules with narrow absorption ranges[29].

A high-yield approach using commercially available probes has also been

demonstrated which involved thermally oxidizing silicon tips to silicon dioxide, which are then coated with silver by CVD[37]. The silicon dioxide blueshifts the plasmon resonance of the tips so that it matches the wavelength of the incident laser. A yield close to 100% was demonstrated by performing TERS imaging on carbon nanotubes, with tips producing an enhancement factor greater than 100×. While the plasmon resonance can be controlled by the tip material, there is still the lack of control over the particle shape at the apex inherent to CVD techniques.

Another approach involves fabricating an entire AFM cantilever-chip from silver[38]. This could be advantageous as the tip apex will always be silver, even as it degrades through the course of an experiment, as seen in the before/after SEM images in Figure 2.11 (c). However the problem of controlling the plasmon resonance or tip-apex shape remains.

Most TERS experimental results are generally obtained by a trial and error process with prepared tips. Additionally, the enhancement a particular tip will produce is an unknown factor prior to experiments and can vary significantly. If TERS is to be used as a rigorous technique, the development of standardized, reproducible tips with a reasonably well understood enhancement is crucial. Ideally, such tips should also be simple to fabricate with a low cost. The aim of the work presented in here is to tackle this problem with a novel *in-situ* preparation method.

2.2.3 Applications of TERS

One of the great strengths of TERS is that it is particularly well suited for investigating a wide range of samples across physics, chemistry and biology. Any material that can be studied by AFM and Raman micro-spectroscopy can, in principle, also be studied using TERS. Investigations of TERS as an instrument utilize samples that are tailored to test particular aspects of the technique such as enhancement factor or spatial resolution. Accordingly,

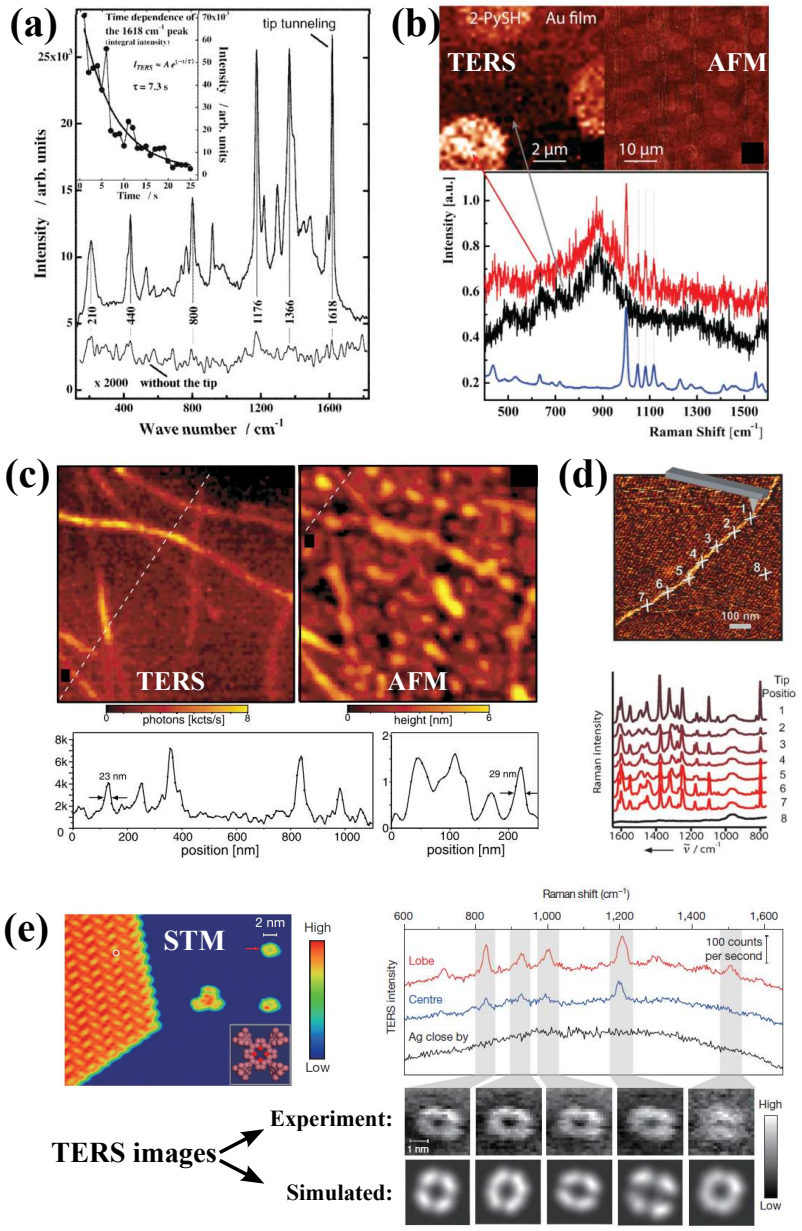

Figure 2.12: Examples of TERS applications. (a) STM-TERS spectra of malachite green isothiocyanate on gold(111) (modified from [40]), (b) TERS and AFM maps on contact printed 2-mercaptopyridine (modified from [41]), (c) Comparison of TERS and AFM on carbon nanotubes (modified from [42]), (d) AFM image with corresponding TERS spectra on a single DNA strand (modified from [43]), (e) Single-molecule STM and TERS images of H2TBPP (modified from [44])

samples which have a low Raman scattering cross section or which have a low concentration are useful for testing the enhancing power, while samples with structure on the scale of a few or tens of nanometers are used when

testing the spatial resolution. Popular samples for the latter include carbon structures[34, 42, 45–47] and nanocrystals (adenine and diamond), while for the former, typical analytes include thiol monolayers (e.g. 4-aminothiophenol (pATP), p-thiocresol[48], 2- and 4-mercaptopyridine (2- and 4-PySH)[41]) and dye molecules (brilliant cresyl-blue (BCB)[21], Rhodamine 6G (R6G) [22], and Malchite green (MG)[40]. Polymer blend thin films have also been studied[49].

Recent studies in STM-TERS has allowed for sub-molecular resolution imaging, as seen in Figure 2.12 (e) for a meso-tetrakis(3,5-ditertiarybutylphenyl)-porphyrin (H2TBPP) sample. This is possible by the creation of a broadband nanocavity plasmon between the sample and tip, which essentially acts as a pump-beam in a stimulated Raman process. This nanocavity plasmon is localized to a much smaller region (the order of a few angstroms) than a typical LSPR of a 10-20 nm sized particle, which explains the drastic improvement in resolution compared with traditional TERS experiments. The nanocavity depends strongly on maintaining an accurate tip-sample separation, which makes STM control necessary, limiting it's application to flat samples on conducting substrates. However, this new approach has expanded the possibilities for TERS, allowing optical spectroscopic imaging of single molecules, and potentially even Raman measurements of single bonds.

Although as a technique TERS is still at an early stage, investigations have been performed on more complex systems than those mentioned above. Of particular interest are biological samples such as cell membranes, viruses, DNA and other protein structures. The ability to resolve vibrational spectra at the nanoscale from such structures offers a great deal of potential information to be gained. The first attempt at using TERS on a cell membrane was published in 2008 by the Deckert group[50], in which the point spectra on and off the cell were taken, showing different Raman bands ap-

pearing when the tip was approached to the cell. The same group have also investigated the viability of TERS as a tool for direct sequencing of a single DNA strand[43], investigating hemozoin crystals formed on blood cells caused by malaria[51], and studying single viruses[52]. Other groups have also investigated single strands of collagen and insulin fibrils[53,54], synthetic lipid bilayers[55] and protein-mineral interactions[56]. These methods

While these experiments are pioneering, they are still being performed using a technique which has unresolved instrumental issues. The main problem is that the majority of the literature in this area originates from a handful of research groups due to their experience with the technique. This is not surprising given the difficulty of the technique when applied to a complex sample and makes it difficult for other laboratories to repeat results. One inter-laboratory study has shown some agreement between different groups, but unexplained discrepancies were still present[57]. Many of these problems are likely to originate from the tip preparation.

2.3 Shape- and Size-Controlled Nanoparticle Synthesis

2.3.1 Stages of seed-based nanoparticle synthesis

A nanoparticle is usually defined as "a particle which has size or shape dependent properties". In the case of metallic and semiconductor nanoparticles, the optical properties can change considerably from those of the bulk for particles of size below around 100nm. Such phenomena can often be observed in unexpected places, such as the colors of the famous Roman Lycurgus cup, and the vibrant colors in stain glass windows[58]. The first experimental investigations into the properties of gold colloids were carried out by Michael Faraday[59], and were explained theoretically by Gustav Mie in 1908[60]. Mie's theory allowed extinction calculations (the combination

of absorption and scattering), from which certain properties of the particles could be determined. However, due to the nature of the sizes of the particles under study, experimental measurements of the precise structure of individual colloidal particles were difficult to obtain until the invention of high resolution electron microscopy. Transmission electron microscopy (TEM) today is able to image with Ångstrom resolution, and has been of great importance for investigations into the structure of small metal particles.

Gold and silver particles are of particular interest because of their unique electrical properties, which allow for the strongest plasmonic response for visible light. Plasmonics essentially allows for the manipulation of light across distances below the diffraction limit of the radiation being used. This may have applications in nanoscale electronics, metamaterials, and chemical sensing, the latter of which will be of importance here.

For sensing purposes, the plasmon resonances of nanoparticles can be used in several ways. For example LSPR spectroscopy[61], whereby a change in the refractive index of a material can be detected by measuring a shift in the extinction spectrum, and enhanced Raman spectroscopy allows spectra to be obtained from very small sample volumes. For these studies in which ensembles of nanoparticles are used, the precise shape of the particles and their interaction typically has little importance for sensing purposes, as a wide range of shapes and sizes will suffice to obtain results. However, TERS uses a single particle for enhancement, thus the shape and size of the particle is critical.

As discussed in the previous section, the most common TERS probes are fabricated either by etching metal wires or evaporating metals onto AFM tips, with the aim of obtaining a single spherical particle at the apex. These methods offer little scope for customization and control; one can vary the thickness of the evaporated metal or change the electrical etch-

ing parameters, but there is no direct way, other than to attempt a TERS measurement, to verify whether the probe is suitable for use.

Solution-based synthesis of metal nanoparticles are popular as they can

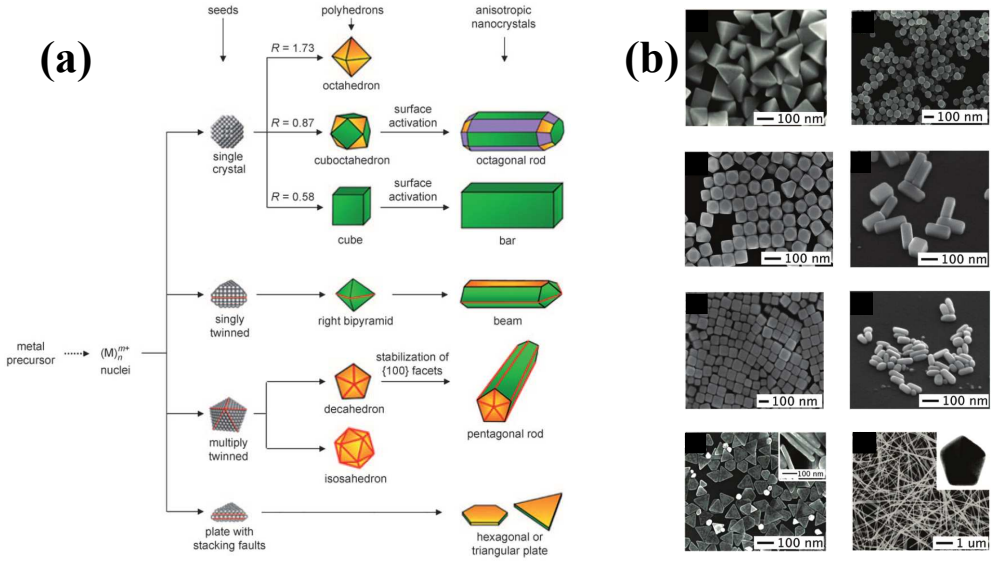

Figure 2.13: Controlled nanoparticle synthesis. (a) shows the possible growth pathways for f.c.c. metal structures. (b) shows example TEM images of mono-disperse silver nanoparticles of different shapes (images modified from [62, 63])

produce large quantities of nanoparticles using relatively simple equipment. A common route for obtaining specific nanoparticle geometries is to use a seed-mediated approach, which involves controlling the structure of the nanoparticles from very early on in the nucleation process. As seen in figure 2.13, several stages are involved in the formation of the final nanoparticle, the first of which is the creation of a seed which will then preferentially grow into a well defined nanoparticle shape (see figure 2.13). Using this basis, highly monodisperse nanoparticle solutions can be fabricated. The prospect of growing nanoparticles with specific geometries at the apex of an AFM tip is highly desirable for TERS.

The growth at each stage relies on the addition of silver ions from the solution, which are usually provided by a silver salt (commonly silver nitrate: $AgNO_3$). When dissolved in high purity water, the salt will form an ionic

liquid of Ag^+ and NO_3^-. If a reducing agent (such as sodium borohydride) is added, the silver ions will become electrically neutral and can aggregate to form a crystal. To avoid the complete aggregation of all the silver in the solution, a protective "capping" layer can be used which adsorbs to the surface of silver particles. Often, the same chemical which is used to reduce the silver ions can also be used to protect the particle.

2.3.2 Selecting the growth pathway

In figure 2.13, it should be noted that the crystallinity of the seed is key to the formation of the end product. However, the nanoparticle surfaces must also be stabilized to prevent aggregation. This is commonly achieved by using organic molecules adsorbed to the surface of the particle. A common chemical used is sodium citrate, which acts both as a reducing agent for the silver ions in solution, as well as the protective capping layer.

Empirical observations suggest that different capping agents can be used to protect different facets of the nano-crystals. This selective adsorption can be used as an additional mechanism for controlling the final nanoparticle shape. Gold and silver are face-centered-cubic (f.c.c.) metals in bulk, but at nanoscale length scales certain structural defects can be favorable. In particular, planar defects in which adjacent crystal planes are mirrored are commonly seen in what is commonly known as a twin-defect. Singly and multiply twinned particles, constructed from single crystals, can be more energetically favorable in the appropriate conditions. Typically the equilibrium shape of a crystal can be determined using the Wulff construction. This process essentially finds the geometry required for the minimum Gibbs free energy of the total surface. A modified Wulff construction which takes into account particle twinning was introduced by Marks and Howie, and used to explain observations of small f.c.c. metal particles with five-fold symmetry[64, 65]. The conditions for the formation of multiply-twinned par-

ticles relies on the balance between the energy of forming a planar twinning defect, and the surface energy of the particle.

The surface energy difference between the {100} and {111} facets of f.c.c.

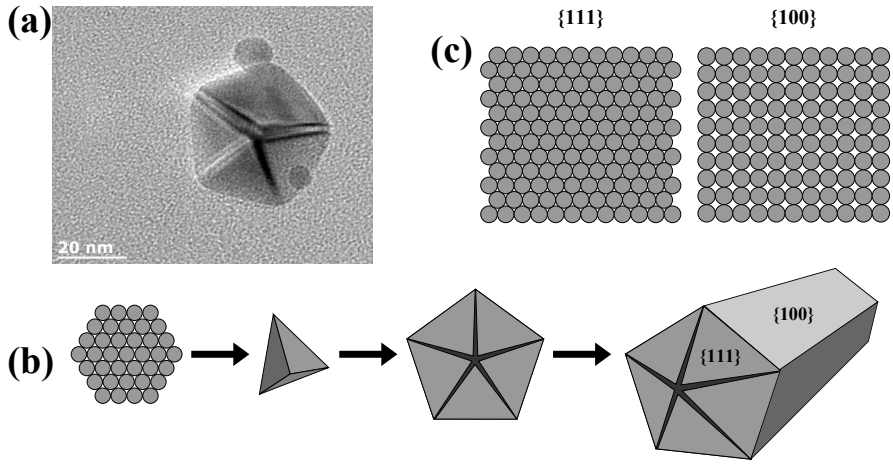

Figure 2.14: Decahedral-seeded nanoparticles. (a) shows a TEM image of a single pentagonally twinned silver nanoparticle. Diffraction from the twinning planes can be seen clearly. (b) Schematic for the stages of the formation of the decahedra, from small single crystal particles, to single crystal tetrahedra, which form twinned-planes to make a single decahedral particle. The selective growth of the decahedra along the five-fold twinning axis produces nanorods with different f.c.c. crystal faceting at the edges and on the sides. (c) shows the f.c.c. 111 plane from above having a hexagonal close-packed structure, while the same view of the f.c.c. 100 plane shows it has cubic packing.

metal could be used to allow preferential binding of surfactants. As seen in figure 2.14 (c), the {111} facet will have a hexagonal close packed (hcp) structure, while the {100} facet will be cubic, which implies the {111} surface will have a lower free energy as the surface atoms pack together more efficiently. This is indeed the case, and for silver the value for the surface energies is $\gamma_{\{111\}} = 0.533$ eV per atom and $\gamma_{\{100\}} = 0.653$ eV per atom[66]. This is a small difference, but it has been found to be sufficient for certain molecules to discriminate between the two surfaces, and preferentially adsorb to one over the other[62,63,66].

Particles with a five-fold twinning symmetry, composed of five tetrahedral particles forming an overall decahedral shape (pentagonal bipyramid, see figure 2.14), have been known to exist since the first electron microscopy

studies on metallic nanoparticles[64]. As shown in figures 2.13 and 2.14, they can be regrown to form nanorods as a consequence of the anisotropy of the initial decahedral particle. The crystal facets at the ends of the rod will differ from those along the side, with the former being composed of {111} facets, and the latter {100} facets.

In the greater context of TERS, a suitably oriented nanorod attached to the apex of an AFM tip would maximize the lightning rod effect, while also allowing tailoring of the LSPR frequency simply by adjusting the size of the particle. While it is possible to form nanorods using other seed-based methods, the unique surface properties of the five-fold twinned particles offer a greater scope for control.

2.3.3 Synthesis of nanorods based on decahedral seeds

As mentioned, sodium citrate is commonly used as a protective cap for nanoparticles. However it is also thought that it preferentially binds to {111} silver surfaces rather than {100}[63]. For the {100} surfaces, a variety of substances can be used. The most common of these is polyvinylpyrrolidone (PVP) which Sun et. al. first introduced in the polyol reduction method for fabricating rods based on decahedral seeds, where ethylene glycol was used as a reducing agent (see figure 2.15(a)) [67].

Further work was carried out by Pietrobon et. al.[68] who prepared monodisperse decahedral particles with greater control over the shape and size[68], and then using these as a seed to regrow into pentagonal-twinned rods as seen in figure 2.15(b) [69]. The thickness of the rods could be controlled by adjusting the size of the starting decahedral seeds, which were prepared photochemically with high yield. The length of the rods was controlled by the time in which the thermal regrowth process was allowed to continue, assuming an appropriate supply of silver ions in the solution.

A similar method which utilizes the same photochemical preparation for

producing decahedral particles, but using high power LEDs was demonstrated by Zheng et. al.[70] (whereas Pietrobon et. al. utilized a high powered lamp with various filters). Another similar method was introduced by

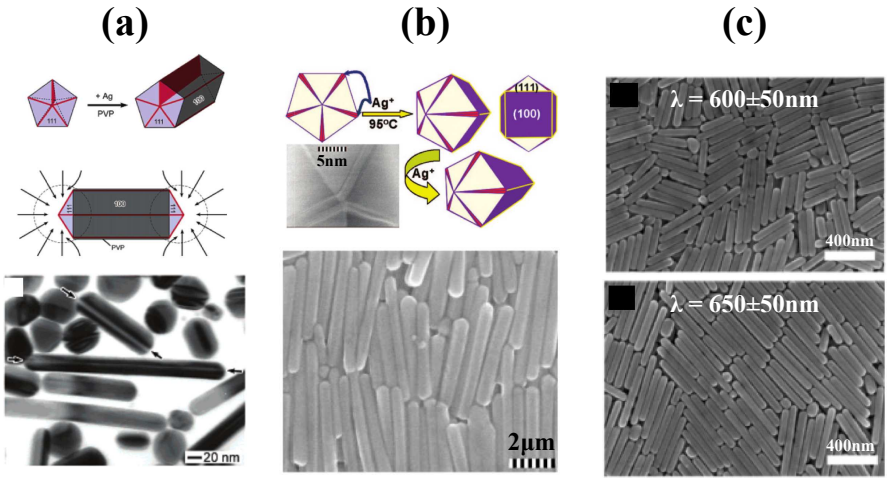

Figure 2.15: Results from various techniques for preparing pentagonal nanorods: (a) The polyol thermal reduction method (Sun et. al. [67]). (b) Thermal rod growth with photochemical decahedral seed preparation (Pietrobon et. al. [69]). (c) Photo-induced rod growth using low energy visible light (Zhang et. al. [71]).

Zhang et. al. (shown in figure 2.15(c) relied on a purely light-mediated method, but which retained the same conditions for decahedral twinned seeds, and regrowth into rods[71]. Here it was shown that, using the appropriate capping agents, high intensity light can initiate the regrowth reaction to produce rods. It was also found that the aspect ratio of the final particles increased with longer wavelength. While this method offers less control over the final shape compared to the method given by Pietrobon et. al., the purely light-based approach avoids the effects of high temperature synthesis. The light-mediated methods also offer potential for development of a system whereby nanoparticles can be grown using light, for example the laser used in the Raman instrument and at relatively small volumes, such as at an AFM tip apex.

3. Theory

3.1 Introduction

The interaction of electromagnetic radiation with materials produces a plethora of physical phenomena. We are most familiar with the visible spectrum and regularly observe effects such as reflection, refraction and scattering and absorption. A majority of phenomena that fall into these categories can be described with classical electromagnetic theory and ray optics, where macroscopic material parameters, such as the refractive index, can be used to describe the interaction with the material.

However there are some effects which require quantum mechanical treatment of the atoms and molecules in a material for a complete description. Raman scattering and fluorescence emission are examples where the frequency of the scattered light will be different to that of the incident beam. These effects are due to transitions between discrete electronic and vibrational molecular states. If the frequency-shifted scattered radiation from these processes is collected and analyzed, a great deal of information can be obtained about the nature of the material.

This chapter first addresses Raman spectroscopy, which will be the central technique used in this work. A derivation explaining the cause of the shifted wavelengths in the scattered/emitted radiation followed by a brief discussion on the intensity dependence of the scattering will be given. Following this, the combination of Raman spectroscopy with a confocal microscope system will be discussed, including the ultimate resolution that can be achieved using far-field optics. Subsequently, the theory behind the plasmonic properties of metal nanoparticles will be introduced, specifically the enhancement of the electromagnetic fields utilized in Raman spectroscopy.

The optical properties of small metal particles will be discussed, particularly the effects of scattering and absorption from such structures. The final section will give a brief introduction to atomic force microscopy in ambient conditions.

3.2 Raman Micro-spectroscopy

3.2.1 The Raman Effect

The molecular vibrations in a material depend on the elemental composition and types of bond present in it. Studying the vibrational properties of materials can allow these properties to be inferred. For many molecules, a particular vibrational mode can be approximated by a simple harmonic oscillator. Taking an ensemble of these molecules, one would expect the distribution of energies to vary according to the Boltzmann distribution, with the most favorable state being that with the lowest energy. It can be

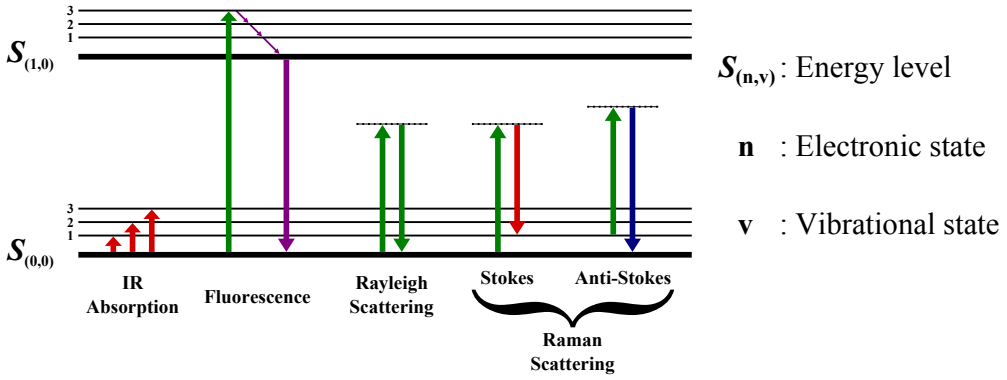

Figure 3.1: Jablonski energy diagram of several absorption and scattering processes for UV-NIR radiation. Dotted lines indicate virtual states. $S_{(n,v)}$ is the energy level, where n and v correspond to the electronic and vibrational levels respectively. Infra-red absorption increases the vibrational state such that $S_{(0,0)} \rightarrow S_{(0,+v)}$, where $v = 1, 2, 3....$ Fluorescence involves transitions to another electronic state, in which non-radiative decays occur. Subsequently the system decays back to the ground state, releasing radiation over a spread of wavelengths. Rayleigh scattering involves no change of energy, but the outgoing radiation is scattered in a different direction to the incoming radiation. Raman scattering involves a change in the vibrational number v such that $S_{(0,v)} \rightarrow S_{(0,v+1)}$ or $S_{(0,v)} \rightarrow S_{(0,v-1)}$, termed Stokes and Anti-Stokes respectively.

seen in figure 3.1 that energies involved in transitions between vibrational states are much lower than corresponding electronic transitions, and can be considered to act independently (the Born-Oppenheimer approximation). Also, note that rotational energy transitions are not considered here as they are typically only important when considering free molecules (i.e. gaseous), and involve much lower energies than vibrational transitions.

A simple diatomic molecule in the presence of an electromagnetic wave of suitable frequency will experience a distortion of its electron cloud, changing it's polarizability α. Assuming the incident wave is monochromatic, the electric field can be written

$$\vec{\xi} = \vec{\xi_0}\cos(\omega_L t) \tag{3.1}$$

where ω_L is the frequency of the laser radiation. Thus an electric dipole moment of the bond

$$\vec{\mu}_{ind} = \alpha \cdot \vec{\xi} = \alpha \cdot \vec{\xi_0}\cos(\omega_L t) \tag{3.2}$$

will be induced upon interaction with the wave. This perturbation from the normal vibrational mode will result in a different vibration of the molecule which can be described in terms of the nuclear displacement co-ordinates

$$q^{(m)}(t) = q_0^{(m)}\cos(\omega_{vib}^{(m)} t) \tag{3.3}$$

where $\omega_{vib}^{(m)}$ is the frequency along the m^{th} vibrational co-ordinate. For a diatomic molecule there is only one axis of vibration, thus the m will be omitted for the rest of this discussion. In general however, for an N-particle molecule, there are $3N-6$ vibrational degrees of freedom ($3N-5$ for linear molecules, as in our case) which m will span. The polarizability can now

be written as a Taylor series expanded in terms of this displacement

$$\alpha(q) = \alpha(q_0) + q \cdot \left.\frac{\partial \alpha}{\partial q}\right|_{q=q_0} + \frac{q^2}{2} \cdot \left.\frac{\partial^2 \alpha}{\partial q^2}\right|_{q=q_0} + \dots \tag{3.4}$$

which can then be substituted into equation 3.2 after omitting quadratic or higher order terms and taking $\alpha(q_0) = \alpha_0$ to give

$$\begin{aligned}
\vec{\mu}_{ind} &= \alpha_0 \cdot \vec{\xi} + q \cdot \vec{\xi} \left.\frac{\partial \alpha}{\partial q}\right|_{q=q_0} \\
&= \alpha_0 \cdot \vec{\xi_0} \cos(\omega_L t) + q_0 \cdot \vec{\xi_0} \cos(\omega_{vib} t) \cos(\omega_L t) \left.\frac{\partial \alpha}{\partial q}\right|_{q=q_0} \\
&= \alpha_0 \cdot \vec{\xi_0} \cos(\omega_L t) + \frac{1}{2} q_0 \cdot \vec{\xi_0} \left[\cos([\omega_L + \omega_{vib}]t) + \cos([\omega_L - \omega_{vib}]t)\right] \left.\frac{\partial \alpha}{\partial q}\right|_{q=q_0}
\end{aligned} \tag{3.5}$$

where the identity $\cos(A)\cos(B) = \frac{1}{2}[\cos(A+B) + \cos(A-B)]$ has been used in the last step. An oscillating electric dipole will produce electromagnetic radiation, which in this case will have three frequency components. The first term corresponds to Rayleigh scattering, which will have the same frequency ω_L as the incident radiation. The other two are components of the Raman scattering corresponding to energy loss ($\omega_L - \omega_{vib}$) and gain ($\omega_L + \omega_{vib}$), usually termed Stokes and Anti-Stokes scattering respectively. As already mentioned, the Boltzmann distribution shows that the vibrational ground state is more likely to be occupied under normal conditions, thus Stokes-Raman scattering is usually more intense than Anti-Stokes Raman (from here, only Stokes-Raman scattering will be considered). A Stokes-Raman spectrum can be seen for carbon tetrachloride and Tylenol/paracetamol in figure 3.2, highlighting how different molecules can have different vibrational spectral features. Figure 3.2 also shows that a notch/edge filter is required around the laser excitation frequency, with a cutoff at 300 cm^{-1} away from the laser line for this particular system.

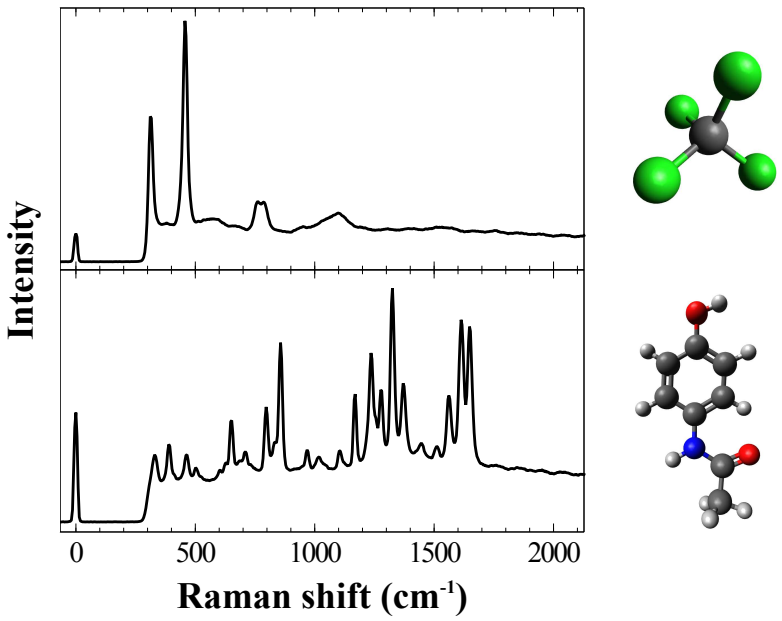

Figure 3.2: Example Stokes-Raman spectra of carbon tetrachloride (CCl_4, top) and N-acetyl-p-aminophenol (paracetamol, bottom), with corresponding molecular ball and stick models to the right. The green highlighted region shows the laser peak position, and the red region shows the spectral region where the band-stop/notch filter absorbs. The peaks in the region outside this correspond to Raman scattering from particular vibrational modes of the molecule. Note how paracetamol has more peaks than CCl_4 as it is a more complex molecule. This region below approximately 1700cm^{-1} is commonly referred to as the fingerprint region.

Equation 3.5 also reveals the selection rule for Raman scattering

$$\left.\frac{\partial \alpha}{\partial q}\right|_{q=q_0} \neq 0 \tag{3.6}$$

which indicates that it is a *change* in polarizability that results in Raman scattered radiation. This is the reason why water has a relatively low Raman cross section; while H_2O has a large α, it typically does not vary significantly under excitation (i.e. $\partial\alpha/\partial q \approx 0$).

While the shift was derived here in terms of angular frequency of the radiation, Raman shifts are typically expressed in terms of wavenumber in the vibrational spectroscopy community (in units of cm^{-1}). A photon of

energy E can be expressed in terms of absolute wavenumber $\tilde{\nu}$ by

$$E = hc\tilde{\nu} = h\nu \tag{3.7}$$

where $\nu = \omega/2\pi$ is the photon frequency, h is Planck's constant and c is the speed of light in vacuum. The Raman shift shows the frequency difference between the vibrational mode of a particular molecular bond and the incident laser, which can be written as

$$\Delta\tilde{\nu} = \pm\frac{\Delta E}{hc} \tag{3.8}$$

where ΔE is the energy difference, for example that between the states $S(0,0)$ and $S(0,1)$ in figure 3.1.

3.2.2 Polarized Raman Spectroscopy

The scattering intensity of particular Raman bands can be determined to be

$$I \propto \frac{\partial\alpha}{\partial q} \tag{3.9}$$

indicating larger changes in the polarizability during a particular vibration produce a greater intensity of Raman scattering. As the electric field $\vec{\xi}$ and induced dipole $\vec{\mu}$ in equation 3.2 are not necessarily aligned in space, the polarizability will more generally be a tensor

$$\begin{pmatrix} \mu_X \\ \mu_Y \\ \mu_Z \end{pmatrix} = \begin{pmatrix} \alpha_{XX} & \alpha_{XY} & \alpha_{XZ} \\ \alpha_{YX} & \alpha_{YY} & \alpha_{YZ} \\ \alpha_{ZX} & \alpha_{ZY} & \alpha_{ZZ} \end{pmatrix} \begin{pmatrix} \xi_X \\ \xi_Y \\ \xi_Z \end{pmatrix} \tag{3.10}$$

where X, Y and Z specify an arbitrary lab frame, suggesting that the intensity resulting from 3.9 will be polarization dependent in general. Alternatively expressing the differential of the polarizability tensor, known as

the Raman tensor, relates the incident electric field with the scattered field

$$\vec{\xi}_i^{(inc)} = \alpha'_{ij}\vec{\xi}_j^{(exc)} \tag{3.11}$$

where $\alpha'_{ij} = \frac{\partial \alpha_{ij}}{\partial q}$ (and $i, j = x, y, z$ are the co–ordinates of the molecular reference frame) for a particular vibrational mode. This tensor can be represented as an ellipsoid in an arbitrary co-ordinate frame. The general form of the tensor contains many terms, but can be reduced by appropriate alignment of the co-ordinate system with the natural axes of the ellipsoid such that only the three diagonal components are required. This tensor is called the principle axis of the Raman tensor (PART). Using Euler angles, the tensor can be converted between the (x, y, z) molecular frame and the (X, Y, Z) lab frame. The tensor in the latter co-ordinate frame will involve off–diagonal components in general, but all of which can be written in terms of the diagonal components of the molecular frame and functions of the Euler angles relating them.

The depolarization is the most important quantity measured in polarized Raman spectroscopy, which is the ratio of the Raman scattered intensity polarized perpendicularly to the incident radiation, $I_\perp$, to that of the parallel polarized radiation $I_\parallel$. The depolarization can then be written as

$$\rho = \frac{I_\perp}{I_\parallel} = \frac{3\gamma^2}{10\delta^2 + 4\gamma^2} \tag{3.12}$$

where the isotropic part of the lab–frame Raman tensor, δ, is

$$\delta = \frac{1}{3}(\alpha'_{XX} + \alpha'_{YY} + \alpha'_{ZZ}) \tag{3.13}$$

and the anisotropic part, γ, is

$$\begin{aligned}\gamma^2 =& \frac{1}{2}\left[(\alpha'_{XX}-\alpha'_{YY})^2+(\alpha'_{YY}-\alpha'_{ZZ})^2+(\alpha'_{ZZ}-\alpha'_{XX})^2\right] \\ &+\frac{3}{4}\left[(\alpha'_{XY}-\alpha'_{YX})^2+(\alpha'_{XZ}-\alpha'_{ZX})^2+(\alpha'_{YZ}-\alpha'_{ZY})^2\right] \end{aligned} \tag{3.14}$$

written in terms of the lab–frame Raman tensor components. As these components only rely on the three diagonal components in the molecular co–ordinate frame, three values of the depolarization are needed to measure all the components. In systems with increased symmetry, such as cylindrical and spherically symmetric systems, only two and one components are needed respectively.

In summary, the measurement of the depolarization from the ratio of particular Raman band intensities within some defined laboratory co–ordinate system can be used to extract information about the PART for a particular band, and thus from Euler angles, its orientation with respect to the lab axes. For a more in–depth account of polarized Raman microspectroscopy, see references [1, 2, 72, 73].

3.2.3 Raman Microspectroscopy

Raman spectroscopy typically uses a laser as an excitation source, as a high power is needed to be able to produce enough Raman scattering to be detected. Modern day spectrometers with sensitive CCDs allow for the detection of this scattering with relatively short acquisition times (milliseconds to minutes, dependent on the sample under investigation). A laser directed through a microscope can be focused by an objective to produce a small laser spot, which can be used as an illumination source for Raman scattering. This spot can be raster-scanned across the sample, with a spectrum being taken for each point, building up a three-dimensional data set of two-dimensional position and Raman spectral information. The lateral

resolution is set by the laser spot, which is in turn set by the properties of the microscope, namely the objective lens and the illuminating wavelength. The axial resolution can be modified by introducing confocality into the system using a pinhole before the spectrometer. The smaller the pinhole, the better the axial resolution, but this must be balanced by a tradeoff with the signal intensity.

The ultimate resolving power of a typical optical microscope is governed by the diffraction limit, which is in turn dependent on the wavelength of light. A common expression for this resolution Δx using a microscope was derived by Lord Rayleigh by considering the separation necessary to resolve two separate Airy disks to be

$$\Delta x = \frac{1.22 \cdot \lambda}{2 \cdot \text{N.A.}} \tag{3.15}$$

where

$$\text{NA} = n \sin \theta \tag{3.16}$$

is the numerical aperture, λ is the wavelength of the light, n is the refractive index of the material between the objective lens and the sample and the angle θ is measured between the maximum possible path to the objective, and the normal to the sample. As an example consider an objective with N.A. = 1.0 and a wavelength range of 400–1000nm (typical for Raman spectroscopy). When substituting these values into the above equation we get a resolution $r \approx$ 250–610nm. This is the limit in the lateral spatial resolution of Raman imaging in the far-field.

3.2.4 Near-Field Optics

In order to improve upon the diffraction-limited resolution, it is useful to consider the uncertainty principle[74]

$$\Delta p_x \Delta x \geq \frac{\hbar}{2} \tag{3.17}$$

where we can substitute the photon momentum relation $\Delta p_x = \hbar \Delta k_x \approx 2\pi\hbar/\lambda$ resulting in

$$\Delta x \geq \frac{\lambda}{4\pi} \tag{3.18}$$

upon re-arranging terms. One can see that the form is similar to Rayleigh's criterion (eq.3.15) in the proportionality to the wavelength. There is a critical assumption here in the step between converting the Δk_x term to a wavelength, in that we take the x-component to be the total contribution to the magnitude of the wavevector k, with the others set to zero ($k_y = k_x = 0$). In order to probe below the Rayleigh limit, we must consider the full expression for the wavevector

$$|k| = \sqrt{k_x^2 + k_y^2 + k_z^2} \tag{3.19}$$

where each component is a real value and less than or equal to k. However, it is possible to have a component larger than k, if another component is pure imaginary. For example let us restrict the system to the x-z plane. It is possible to have $|k_x| > |k|$ if k_z is imaginary such that

$$|k_x|^2 - |k|^2 = |k_z|^2. \tag{3.20}$$

The increase in $|k_x|$ corresponds physically to a smaller spread in the x-direction, i.e. a better spatial resolution. However upon substitution into

the expression for a plane wave

$$E_z = E_{z0}\, e^{ik_z z} = E_{z0}\, e^{-|k_z|z} \tag{3.21}$$

the imaginary k_z component causes the solution to become exponentially decaying in the z-direction. This is termed the optical near-field, which is used for many applications in optical sensing such as total internal reflection (TIR) microscopy (see figure 3.3). Note that the decaying solution occurs only for $z > 0$ and we reject the exponential growth for negative z as non-physical.

As an example of the range of the near-field, substituting $|k| = \frac{2\pi}{\lambda}$ and

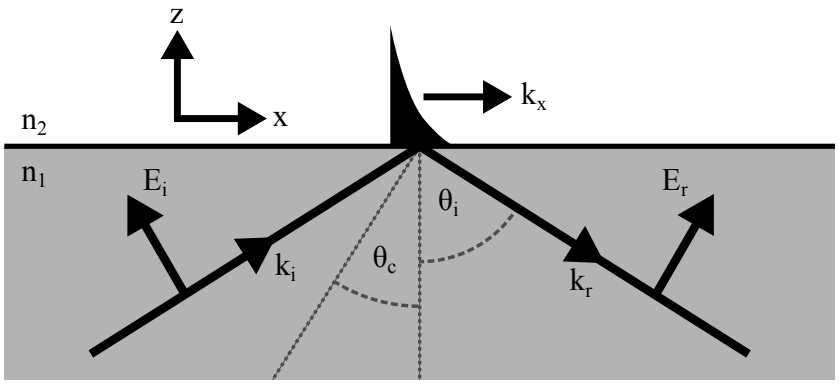

Figure 3.3: Diagram of an evanescent field at a planar interface. θ_c is the critical angle and θ_i is the angle of incidence. Evanescent waves occur for $\theta_i > \theta_c$.

$k_x \approx \Delta k_x \approx \frac{1}{2\Delta x}$ into equation 3.20 and taking the square root we obtain

$$|k_z| = \sqrt{\left(\frac{1}{2\Delta x}\right)^2 - \left(\frac{2\pi}{\lambda}\right)^2} \tag{3.22}$$

which can subsequently be substituted into equation 3.21 to give

$$E_z = E_{z0}\; exp\left\{ -z\sqrt{\left(\frac{1}{2\Delta x}\right)^2 - \left(\frac{2\pi}{\lambda}\right)^2} \right\}. \tag{3.23}$$

Using the fact that $I \propto E^2$ we can determine the typical range of the near-field. Combining the above equations and re-arranging for z results in

$$z_{1/2} = \ln\left(\sqrt{2}\right)\left[\left(\frac{1}{2\Delta x}\right)^2 - \left(\frac{2\pi}{\lambda}\right)^2\right]^{-\frac{1}{2}}. \tag{3.24}$$

Equation 3.24 indicates that in order to obtain a resolution in the z–direction of 10nm using a wavelength of 500nm, the near-field intensity would reduce by half after $\approx$ 7nm, highlighting the degree to which the near-field is confined. The lateral resolution, Δx, is dependant on the size of the probe, and should not be confused with the effect of the near–field confinement. The lateral resolution can be improved beyond the diffraction limit using physical probes as discussed in chapter 2, where SNOM techniques were developed in order to access near–fields using nanoscale apertures (see figure 2.4). However, these were shown to be insufficient for collecting the inherently weak intensities from Raman scattering. In order to collect Raman scattered radiation, the scattering process must be amplified or enhanced in some way.

3.3 Plasmonics

3.3.1 The Optical Properties of Metals

A typical model for metals consists of a rigid lattice of positively charged ion cores with a negatively charged gas composed of conduction band electrons. As metals are conductors, an electric field is forbidden within the bulk of the metal at macroscopic scales according to Maxwell's equations. This agrees with the fact that metals are highly reflective: the propagating electric field cannot pass through the bulk of the conductor. However, at a smaller scale, there will be some characteristic depth, δ, to which the electric field of light radiation will propagate, being rapidly attenuated. This

is known as the skin-depth, and is typically on the order of the wavelength of the light incident upon the surface. These common properties of metals are described by their material parameters, either the refractive index or dielectric permittivity, which are complex numbers in general, and are a function of the frequency of the incident light, ω. These parameters can be written in terms of one another, the choice between which one to use depending on the situation. Here, the dielectric function ϵ will be used to describe the materials of interest.

As ϵ is complex, it can be separated into real and imaginary parts

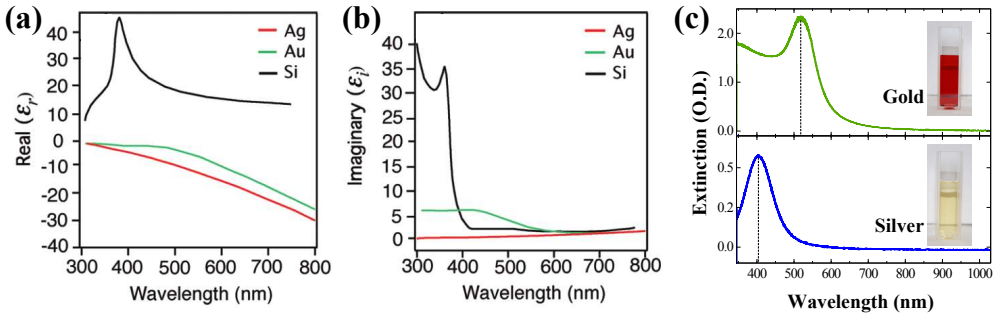

Figure 3.4: Real (a) and imaginary (b) components of the dielectric functions for silicon, silver and gold (modified from [62]). (c) Extinction spectra for small (<10nm) gold and silver colloids (inserts show photograph of the corresponding solutions).

$$\epsilon(\omega) = \epsilon_{re}(\omega) + i\epsilon_{im}(\omega) \tag{3.25}$$

where ϵ_{im} is related to the absorption of the medium.

The motion of the free electrons in the metal can be described using Drude-Lorentz theory[74,75], which uses the differential equation

$$m_e \frac{\partial^2 \vec{x}}{\partial t^2} + m_e \Gamma \frac{\partial \vec{x}}{\partial t} = e\vec{E}_0 e^{i\omega t} \tag{3.26}$$

where m_e is the mass of the electron, Γ is a damping term (related to the Fermi velocity and mean free path of the electrons) and E_0 is the amplitude of the applied field. The electric susceptibility of the medium can be written

$\chi = \frac{ne}{\epsilon_0}\frac{\vec{r}}{\vec{E}}$, which in turn can be related to the dielectric function by $\epsilon = 1+\chi$. Here ϵ_0 is the vacuum permittivity. The relation $\vec{P} = \epsilon_0\chi\vec{E}$ between the induced macroscopic polarization $\vec{P} = ne\vec{x}$ and electric field $\vec{E}$ has been assumed. Assuming the solution for the displacement $\vec{x}(t) = \vec{x}_0 e^{-i\omega t}$, the dielectric function according to the Drude-Lorentz model is found to be

$$\epsilon(\omega) = 1 - \frac{\omega_p^2}{\omega^2 + \Gamma^2} + i\frac{\Gamma\omega_p^2}{\omega(\omega^2 + \Gamma^2)} \tag{3.27}$$

where

$$\omega_p^2 = \frac{ne^2}{\epsilon_0 m_e} \tag{3.28}$$

is the plasma frequency, which describes the natural oscillation frequency of the free electron gas. The constant e corresponds to the electron charge, and n to the number density of electrons. As all other quantities in equation 3.28 are constant, n is the factor which causes variation between different metals. Figure 3.4 shows the real and imaginary parts of the dielectric constants for gold, silver and silicon. It should be noted that for materials such as gold and copper, intraband transitions must also be taken into account in the calculation of the dielectric function. However, this is not necessary when considering silver in the visible frequency range, and thus it will not be discussed in detail.

3.3.2 Surface Plasmons

The previous discussion concerned the free electron gas of an ideal bulk metal. If a planar interface with a dielectric medium is introduced, charge density standing waves will be set up at the boundary. An evanescent electric field will decay exponentially from the metal into the dielectric, as described in section 3.2. These are known as surface plasmons.

This spatial constraint in one dimension can be extended to all three di-

mensions, i.e. a spherical particle. For this case, if the particle is small enough, such that the skin depth $\delta >> a$, where a is the particle radius, then the electric field of visible light can be considered uniform throughout the particle. Even at scales of 10nm, macroscopic parameters such as the material polarizability can be used to good approximation. It can be shown that for a particle of material ϵ_1 embedded in a medium of material ϵ_2, the electric dipole polarizability is

$$\alpha = 4\pi\epsilon_0 a^3 \frac{\epsilon_1 - \epsilon_2}{\epsilon_1 + 2\epsilon_2} \tag{3.29}$$

where the ϵ_1 and ϵ_2 are the dimensionless bulk relative permittivities. Here the frequency dependence of α and ϵ_1 is assumed. Note that this expression becomes large when $\epsilon_1 = -2\epsilon_2$, which is known as the Frölich condition. For air, $\epsilon_2 \approx 1$, leading to a resonance when $\epsilon_1 = -2$. Figure 3.4 (a) and (b) show the real and imaginary parts of ϵ for gold, silver and silicon. For silver Re(ϵ) is close to -2 between 300-400nm and for gold between 500-600nm. This agrees well with the peak positions in the extinction (absorption + scattering) spectra shown in figure 3.4 (c).

This polarizability is used in calculations of the extinction cross section, which has contributions from scattering and absorption. The cross sections for these processes are given by

$$\sigma_{scattering} \propto k^4 \cdot |\alpha|^2 \tag{3.30}$$

and

$$\sigma_{absorption} \propto k \cdot \mathrm{Im}(\alpha) \tag{3.31}$$

where k is the wavenumber of the radiation. Equations 3.30 and 3.31 show that $\sigma_{scattering} \propto a^6$, while $\sigma_{absorption} \propto a^3$, thus absorbtion will dominate for smaller particles and scattering will dominate for larger particles. This

is readily observed with nanoparticles in aqueous solution, where for large particles, the color differs when viewed against a white background (i.e. observing the transmitted light) and a dark background (viewing the scattered light). The extinction spectra of such particles can thus be used as an indicator on the size of the particles (assuming the particles are spherical). The absorption efficiency (closely related to the cross sections above) can be shown to be

$$Q_{absorption} = \frac{12\pi\epsilon_0 a^3 \epsilon_2}{\mathrm{Im}(\epsilon_1)} \tag{3.32}$$

at the Frölich frequency. Note that for smaller $\mathrm{Im}(\epsilon_1)$ this efficiency increases, which, following from figure 3.4 (b) shows that silver will typically absorb radiation more efficiently across the visible range than gold. This can be linked qualitatively with the subsequent enhancement from plasmonic nanoparticles, and is a reason for the greater enhancement of Raman spectra by silver nanoparticles compared to gold.

The size- and shape-dependent properties of gold and silver nanoparticles are of major interest due to the large localized electric field they exhibit when excited by the appropriate wavelength of light. For small particles, the extinction spectra can be taken as having mostly absorption contributions. The absorption spectrum of metal colloidal particles typically exhibits a resonance peak at a particular wavelength, as seen in figure 3.4 (c). This can be taken as an absorption maximum, such that the radiation frequency matches the plasma oscillation frequency in the metal particle. This is known as a localized surface plasmon resonance (LSPR).

The equations 3.30 and 3.31 are valid for spherical particles, and originate from solving Maxwell's equations for scattering from a sphere small compared with the incident wavelength, first derived by Gustav Mie[60]. Solutions exist for spherical and spheroidal particles, but for more complex geometries no analytical solutions exist. Theoretical modelling of different

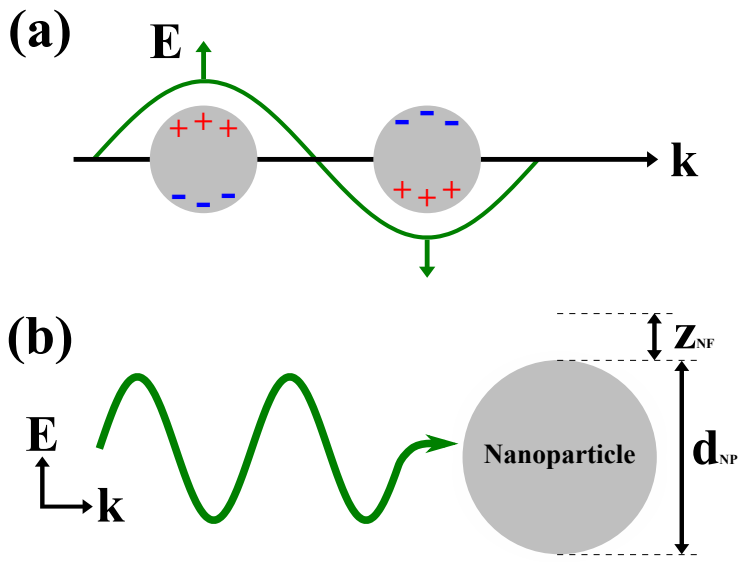

Figure 3.5: Localized surface plasmons. (a) shows the displacement of the free-electon sea in a nanoparticle due to an electromagnetic wave. (b) shows the dipolar LSPR with respect to the orientation of the electric field vector. The value z_{NF} is the decay length of the enhanced evanescent field, typically to the order of 10nm.

geometries can be performed using an array of different techniques such as finite element analysis where the structure is broken into small cells with simple geometries for which Maxwell's equations can be solved. However an intuitive explanation of the absorption in anisotropic nanoparticles is possible by considering characteristic length scales[76]. As an example, a cylinder (i.e. nanorod) has two characteristic length scales, the long axial length, and the shorter radial length. This is shown in the absorption as two separate peaks, corresponding to a dipolar LSPR for the long and short axis of the rod.

3.4 AFM

3.4.1 Basics of Atomic Force Microscopy

An alternative method for imaging below the diffraction limit is to use miniature probes and measure some physical response when brought very

close to a surface. This is the central idea underlying SPM, whereby a probe is raster scanned across a surface and some response is measured by feedback electronics, a signal from which can be built up into an image. Instead of measuring a particular type of response of a sample to light (such as transmission or phase constrast for example), SPM typically deals with topographic features and is thus restricted to surfaces.

The two most common SPM methods are scanning tunneling microscopy (STM), where the response mechanism relates to the electronic tunneling current from a metal tip, and atomic force microscopy (AFM) where mechanical forces are used for feedback. As STM requires a voltage bias to be applied across the tip-sample, only electrically conducting substrates can be used. AFM on the other hand can be used for almost any sample under many different environments, and is thus applicable to a wider range of samples.

AFM was first demonstrated by G. Binnig et. al., who imaged surfaces in air with resolution of 30 Å[77]. Since its discovery, commercial AFM instruments exist, which typically consist of a silicon or silicon nitride cantilever with a sharp tip at the end. This cantilever is positioned by piezoelectric transducers resulting in sub-nanometer positioning accuracy. When the tip is brought into contact with a sample, the cantilever will be deflected. The magnitude of this deflection can be detected by aligning a laser to the cantilever and recording the movement on a photodiode quadrant (see figure 3.6). If the tip is then raster-scanned across the sample, the deflection can be measured at each point, and with suitable calibration and feedback electronics for controlling the positioning, the topography can be mapped. Full contact with the surface may cause damage to the tip during raster-scanning, thus an alternative mode that is often used is intermittant-contact (or "tapping") mode AFM whereby the cantilever is oscillated such that the tip is not simply dragged across the surface and only experiences

brief contact. Images are then built up by inspecting the amplitude or frequency response of the cantilver at the surface with respect to a setpoint. The resolution of AFM has been demonstrated to subatomic levels in vacuum, but in ambient conditions is typically the order of several nanometers, and is inherently dependent on the sharpness of the tip. The accuracy with which these probes can be positioned makes them the most viable option for near-field optical measurements. As the images produced with AFM

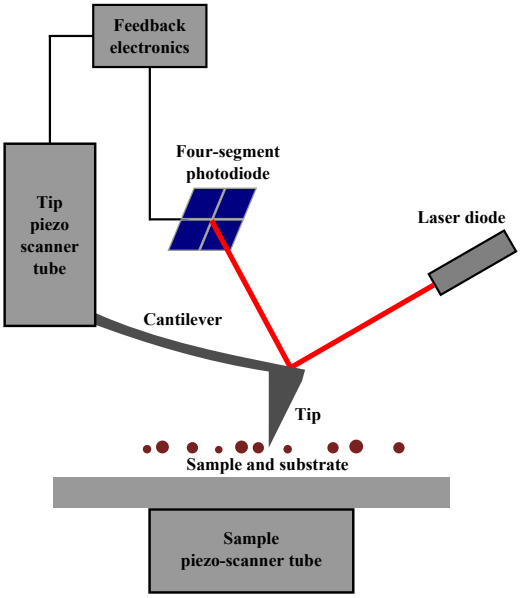

Figure 3.6: Basic components of AFM. A cantilver chip (typically silicon or silicon nitride) is mounted to a piezo scanner tube, which is controlled by detection electronics in a feedback loop. The feedback loop obtains input from a laser beam reflected from the back of the cantilever onto a photodiode quadrant. The feedback loop attempts to maintain a constant setpoint for the particular mode of operation being used, which can then be used to build an image. The sample stage can also be controlled by a piezo tube.

are a result of the convolution of the tip with the sample, care must be taken during the process of imaging and the subsequent interpretation of features. Image artifacts due to incorrect setting of feedback parameters are a common source of misinterpretation, as well as "multiple–tip–effects", which are due to bad tip geometries caused by a damaged tip apex or adhesion of unwanted material to the tip, which manifests as almost perfectly

repeating features in AFM images.

3.4.2 Nanoscale forces

AFM instruments are capable of more than just topographic imaging. As the physical probe used for scanning is controlled by a piezo-transducer capable of accurate positioning (sub–nm in ambient conditions), the effect of forces can be measured by changing the tip–sample displacement at a point and observing the laser deflection, and is termed force spectroscopy. A force spectroscopy measurement if typically composed of two main parts, the approach (or extend) when the tip is moved towards the sample from free space, and the retraction, where the tip is moved away from the set-point. The value for the setpoint essentially controls the maximum deflection (i.e. force) that the tip can undergo during the measurement, and when to stop the approach and begin retraction.

Force spectra are usually displayed as vertical deflection (or equally force is the cantilever response is appropriately calibrated) vs. piezo displacement, as shown in the example in Figure 3.7. The tip approaches from a starting

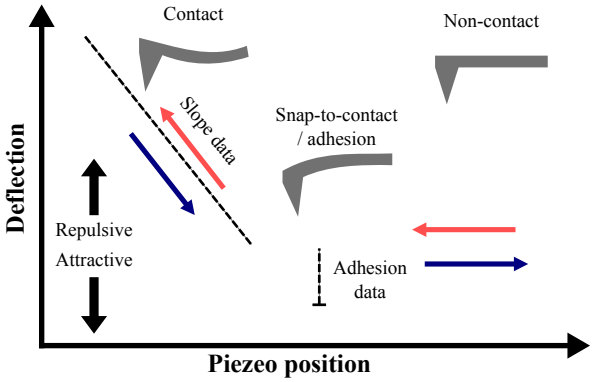

Figure 3.7: Example force spectrum, with regions of interest highlighted, and cartoon of AFM cantilever corresponding to particular points.

position such that the surface is within the piezo extension range, but far enough away from the surface that the initial section of the approach curve

is flat. Once the tip is close enough to the sample, the tip will "snap–to–contact", due to attractive forces from the surface. As the pieze continues to extend towards the surface, the repulsive forces deflect the cantilever in the opposite direction to this, usually with a linear profile observed. The point at the base of this line where the deflection is that of the non-contact regime is termed the contact point. The gradient of the contact deflection, termed the sensitivity s, can be measured when force spectra are acquired on a hard sample (relative to the tip material). This allows deflection to be measured in units of length, rather than photodiode voltage. Further calibration by measuring the cantilever resonance due to the thermal background when retracted from the surface allows the spring constant of the cantilever to be obtained, allowing deflection to be measured in units of Newtons. The slope of the contact region, when applied to other softer materials, can reveal information about the mechanical properties.
When the tip reaches the setpoint deflection, the extend part of the force curve terminates, and the piezo begins to retract from the surface. While the majority of the extend and retract curves overlap, interesting phenomena can be observed at or just above the contact point. In ambient conditions, there are usually adhesion effects observed, either due to a thin water layer at the surface, or other sample–dependent attractive interactions.

3.5 Summary

This chapter has introduced the concepts necessary for understanding the basic operation of TERS. AFM is used as a tool for positioning a nanoparticle, which greatly enhances the electric field in close proximity to its surface. This occurs when the excitation wavelength of the laser being used matches the LSPR of the particle. In Raman micro-spectroscopy, the frequency of the excitation laser must be matched to this LSPR max-

imum in order to maximize the field enhancement. The enhanced Raman scattered radiation can then be collected in the same way as for far-field Raman micro-spectroscopy. In order to distinguish between the enhanced radiation, spectra are usually acquired with the tip both in approached and retracted from the sample.

It should be noted that the polarization of the electric field in the focal region is non-trivial for high N.A. objectives. As mentioned in the literature review, this benefits the backscattering configuration, as there will be a significant axial polarization at the focus. However this is not spatially uniform, and the component in the center of an ideal focal spot is zero. The maximum contribution is slightly off-center, thus when the tip is aligned with the laser spot, it is common for placement to intentionally be slightly off-center.

4. Preparation and Testing of TERS Probes Fabricated *in-situ*

4.1 Introduction

In this chapter, the first steps towards a reproducible method for fabricating TERS tips will be presented. The first step will involve investigating a novel method used for preparing tips *in-situ* by means of light-mediated nanoparticle growth. Following this, the prepared tips are characterized by electron microscopy to determine the structures formed using this new technique. Preliminary TERS tests carried out on sub-100nm diameter diphenylalanine (FF) peptide nanotubes are subsequently described and analyzed. The equipment used for the TERS measurements and light-induced nanoparticle growth will be presented in the next section.

4.2 Instrumentation

4.2.1 Inverted Microscope and Spectrometer

The experimental setup for collecting the Raman spectra consists of a frequency doubled Nd:YAG laser (Laser2000) which is directed through the back port of an inverted microscope (IX71 Olympus) as shown in figure 4.1. The backscattered light is collected through the same objective, focused into an optical fiber connected to a spectrometer (Andor Shamrock) which records the dispersed light on a 1024×100 pixel CCD camera (Andor iDUS CCD).

The wavelength of the laser is 532nm with spectral linewidth of less

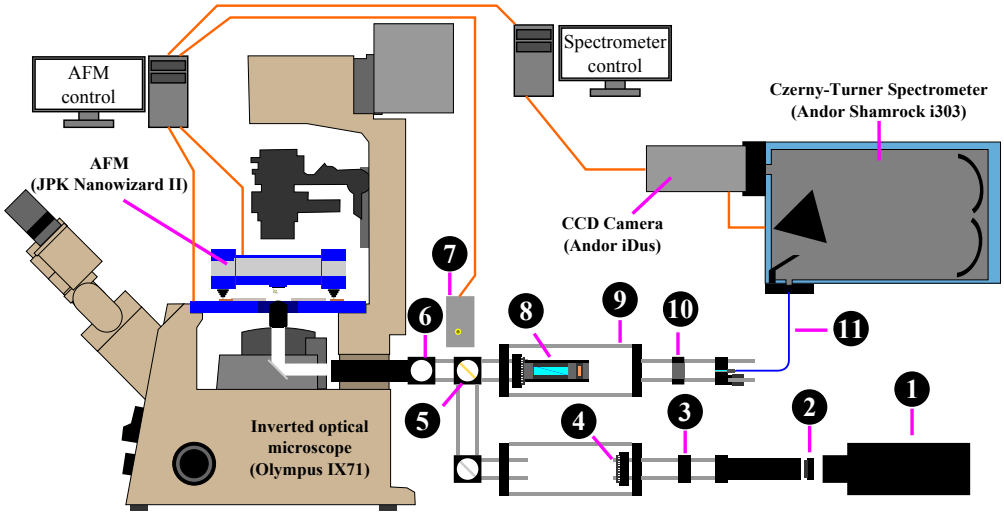

Figure 4.1: Schematic of the combined AFM-Raman microscope. **Legend: (1)** 532nm 20mW solid state laser, **(2)** removable linear polarizer and neutral density filters, **(3)** laser line filter, **(4)** removable half wave plate (rotatable), **(5)** dichroic mirror (532 nm reflection), **(6)** removable beamsplitter, **(7)** photodiode setup for collection of backscattered light, **(8)** removable Glan-Thomson element with quarter wave plate (rotatable), **(9)** cage-system for improved alignment of system, **(10)** lens for focusing backscattered light into fiber, **(11)** fiber optic link to spectrometer.

than 0.1×10^{-3}nm and divergence less than 1.5mrad producing a maximum power of 20mW (safety class 3B). A plasma line filter (Semrock) is used after the laser exit aperture to remove any unwanted emission lines. The beam is then directed into the back-port of the microscope via a dichroic mirror which has a high reflection coefficient at 532nm. Subsequently the beam is focused by either an Olympus Uplan FL 20× objective (N.A. 0.5) or a UPlan SApo 60× water immersion objective (N.A. 1.2) onto the sample of interest. Backscattered light is collected by the same objective and directed back to the dichroic mirror where any light at a wavelength other than 532nm, such as Raman scattered light, is transmitted. Following this, a notch/bandstop filter is used to remove any remaining 532nm radiation. The initial setup used was previously built using lenses to direct the scattered light through a slit into the spectrometer with a pinhole also used to

improve the axial resolution. This was later replaced with a lens focusing the light into a fiber-optic coupling to the spectrometer. As the diameter of the fiber is comparable to the pinhole diameter (100μm), this can effectively be used to perform the same function.

The mechanical arrangement of the optics utilizes a Thorlabs cage systems. Here the optics can easily be kept rigidly aligned, and additional elements, such as neutral density filters and polarization optics, can be added easily (see figure 4.2).

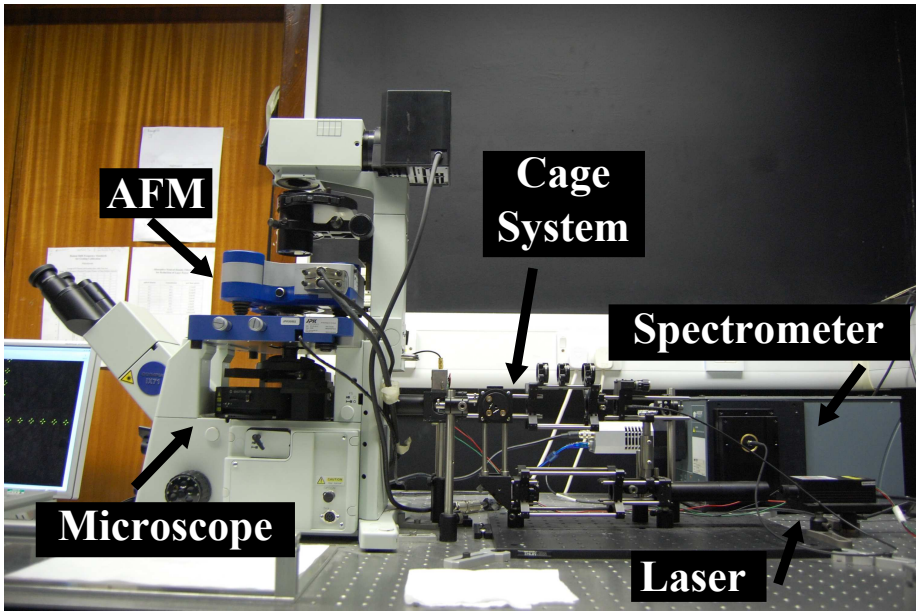

Figure 4.2: Photograph of equipment corresponding to the schematic in Figure 4.1

4.2.2 Combined AFM-Raman

The AFM used is the Nanowizard II (JPK) which is placed on a motorized stage (Tip-assisted optics (TAO) stage, JPK) fitted to the microscope. Both the tip-holder and stage have three degrees of translational freedom, which is necessary for TERS, as the laser must be aligned with the focused laser spot, then fixed and the stage subsequently used for movement. AFM cantilevers are fixed to a glass block attached to the underside of the AFM

head. A laser beam is directed through the block onto the cantilever, and the specular reflection collected by a four-quadrant photodiode. When the cantilever is deflected, the laser path will change, which changed the photodiode signal, which can then be converted into a topographic measurement. The laser used in the AFM head is in the infra-red and thus will not interfere with the Raman measurements.

The output channels from the AFM are connected to a controller, which outputs the data to a computer using the manufacturer's software. This allows the automated approaching to the sample, and a connection to the camera port of the microscope for simultaneous optical micrograph and AFM acquisition. The AFM software also allows for the incorporation of home-made software. Raman imaging software was developed previously using Microsoft Visual Basic, allowing the synchronization of the AFM stage positioning and spectrometer control (B. Lekprasert, PhD thesis [1]).

4.2.3 Photodiode Setup for Backscattering Images

A key factor in TERS measurements is the alignment of the tip within the laser focus. In order to do this, the tip is raster scanned through the laser spot. The reflected image is used to find the position of the tip, which corresponds to the highest backscattered light spot. The tip is then fixed in the appropriate position, and all subsequent positioning is achieved by moving the sample stage, whilst the tip and laser are kept in the same position. To detect this reflected image, a 50:50 beam-splitter is placed just before the back port of the microscope, which redirects the backscattered light into a lens focused onto a photodiode. The signal from the photodiode is connected to the AFM controller, which allows an image of the backscattered light to be built up.

Images acquired from raster scanned AFM tips will typically show a diffraction limited spot, corresponding to reflection from the apex. However,

depending on the cantilever geometry, these can be difficult to interpret, especially as a flat cantilever will reflect a larger fraction of the light when compared with the reflection from the tip apex. This can be overcome by inspecting the images from the cantilever data sheet to obtain information regarding its geometry and attain correct focusing of the laser.

4.3 Photoinduced Nanoparticle Aggregates

4.3.1 Laser-grown SERS Substrates

In chapter 2 a variety of methods for preparing silver nanoparticles with controllable size and shape were introduced. Methods for preparing seeds were shown which involved using light as an energy source to induce the transformation of the particles to the desired geometry and crystallinity. Other light-based synthesis techniques exist, an early example by Jin et. al. demonstrated the photoinduced conversion of small silver nanoparticles into single-crystal prisms[78], with subsequent control over the edge length of the prisms using dual-wavelength illumination.[79] A similar experiment by Maillard et. al. also produced nanodisks, but which used small spherical seeds prepared by a common procedure using sodium citrate and sodium borohydride.[80] Here, a mechanism for the formation of the particles was presented, as well as a calculation for the quantum yield of the reaction. These methods differ from those mentioned in chapter 2 in that they do not require additional silver ions in the solution as silver ions are generated from the seeds by oxidative etching. The details of this reaction will be discussed in section 4.3.2.

A different method using similar materials which is used for rapidly producing SERS substrates on demand in aqueous solution was demonstrated by Bjerneld et. al. in 2002.[81,82] Here it was shown that a laser focused

at the interface between a substrate and a prepared solution will form a stable SERS-active nanoparticle aggregate. The size of the cluster is shown to be dependent on the laser spot size, power and exposure time. It was also shown that coating the substrate with a monolayer of 3-amino-trimethoxysilane (APTMS) significantly increases the initial growth rate. Here, it is proposed that the same technique could be adopted for fabricating TERS-active tips *in-situ*. A schematic for a suggested procedure is shown in figure 4.3. This method would allow the tip to be prepared

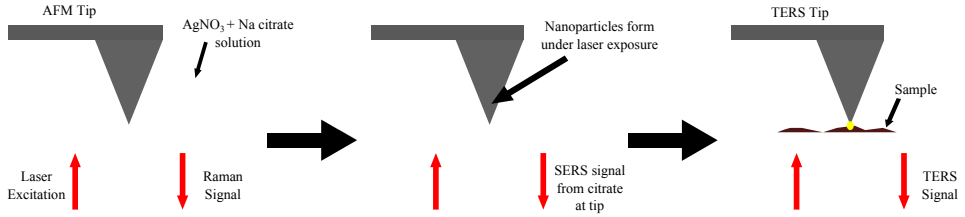

Figure 4.3: Schematic for the proposed method of using a photoinduced reaction to grow nanoparticles at an AFM tip apex for TERS.

completely *in-situ*, avoiding the need for the careful transfer of a tip prepared using other common methods, which may lead to contamination. This is especially important with silver probes as they oxidize quickly in air, which decreases the enhancement such that the tips are no longer useful. In addition to this, the SERS signal from chemicals in the solution in close proximity to the nanoparticles on the tip will increase as the growth progresses. This could be detected using time-course spectra, which could be used as a feedback mechanism for the growth process.

4.3.2 Mechanism for Nanoparticle Formation

The silver nanodisks produced by Maillard et. al. used similar materials to Bjerneld et. al., with the exception of the use of sodium borohydride as a reducing agent in the former method. With the incorporation of this reagent,

the method by Maillard et. al. contains small 8nm sized seeds before irradiation. However according to Bjerneld et. al., the mixture of silver nitrate and citrate in de-ionized water does not result in any detectable nanoparticle formation at room temperature. Only when the solution is irradiated do nanoparticles form. The exact mechanism for the initial stages of this seed-less nanoparticle formation is not currently clear. However, once under way, it is assumed that the reaction will be similar to that described in [80, 83], which will now be discussed briefly.

The citrate molecule (specifically trisodium citrate) has three carboxyl

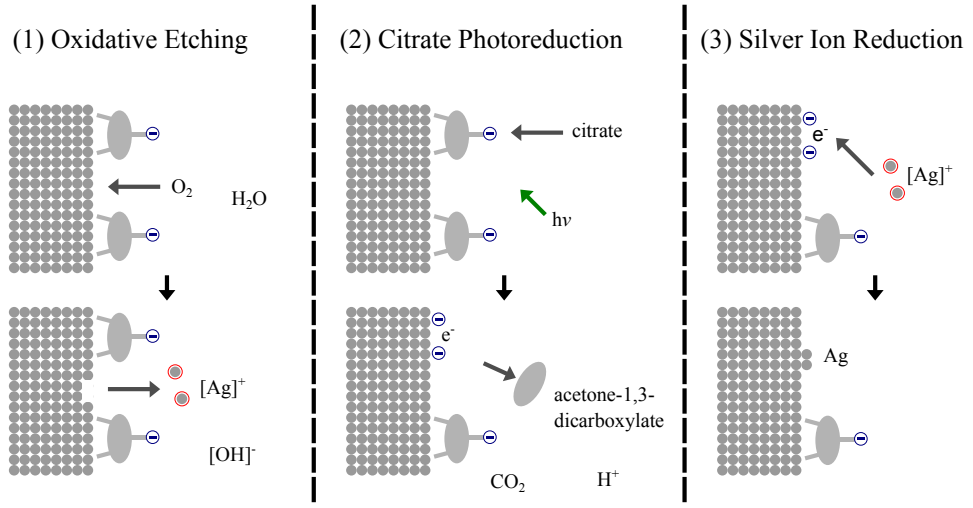

Figure 4.4: Competing mechanisms taking place at the nanoparticle surface in the photoinduced synthesis process as suggested by Maillard et. al.[80].

groups which are negatively charged. It has been shown by Munro et. al. that it is likely that two of these carboxyl groups will adsorb to a silver surface, leaving one free pointing away from the surface.[84] This free carboxyl will cause electrostatic repulsion between particles, stabilizing them in solution.

If the solution of nanoparticles is irradiated with light of frequency sufficiently close to the LSPR absorption band of the nanoparticles, as discussed in chapter 3, a large electric field close to the surface will be present. Under

these conditions, it is thought that three chemical processes will occur:

1. Oxidative etching of silver from nanoparticle surface
2. Photoinduced oxidation of citrate adsorbed to silver
3. Silver ion reduction and deposition onto the nanoparticle surface.

These processes are shown graphically in figure 4.4. The corresponding chemical kinetic equations are

$$2\mathrm{Ag} + \frac{1}{2}\mathrm{O_2} + \mathrm{H_2O} \rightarrow 2\mathrm{Ag^+} + 2[\mathrm{OH}]^- \tag{4.1}$$

for process (1),

$$\text{citrate} \rightarrow \text{acetone-1,3-dicarboxylate} + \mathrm{CO_2} + \mathrm{H^+} + 2\mathrm{e^-} \tag{4.2}$$

for process (2), and

$$2\mathrm{e^-} + 2\mathrm{Ag^+} \rightarrow 2\mathrm{Ag} \tag{4.3}$$

for process (3)[83]. Process (1) will occur more often for particles which scatter/absorb the radiation less, typically the smaller particles for visible light. Process (2) will occur more for particles which absorb/scatter light more. From this it can be inferred that a particle will keep growing until it is too large, and the incident light will not scatter/absorb efficiently. This can be seen in time-resolved UV-vis absorption spectra in [83]. This implies that smaller particles with a plasmon resonance far from the laser frequency will be more likely to contribute silver ions to the solution via process (1). The nucleophilic citrate molecules will preferentially adsorb to the silver particles. However, when the nanoparticle LSPR is excited, the large electric field will cause the citrate to dissociate, injecting electrons into the nanoparticle, creating a photovoltage (as shown in figure 4.4, (2)). This photovoltage is then responsible for the deposition of positive silver

ions onto the nanoparticle. Overall, the citrate reduces the silver ions in solution by indirectly causing a negative photovoltage at the nanoparticle surface, which itself essentially acts as a catalyst for the citrate oxidation. For the process used by Bjerneld et. al., this presents a problem, as initially there are no seed particles. Thus some property of the focused laser must be allowing the particles to initially nucleate and grow without being broken apart by process (1). Another difference between Maillard et. al. and Bjerneld et. al.'s method is the time required for the process to be completed, the former taking several hours to complete, while the latter is takes less than ten minutes. This is most likely to be due to the large difference in power density, as Bjerneld et. al. use a laser spot focused by a microscope. Additional complexities occur in this process such as the presence of an interface, and the nontrivial polarization of a laser spot focused with a high N.A. objective. All these factors could conceivably have an effect on the nucleation and growth of nanoparticles.

However, due to the simplicity of the process compared to other TERS tip preparations, this method will serve as an initial test for the proof-of-principle study for producing TERS probes *in-situ*. In this chapter, the preparation of probes, and their characterization by electron microscopy will be presented, followed by some initial results from a test application to a sample of interest.

4.4 Preparation of TERS Probes Using Photo-induced Technique

4.4.1 Procedure for Tip Preparation

The precursor solution was prepared using the same concentrations as given in [81, 82]. This involved dissolving silver nitrate salts in de-ionized water to 0.5mM. The same concentration of sodium citrate tribasic was also

prepared in de-ionized water separately. Both solutions were left in an ultrasonic bath until all crystals were fully dissolved. Following this, the silver nitrate and sodium citrate solutions were combined in a 1:1 ratio to give the solution used for photoinduced growth. The resulting solution was completely transparent, which indicates that either no silver nanoparticles are present, or the solution is too dilute to observe the yellow colour of the transmitted light from typical nanoparticle solutions.

The solution was first tested on glass coverslips, in a repeat of the work carried out by Bjerneld et. al., where the 532nm laser used for Raman measurements was utilized. A volume of between 200-1000μL was pipetted onto the glass coverslip, and the laser beam focused by either a 20$\times$ or water-immersion 60$\times$ objective. The process was highly reproducible, with nanoparticle aggregates forming every time the laser was exposed to the solution-glass interface. Figure 4.5 shows an example of an aggregate as viewed by the microscope camera, and an AFM measurement (note: AFM and optical micrograph correspond to different particle aggregates). The AFM measurements were taken after cleaning the residual solution off the coverslip with de-ionized water. This appeared to have no effect on the aggregate, indicating a good adhesion to the glass surface. The aggregate varies in height throughout the spot diameter of the spot, but is typically no larger than 100nm in height. However, in this case the height cannot be trusted as a measure of particle diameter, as it is not possible to tell whether multiple particles are stacked on top of one another. Following these tests, the same process was attempted to grow the nanoparticles on AFM tips. The location of the tip apex was determined using the backscattered reflection of the laser, as described in section 4.2 The tip was positioned roughly 200μm above the glass surface in order to avoid additional growth at this interface. Once aligned, the growth solution was added, and microscope focus suitably adjusted to find the AFM tip (as the light path will differ in

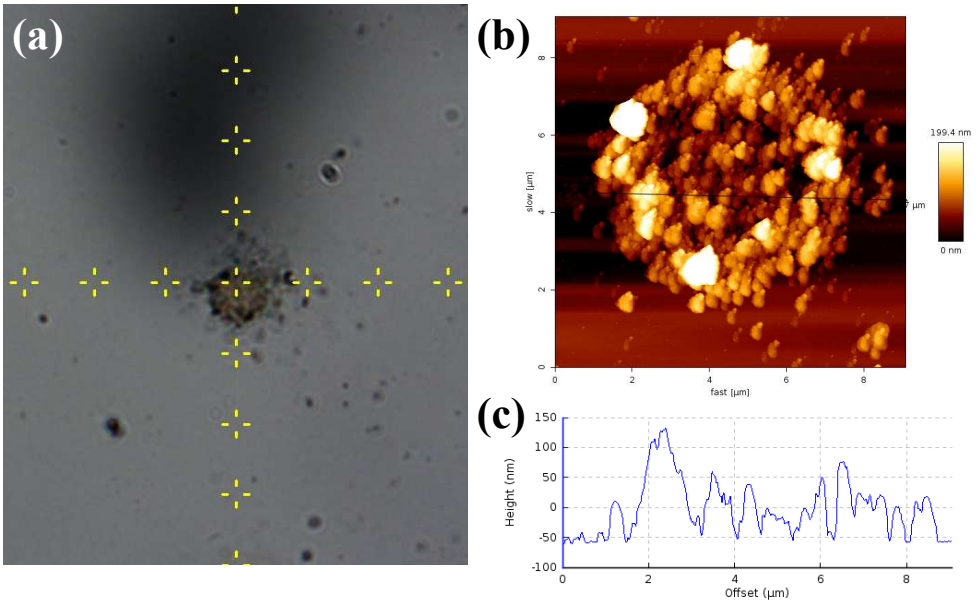

Figure 4.5: Laser-induced nanoparticle aggregates replicated from [81,82]. The optical micrograph (a) shows a typical spot grown at 5mW laser power at a glass slide interface with the nanoparticle growth solution. The AFM image (b) and corresponding line profile (c) indicate a spot size of between (6-8μm). (Note: the shape of the particles in the AFM image appears to be suffering from a tip-effect.)

air and water). Once this was achieved, the laser was exposed to the tip in the same manner as for the growth on the glass coverslip.

In both the glass coverslip and AFM tip synthesis, the microscope image

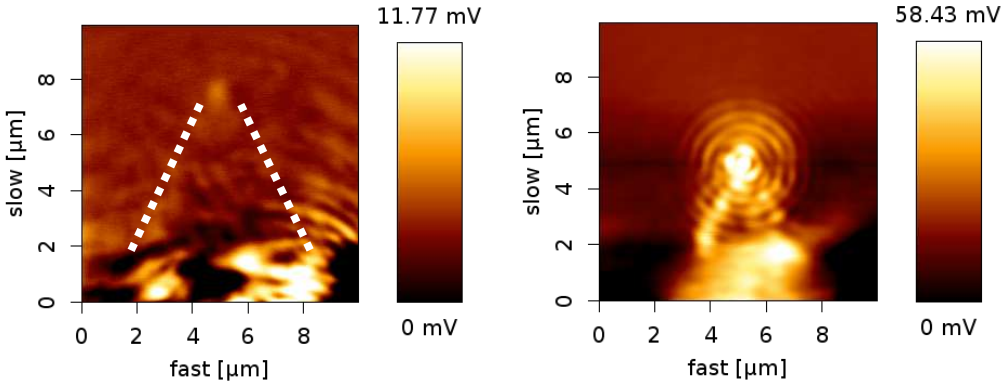

Figure 4.6: Backscattering images collected before (left) and after (right) growth on the same AFM tip at 5mW for a tip completely submerged in precursor solution, raised 200μm from a supporting glass substrate. The dotted white lines in the image on the right are a guide for the eye.

of the focused laser shows a visible difference in light scattering throughout the growth process. Initially the laser spot intensity fluctuates, possibly due to convection currents in the fluid. Once the silver aggregate is formed, the backscattered light intensity dramatically increases. This can be seen for the case of an AFM tip in figure 4.6, where the maximum voltage from the photodiode after the growth is over five times that of the backscattering image before growth. It can also be seen that the tip appears to be much rougher after the growth procedure. However, as these backscattering images are diffraction limited, they cannot be used for much more than a qualitative test of the presence of the silver nanoparticles.

The method by Bjerneld et. al. also used a modified surface to promote the attachment of the silver nanoparticles. This consisted of a monolayer of 3-aminopropyltrimethoxysilane (APTMS), which bonds to the silicon in the glass, leaving an amine (NH_2) group pointing outwards from the surface. This will give the surface an overall positive charge, which is thought to attract the slight negative charge on the silver nanoparticles from the unbonded carboxyl on the adsorbed citrate molecules. Here, a similar molecule was used for attachment, 3-aminopropyltriethoxysilane (APTES), which behaves similarly to APTMS. For the preparation of a monolayer, APTES was combined with methanol in a 1:10 ratio, and the glass slide or AFM tip was immersed for 12 hours.[85] After this, they are removed and rinsed with methanol and dried under a nitrogen flow. When the laser-induced growth process was performed on modified substrates, the growth rate was found to increase, which is in agreement with Bjerneld et. al. [81, 82]. This can be seen in figure 4.7, where the integrated intensity is shown for different laser power and in the presence or absence of an APTES coating. It can be seen that the Raman scattering enhancement increases until reaching a plateau, except for the case of the unmodified tip irradiated with 5mW, where the subsequent points were excluded for

clarity. It can be seen that the uncoated tip requires a much longer time to obtain the same enhancement as the cases where APTES is present. With the APTES coating, the enhancement increases at a much greater rate, and also depends on the laser power. After the SERS signal intensity

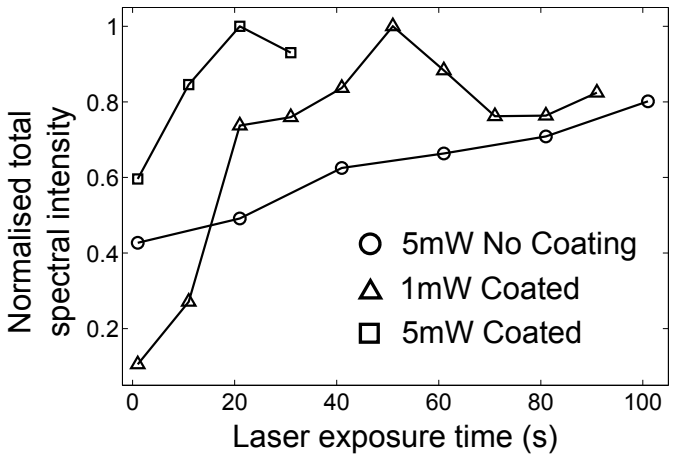

Figure 4.7: Individually normalized growth curves showing the total Raman spectral intensity increasing with time for the nanoparticle growth on AFM tip apex. The value in mW is the laser power before entrance to the microscope, and"Coated" refers to the presence of an APTES surface modification. It can be seen that both increased power and APTES coating cause an increased total signal, indicating an accelerated increase of nanoparticle growth at the tip.

appears to stop increasing, the growth process is stopped by blocking the laser. The probe is then cleaned with de-ionized water and left in air to dry before being used.

4.4.2 Characterization of Probes

Imaging the backscattered laser light before and after the growth process has shown that some differences can be seen, mainly in the magnitude of the reflected light. However, in order to characterize the nanoparticles in greater detail, higher resolution techniques must be used. Ideally, the optical properties of these aggregates should also be measured, but this is difficult due to their size. Thus in this section, the characterization is performed by electron microscopy techniques.

For the initial tests on used AFM tips, scanning electron microscopy (SEM) indicated the presence of nanoparticle aggregates, though not at the tip apex. This was thought to be due to two factors: the high N.A., high magnification (60x) objective used, and the interpretation of the backscattering images. The latter problem was addressed by comparing the manufacturer's tip specifications with the observed backscattering images in order to correctly place the tip apex in the laser spot. The former was solved by switching to an objective with a lower N.A. and spot size (20x Olympus) so that a larger area of the tip is coated in silver nanoparticles. Following this, a second set of used tips was investigated using SEM and energy-dispersive x-ray (EDX) spectroscopy. EDX analyzes the X-rays dispersed from the material under electron-beam illumination, and matches the energy to characteristic atomic transitions for particular elements. This process can be applied to an entire image, or raster scanned to produce an elemental mapping, showing the spatial distribution of different materials. The results from a tip prepared by the photoinduced growth method are shown in fig. 4.8. It can be seen that there is a good correlation between the regions with lighter contrast close to the tip apex in the SEM micrograph, and the silver distribution in the EDX mapping. The SEM and EDX

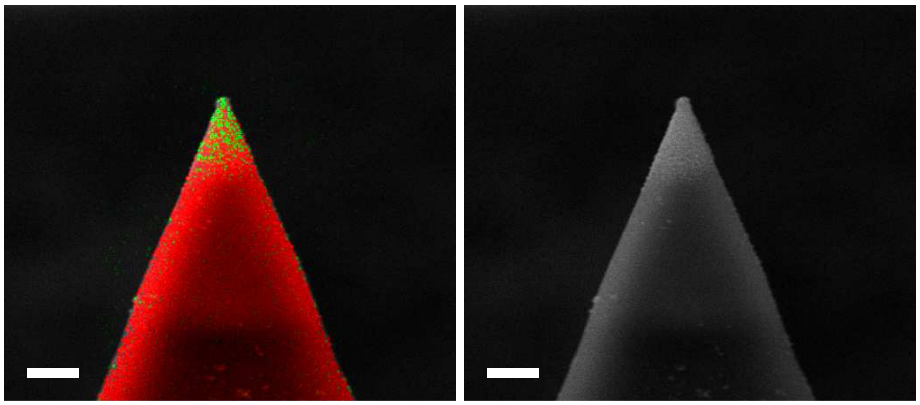

Figure 4.8: EDX (left) and SEM (right) images for an AFM tip coated in Ag nanoparticles. The red and green overlay in the EDX image correspond to silicon and silver peak mappings respectively (Scale bar 2μm).

images indicate that the silver nanoparticles attach to the AFM tip, but lack the resolution to analyze individual particles. Transmission electron microscopy (TEM) offers this high resolution, but is usually restricted to planar samples with thickness of less than 100nm. However, many semiconductor samples can be analyzed by taking "slices" from bulk materials using focused ion beam (FIB) milling in order to investigate interfaces which would not be possible in a TEM otherwise. This can be performed in an SEM, and the samples can be transferred using a microscale needle probe. The same process can be applied to an AFM tip, where the cantilever is fixed or "glued" by depositing a metal (tungsten was used here). The cantilever is then cut using the FIB, and transferred, using the needle probe, onto a TEM grid in the SEM sample chamber. This can then be transferred to the TEM and analyzed using a suitably oriented mount.
Using TEM, and a closely related technique, scanning-TEM (STEM), along with EDX, the particles at the tip apex could be observed with the desired resolution. For initial tests where the unmodified silicon tips were irradiated in solution with 5mW of laser power, the general surface density was low, with no particles at the tip apex as seen in figure 4.9. Here the EDX silver mapping can be compared with the STEM image, to confirm whether the structures shown at the tip contain silver.
While the principle of coating a tip in silver nanoparticles appears to be successful, the surface coverage using plain, uncoated silicon tips is not sufficient. TEM images acquired at the tip apex show a clear change with the APTES layer, with a greater coverage and larger proportion of high aspect ratio nanoparticles present, as seen in Fig 4.10.

The presence of these new, rod-like particles is unexpected, as the previous tips showed randomly-sized roughly spherical nanoparticles. One suggestion for the origin of these particles is that the presence of the coating initially causes the first few seeds generated in the reaction to be fixed

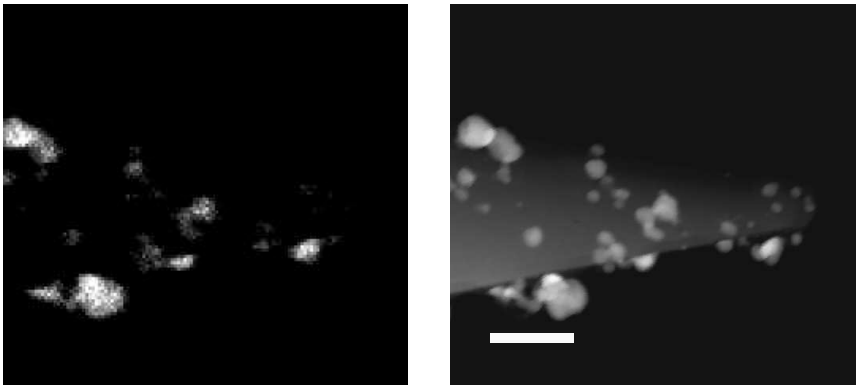

Figure 4.9: EDX mapping for silver (left) and STEM (right) for an unmodified silicon AFM tip (Scale bar 200nm).

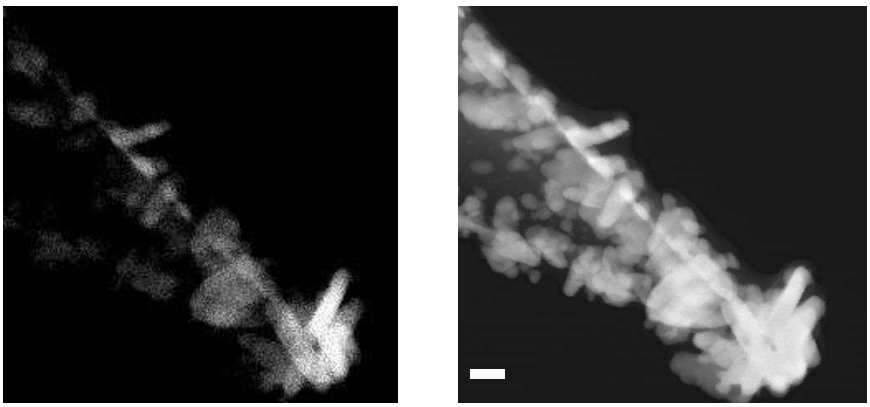

Figure 4.10: EDX mapping for silver (left) and STEM (right) for an APTES-coated silicon AFM tip at 5mW incident laser power (Scale bar 200nm).

in space, so that the particle is constrained with respect to the polarization of the laser, which may then lead to preferential growth in a particular direction.

While the results shown in figure 4.10 satisfy the requirement of having nanoparticles at the tip apex, the density and geometry is not optimal, as there appear to be several elongated nanoparticles pointing in different directions, and are too large to give the desired resolution of 10-30nm. Additionally, the junctions between nanoparticles separated by only a few nanoparticles will experience an even larger electric field than an isolated

one. The enhancement of the Raman signal from any molecule within such a region will be orders of magnitude larger than that from a single particle, which is the requirement for a TERS probe. Similar results were seen by Umakoshi et. al., who attempted the preparation of TERS probes in a similar manner.[86]

There, probes were shown with very large tip-radii, but which had nanoscale roughness. The authors claimed that the enhancement from one of these sites would still allow nanoscale imaging resolution in principle, though no experimental evidence of this was given. The laser power was

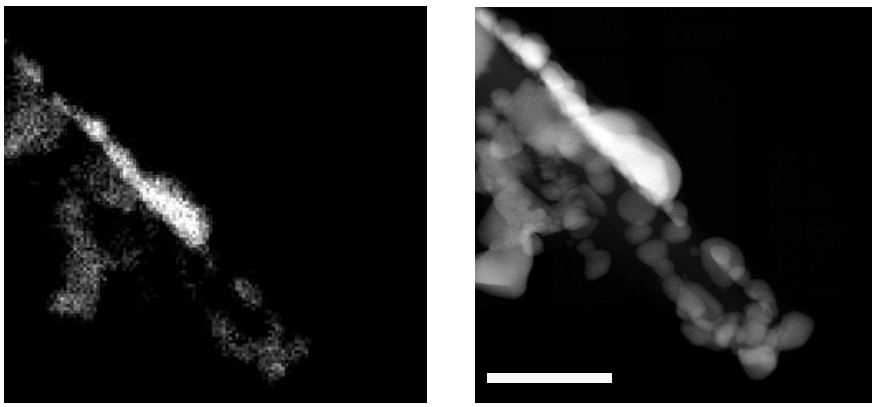

Figure 4.11: EDX (left) and STEM (right) for an APTES-coated silicon AFM tip at 1mW incident laser power (Scale bar 200nm).

shown to be a factor controlling the rate of the reaction, and may be used as a parameter for controlling the growth process on APTES-coated AFM tips. The same procedure used for preparing the tip shown in figure 4.10 was repeated, with a laser power of 1mW used instead of 5mW. The result from one tip grown at this lower power is shown in figure 4.11. It can be seen that there are no elongated particles present as before, and the particles present appear to be similar to those in Fig 4.9, though with a greater coverage, with particles at the tip apex. Both the coverage of the nanoparticles and the size and geometry at the tip apex fulfill the requirements for a TERS probe. The images shown in figures 4.9, 4.10, and 4.11 are one

example, of tips produced under each condition. The TEM/STEM/EDX measurements were repeated twice for each tip, with similar results for tips grown under the same conditions.

The nanoparticle size distributions were counted for each tip in or-

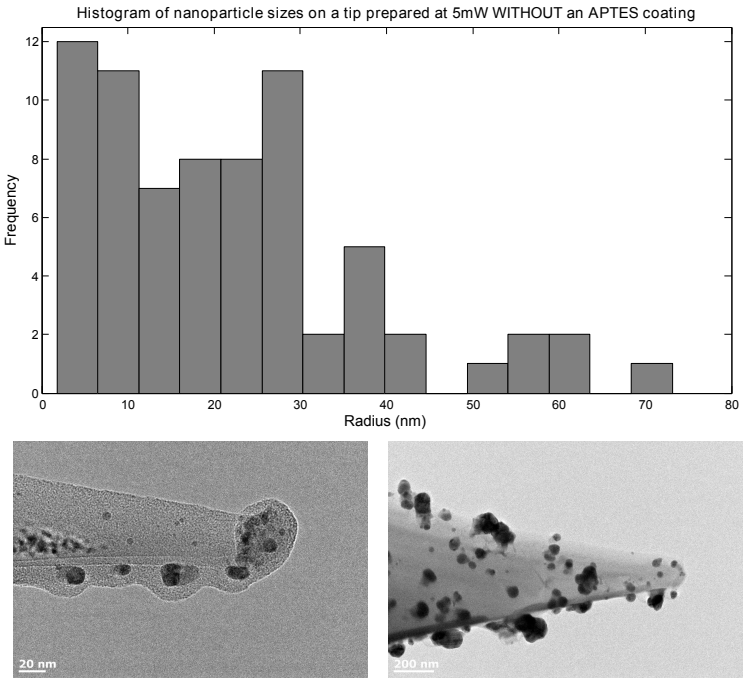

Figure 4.12: Particle size analysis for tips prepared with no APTES coating at 5mW of laser power

der to investigate the correlation with the reaction conditions (APTES coating and laser power). The electron microraphs were analyzed using ImageJ (NIH, http://imagej.nih.gov/ij/) by manually selecting the area corresponding to a particle. Automated detection of nanoparticles was not possible due to the three-dimensional nature of the images, and the close proximity of the particles. When manually selecting the nanoparticle areas, an elliptical area was measured, and recorded. This was performed for one representative image for each tip, and the data for the area was collated for each tip prepared under the same conditions. A rough value for the size of the particle was taken by converting the area data into a radius by

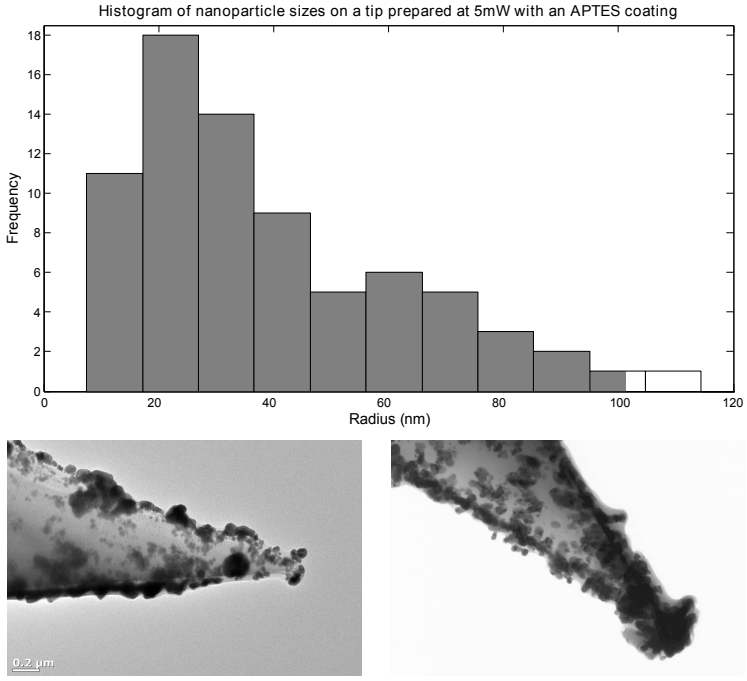

Figure 4.13: Particle size analysis for tips prepared with an APTES coating at 5mW of laser power

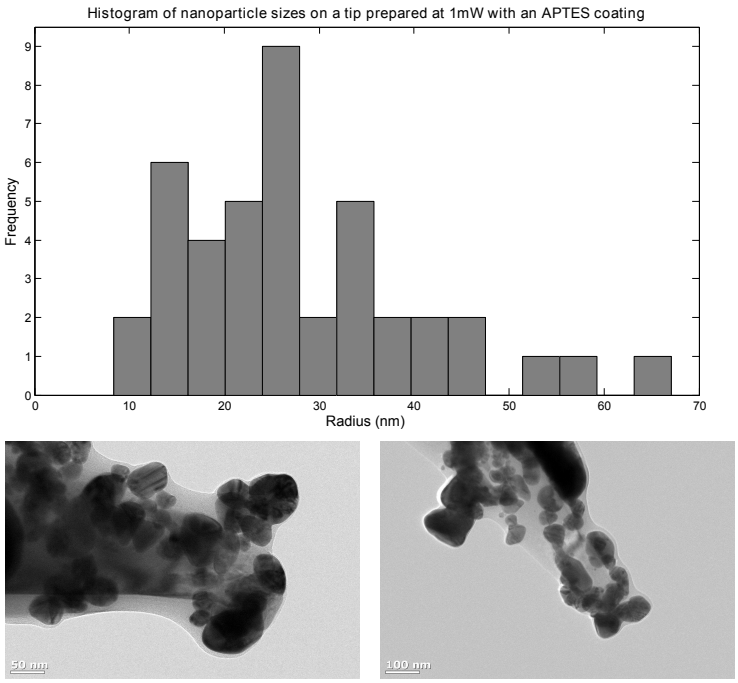

Figure 4.14: Particle size analysis for tips prepared with with an APTES coating at 1mW of laser power

assuming each particle is spherical. Histograms of the data were then plotted for each of the three different growth conditions. These histograms are shown with the corresponding images used in figures 4.12, 4.13, and 4.14. Only clearly defined particles were measured, and any ambiguous or out of focus clusters were not included. As a result, many smaller particles which are likely to be present were not detectable, and thus aren't measured for the tips where the coverage is too dense to observe these particles clearly. These smaller particles were observed for the tips that were not coated, as seen in figure 4.12. Here, the largest particle in the histogram is roughly 70nm, though it can be seen there are larger features in the corresponding TEM images. These were excluded, as it is not clear if these are single particles, or aggregated particles. However, even with the inclusion of these structures, the maximum size can be estimated at no larger than 200nm.

For the procedure using APTES coated tips at 5mW, the particles observed are much larger. The histogram in figure 4.13 indicates a number of structures larger than 50nm. It should be noted that a majority of the particles measured from the bottom right TEM image in figure 4.13 were taken from the region further up the tip, as the coverage close to the apex is too dense to take any conclusive size measurements from. For this tip however, the radius of the aggregate at the apex is at least 150nm.

For the tips prepared with an APTES coating, and at a lower laser power of 1mW (figure 4.14), the particles are observed to be much smaller on average than for the 5mW laser exposure. The coverage is also still high, and for both tips shown in figure 4.14 there are nanoparticles of the desired size at the apex.

4.5 TERS Experiments on FF Nanotubes

4.5.1 Experimental Method

4.5.2 Results

In the previous section, it was shown that probes which are, in principle, suitable for TERS could be produced *in-situ*. In order to confirm these tips are in fact suitable for TERS experiments, measurements on a simple, well-known sample is required. The sample chosen for this was a self-assembled peptide structure, composed of diphenylalanine (FF) molecules. These rigid structures have been studied by polarized Raman spectroscopy previously, for tubes with diameters between 400–1800nm.[1,87,88] It is known that these FF nanotubes can have diameters much smaller than 400nm, but these are not possible to measure individually using diffraction-limited Raman microspectroscopy, as the signal is too weak. However, TERS may be able to measure even smaller FF nanotubes, whilst also measuring the topography from the AFM. In the context of testing the TERS probes prepared *in-situ*, the FF tubes can be used to estimate both the enhancement and spatial resolution, as the tubes are one dimensional, and can be compared with the corresponding AFM images. Initial TERS experiments were carried out using the probes shown in figures 4.9 and 4.10 which did not provide sufficient enhancement to allow measurement of TERS for FF tubes. A simple sample of p-aminothiophenol (pATP) was initially used before the FF nanotube sample. Samples were prepared by evaporating silver onto a glass coverslip, which was then immersed in a 0.1mM pATP-methanol solution for two hours, as described in [89]. This was intended to observe the effect of gap-mode TERS, which increases the enhancement of TERS[90]. However, it was observed that a strong signal was present even in the absence of a TERS tip, and the sample also lacked the nanoscale

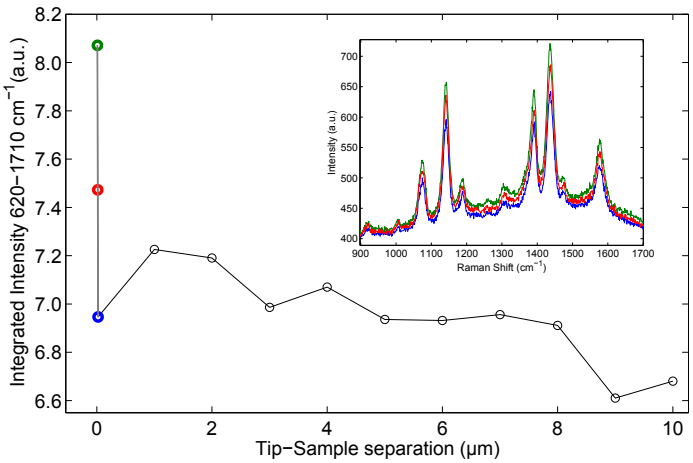

Figure 4.15: Plot of the integrated spectral intensity for pATP on silver versus the distance of the TERS tip. The inset shows the spectra when the tip is between 10-30nm, which were approximately set by changing the oscillation amplitude of an approached tip in closed feedback.

structural variations required for investigating the spatial resolution of the instrument. Furthermore, the spectra observed from the tips prepared using 5mW laser power and an APTES coating (figure 4.10) displayed broad peaks with no distinct Raman bands, which is typically associated with pyrolytic carbon compounds.[35] This may have been caused by the large density of nanoparticles producing a much larger combined electric near-field, which may be strong enough to be destructive to the sample material in close proximity.

For the tips without an APTES coating, measurements of the Raman spectrum of pATP were taken for different tip-sample distances, as shown in figure 4.15. A sharp increase in the intensity of the integrated spectrum was observed when the tip gets very close to the sample. The inset spectra also show a slight increase. However, as the pATP is already on a layer of silver, which itself is rough, a strong SERS effect is thought to be responsible for the majority of the signal. Typically, TERS measurements consist of a spectrum acquired when the tip is in near–contact with the sample, and then another with the tip retracted (the far-field, diffraction-limited

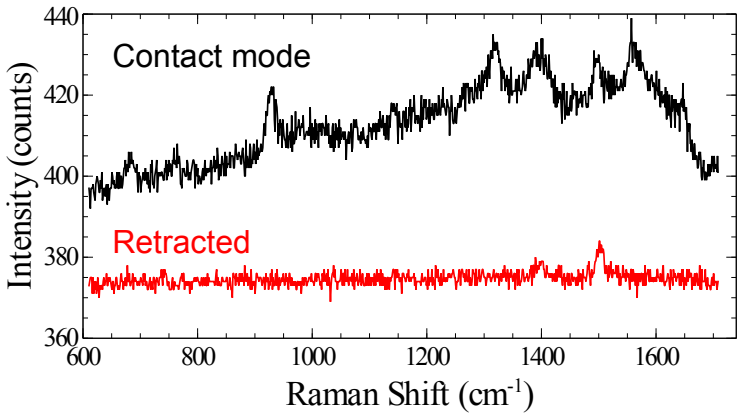

Figure 4.16: TERS spectra of a suspected contaminant for the tip approached in contact mode (black) and retracted from the surface (red) of an FFNT sample (10s, 200 μW). It can be seen that the approached spectrum contains a broad range of peaks at the higher end of the fingerprint region, which is indicative of amorphous/pyrolitic carbon contaminants.

Raman spectrum). This allows measurement of the enhancement factor by comparing the intensity of the approached vs. retracted spectral bands. [5] For these measurements, the enhamcement of the pATP by the tips prepared without APTES gave an enhancement of approximately 100×. For the tips prepared with APTES at 5mW, the enhancement factor was unable to be obtained due to a lack of clarity in the spectra produced. For the tips produced at 1mW using APTES-coated tips (figure 4.11), the FF nanotubes were used. The FF nanotube samples were prepared by B. Lekprasert, using the method described in [87], and deposited on a quartz coverslip. With a prepared tip, the sample was investigated using the optical microscope, and regions with smaller nanotubes identified. Initial experiments of point-spectra showed only a suggestion of carbon contaminants when the tip was approached, as shown in figure 4.16.

Intermittent-mode AFM imaging was then used to identify the precise locations of smaller FF nanotubes, with an example shown in figure 4.18(a). The lateral resolution of this image is poor due to background noise from the laser power supply. However, the diameter can be estimated from

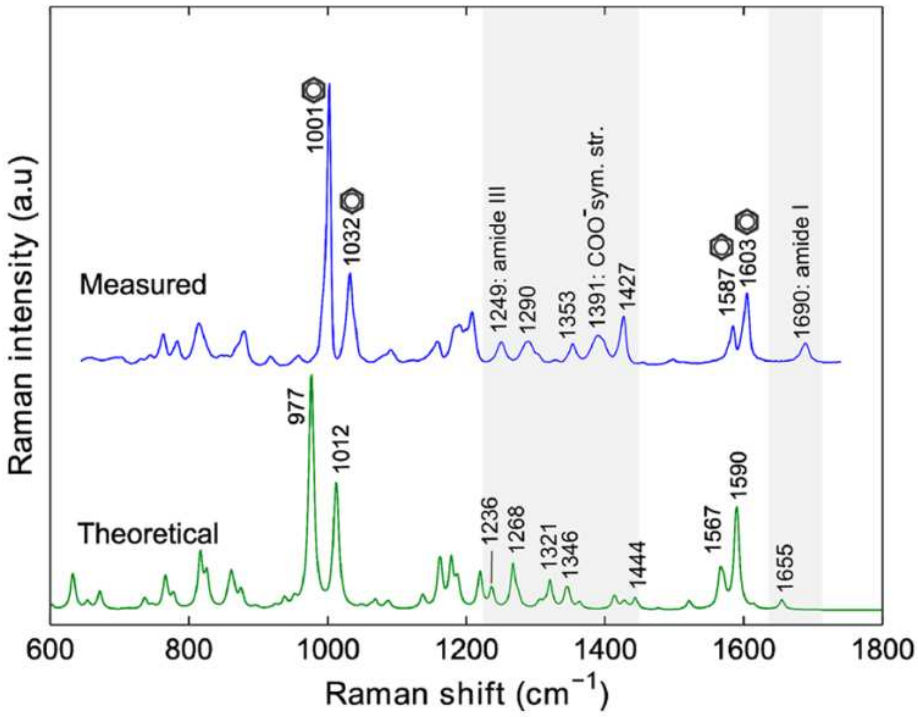

Figure 4.17: Experimental and theoretical Raman spectrum of FF nanotubes with band assignments (adapted from [88])

.

the height of the image, when taking a cross-section of the tube (Figure 4.18(c)).

As mentioned, the enhancement factor is typically calculated by comparing Raman spectra acquired when the tip is approached and retracted. However, in the case of the FF nanotubes below 400nm diameter, the far-field spectrum shows no signal. For this case, the enhancement factor can be calculated by using a far-field measurement from a larger FF tube. From this, the signal and estimated scattering volumes can be calculated as shown in section 2.2.1.

To obtain an estimate of the spatial resolution for the TERS measurements, Raman spectra were recorded at subsequent points in a line across the diameter of a FF nanotube. Provided the step size between the location of the spectra is sufficiently small, any change in the spectra can be

compared with the associated AFM image. Using this, the resolution can be estimated by considering the convolution between the tip and the FF nanotube diameter. After observing small FF nanotubes with AFM, Ra-

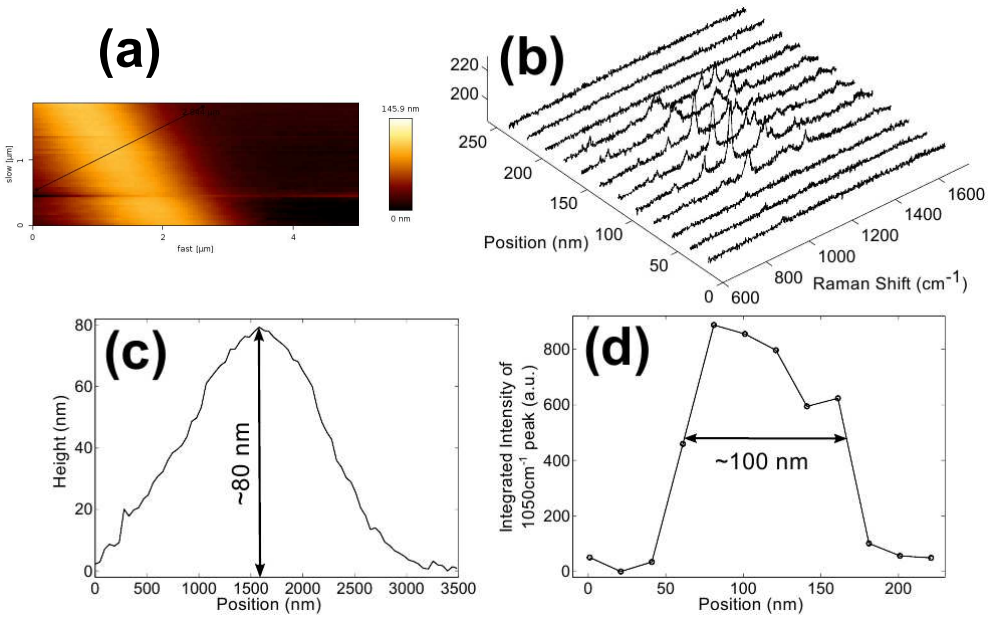

Figure 4.18: TERS resolution test on an FFNT. AFM image (a) with line profile shown in (c) suggesting a nanotube diameter of 80nm. Selection of spectra taken at 10 μW across this line at 20nm steps with tip approached in contact mode with sample shown in (b), with the peak-area of the 1050cm^{-1} band plotted in (d), suggesting a structure of size 100nm

man line-scans were acquired across the diameter of the tube, with a step of 20nm between each spectrum. This relatively high step size was chosen because the typical time for acquiring a spectrum was one minute, thus a higher step size decreases the total acquisition time for the line scan. Also, for the point-to-point measurements of the Raman spectrum, the tip was approached in contact mode with the sample. While the spectra generally produced different spectra when the tip was approached to the sample, the repeatability of the signals obtained was low. On one occasion, the spectrum across a tube produced a similar signal at neighboring points across a distance which was similar to that of the tube diameter, as shown in

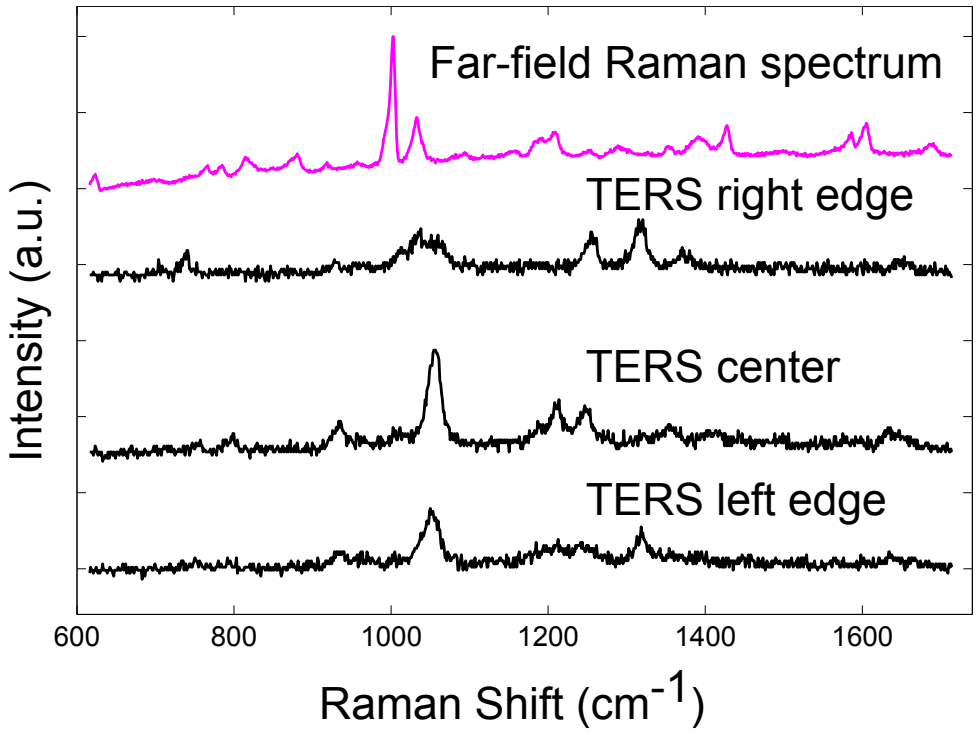

Figure 4.19: Selected TERS spectra from figure 4.18 at different positions along the line scan, together with a far-field FF tube Raman spectrum for comparison.

the sequence of Raman spectra in figures 4.18 (b) and reffig:TERScloseup. When this was repeated with the points acquired in the reverse direction, the same result was not observed. However, the spectra shown for this line scan show similarities with the far-field FF nanotube spectra (figure 4.17). Several bands in these spectra can be matched to the aromatic groups, such as those at 1056 cm^{-1} (in-plane CH bending) and 1216 cm^{-1} (CH bending with ring stretching), which are found at 1031 and 1198 cm^{-1} in the Raman spectra of FF nanotubes. Also, the TERS spectra also show bands at 934, 1247, and 1319 cm^{-1}, which can be assigned to the C-COO- stretching, Amide III and CH2 deformations respectively.[91]

It should be noted that the strong 1003cm^{-1} Raman band (symmetric breathing of phenyl) is missing, which is in agreement with some previous TERS spectra of phenylalanine amino acids[91]. However this is also in con-

flict with the results presented by Blum et. al. who observed this peak in their TERS measurements[92]. It is suggested here that this difference may result from the different conformations of the phenylalanine. In the experiment presented here, the phenylalanine molecules are self-assembled into nanotubes, while in [91] they form a monolayer on a gold surface, and in [92] the molecules are deposited on gold and measured with STM-TERS, not AFM-TERS. While these factors may affect the results in each case, the results here lack the reproducibility to conclusively offer an answer for the observed absence of the 1003cm^{-1} band.

It can be seen that the spectra closer to the middle of the tube differ

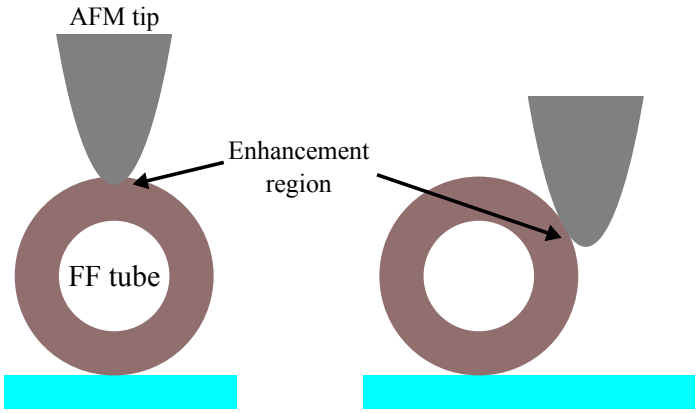

Figure 4.20: Schematic of how the enhancement region across a FF tube will differ due to the orientation of the tip.

from those at the edge. This may be due to the changing orientation of the FF molecules within the tube with respect to the enhancement region. Plotting the diameter of the strongest repeated band at 1050cm^{-1} from figure 4.18(b), the diameter of the tube from the Raman line profile can be estimated as 100nm (figure 4.18(d)). When compared to the AFM height measurement of the FF tube which gave a diameter of 80nm, it is suggested that the tip apex radius is of the order 20-30nm when the convolution between tip and sample is considered.

While the results of the TERS experiments were difficult to reproduce, the

presence of regular enhancement from the tips produced *in-situ* demonstrates the proof-of-principle for this method of preparing TERS tips.

4.6 Summary and Discussion of Results

An *in-situ* method for preparing TERS-active tips has been demonstrated with the aim of improving the tip preparation procedure. TERS experiments tried with these tips has thus far provided preliminary results indicating a degree of enhancement, but low reproducibility of results. All tips observed in the electron microscope studies had been coated with silver nanoparticles and a detectable difference in Raman spectra was observed repeatedly when the tips were brought into contact with a sample. However, these spectra often appeared to suggest contamination, with some containing broad peaks corresponding to amorphous carbon compounds. One contaminant that is frequently seen is the sodium citrate reducing agent from the growth process giving peaks seen in figure 4.7. The majority of contaminants are thought to originate from the growth process when the tip is immersed in the solution. The best TERS results were obtained with the tips prepared using the APTES coating at a power of 1mW, which were able to be used to obtain a sub-diffraction-limited Raman line profile of a FF nanotube.

There are several directions this work could take to improve upon the proof-of-principle demonstration. The optimization of the nanoparticle size and geometry is important, as is the repeatability of the method used for producing them. As discussed in section 2.3, there are a wide range of solution-based techniques for preparing silver nanoparticles with a high degree of control over these properties. The utilization of these methods, in particular those involving photoinduced mechanisms, could potentially be used to extend the tip preparation further. When compared with typical thermally

induced nanoparticle synthesis techniques, photochemical methods offer a larger scope for control, as the wavelength, polarization and power can be adjusted, which may lead to new paths of nanoparticle synthesis. Several methods mentioned in section 2.3 have demonstrated such control, with a wide range of photochemical based techniques used to prepare nanoparticle shapes such as spheres, decahedra, triangular prisms, rods amongst others. The investigation of the suitability of these techniques will be presented in chapter 5.

In addition to the preparation of the desired nanoparticle shape and size, the correct attachment of the nanoparticle to the AFM probe is also vital. In this chapter APTES was introduced to the surface of the tip to promote attachment. While this was shown to increase the coverage, the exact time of attachment is unclear; it is not known whether the nanoparticles grow in solution and then adhere to the tip, or if the initial seeds produced upon irradiation attach to the tip and then grow. Understanding this process is necessary, as the nucleation stage of the reaction is likely to be critical for the resultant nanoparticle morphology at the tip apex.

For anisotropic nanoparticles, the orientation of attachment is crucial, as the plasmon resonance in such particles is sensitive to changes of orientation. For example, the longitudinal mode of the plasmon resonance from a silver nanorod would ideally be excited while the rod is orientated along the axis of the tip. If the nanorod is oriented perpendicular to this, the longitudinal mode may not be excited, and if it is, it would not be enhancing the sample directly underneath, but only at the ends of the rod.

Control over the direction may be possible by considering the polarization of the incident light used for growth. This is rather nontrivial for a focused laser beam at an interface, thus simpler optical setups should be considered first. The simplest possible experiment may involve fixed nanoparticle seeds on a surface, which are regrown in an appropriate solution using linearly

polarized light. This could be used to investigate the growth of anisotropic particles, and investigate the link with the plasmon-mediated chemical reactions, which may depend on the polarization of the light with respect to the nanoparticles. Additionally, investigation of the resultant particles from the growth of fixed nanoparticle seeds and freely moving seeds may elucidate information regarding whether the nanoparticles prepared using Bjerneld et. al.'s method are initially fixed on the APTES layer and then grow, or attach to the tip after growth.

Another issue pertinent to the testing of TERS probes is the sample used for the test experiments. The justification for the use of FF nanotubes involves both the measurement of the enhancement factor and the spatial resolution. Carbon nanotubes (CNTs) have been used in TERS studies to assess these characteristics. However, CNTs have a relatively large Raman cross section and can be readily detected with far-field Raman microspectroscopy, and gold tips with a lower enhancement factor can be used for these TERS experiments. While these studies are useful for structures where large enhancement is not necessarily required, other structures, most commonly in biologically-relevant materials, require enhancement from silver tips.

As mentioned, the one-dimensional structure of the FF tubes is useful for investigating the resolution of the tips. However, another advantage of using the FF nanotubes is the knowledge of the conformation of the FF molecules within the tubes with respect to the tube axis for larger tubes. [87,88] It has been shown that there is no detectable conformation change between nanotubes, microtubes and larger tube structures measured by X-ray diffraction studies. This may allow for a more in-depth understanding of TERS tips if repeated results can be correlated with the known structure of the tubes. This may not be possible with more complex samples such as cell membranes and viruses, where the nanoscale chemical structure is more variable and TERS results may be difficult to interpret. Studies of

these more complex systems should only be undertaken when probes have been adequately characterized, and shown to produce repeatable, consistent enhancing properties.

The characterization of the probes thus far has relied on electron mi-

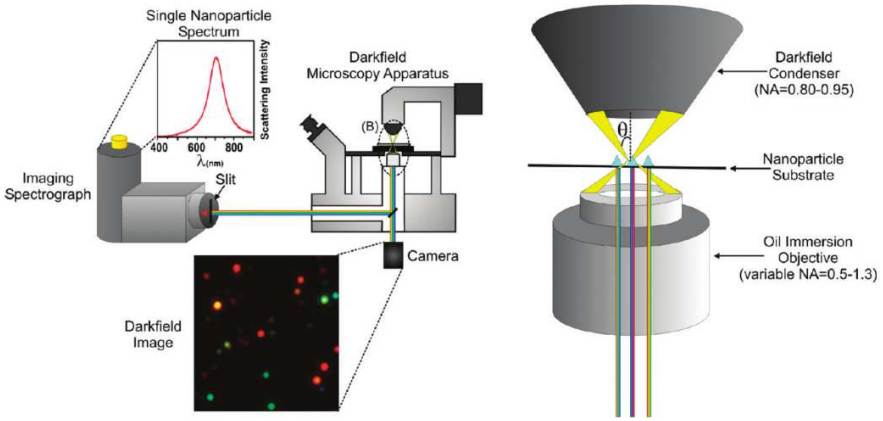

Figure 4.21: Schematic of a dark-field microscope adapted to include a spectrometer for the measurement of Rayleigh scattered light (adapted from [93]).

croscopy techniques. This is not feasible for analyzing all tips used for a TERS experiment due to the cost and necessary sample preparation time required. Other *in-situ* techniques for characterization may be possible. The laser backscattering images shown in figure 4.6 lack sufficient detail to infer any properties of the nanoparticles present at the tip. However, in [93], Henry et. al. demonstrate the use of a dark-field illumination setup to investigate the optical properties of individual plasmonic nanoparticles. The Rayleigh scattered light can be collected, and a spectrum obtained. This may be used to obtain information about the particles at the tip apex in TERS, and possibly infer their structure without the requirement of electron microscopy. It should be noted that dark-field Rayleigh scattering spectra should not be confused with the extinction spectra of nanoparticles, which include absorption as well as scattering.

An additional benefit to the probes prepared here is that the plasmonic particles are localized at the end of a silicon probe. This differs to several other

methods using solid wires, meaning the entire probe is the same material, i.e. has the same dielectric properties. It could be possible that the dielectric isolation from evaporation methods and the laser–induced method here allow for more ideal plasmonic properties of the nanoparticles. This could be further investigated by theoretical simulations and measurements using the mentioned dark–field scattering setup.

In chapter 5, the issue of controlling the nanoparticle size and shape using methods which could be adapted for use *in-situ* will be investigated.

5. Pathways to Controllable Nanoparticle Synthesis for TERS

5.1 Silver Nanorod Synthesis

The previous chapter introduced a relatively simple method for preparing silver nanoparticles *in-situ*, at the apex of an AFM tip. The particles produced by this method were not uniform in shape or size, and in some cases they formed large aggregates. While these particles produced an enhancement of the Raman scattering, the silver structures formed at the very apex of the tip varied in structure with no control over the final geometry. It is important to investigate pathways to control the geometry of the nanoparticle, as their shape and size are vital for the enhancement characteristics of the tip.

In section 2.3, a range of methods were introduced for preparing colloidal nanoparticle solutions with a high degree of control. In particular, procedures for preparing pentagonally-twinned nanorods were introduced. These will be investigated in this chapter, and assessed for their suitability for use in preparing TERS tips.

A key aspect of control is the preparation of an appropriate initial seed solution, which was not considered for the simple *in-situ* method described in the previous chapter. In a seed-mediated process, the final morphology of the particles produced is dependent on the initial seed-particle structure. In this chapter, two methods for producing silver nanorods are tested and analyzed to determine whether they have the required properties for use

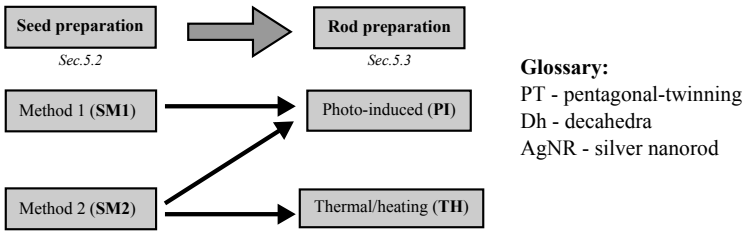

Figure 5.1: Schematic outline and glossary for silver nanorod experiments in this chapter. Two different methods for preparing decahedral nanoparticle seeds were used from Zhang et. al. [71] (SM1) and Pietrobon et. al. [68] (SM2). Two different rod growth procedures were used, with the photo-induced method primarily being adapted from Zhang et. al. [71] (PI) and the thermal rod growth procedure from [69] (TH).

as TERS probes after growth/attachment at the apex of an AFM tip. To improve the work throughput, this study will not focus on the attachment of the particles to AFM tips, but instead on solution based synthesis. This allows UV-vis absorption spectroscopy to be used to analyze the optical properties as averaged across a large number of particles. This can then be compared with TEM results of nanoparticles to analyze the detailed structure and assess the reproducibility of the techniques.

The electron microscopy setup consisted of a JEOL 2100F TEM with a Gatan Orius CCD camera. Samples were prepared on holey carbon film copper grids or silicon window grids (Agar) by drying solutions in ambient conditions. Ocean Optics USB4000 and Red-tide spectrometers were combined with a halogen/deuterium light source (Ocean Optics DT-MINI-2-GS) for acquiring the UV-vis extinction spectra (as shown in figure 5.2).

For later experiments, a series of custom LED reactors were built, each containing four identical LEDs thermally coupled with a heatsink to allow high power operation. Each reactor had a different peak wavelength, to investigate the effect of different excitation wavelength (405 nm, 510 nm, 550 nm, 610 nm and 720 nm). Figure 5.3 shows photographs of one reactor, with spacing to allow a cuvette of the particular nanoparticle solutions

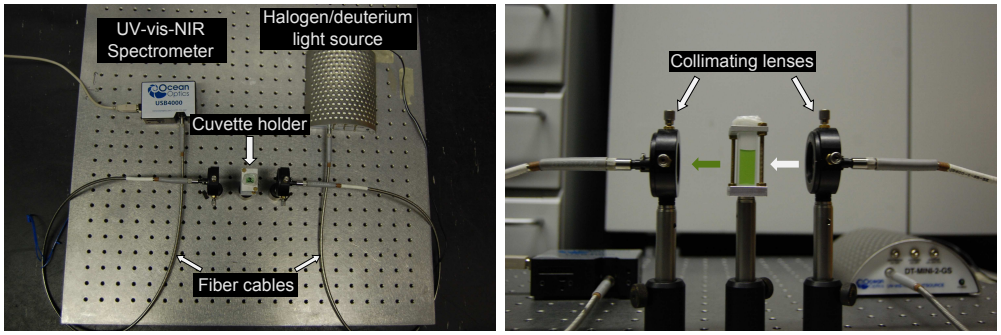

Figure 5.2: Photograph of the UV-vis-NIR spectrometer used for extinction/absorption measurements of nanoparticles dispersed in a liquid cuvette. A halogen/deuterium light source is used for extensive UV-NIR spectral coverage, and Ocean Optics spectrasuite software used for calibration and acquisition of the spectra.

being used. The reactors were placed in the box shown and closed off during the growth procedure, except for particular intervals when time–course absorption spectra were obtained. The LEDs were powered by a variable bench power supply in constant current mode, typically supplying between 100-200 mA.

Analysis of the TEM images was performed using semi-automated par-

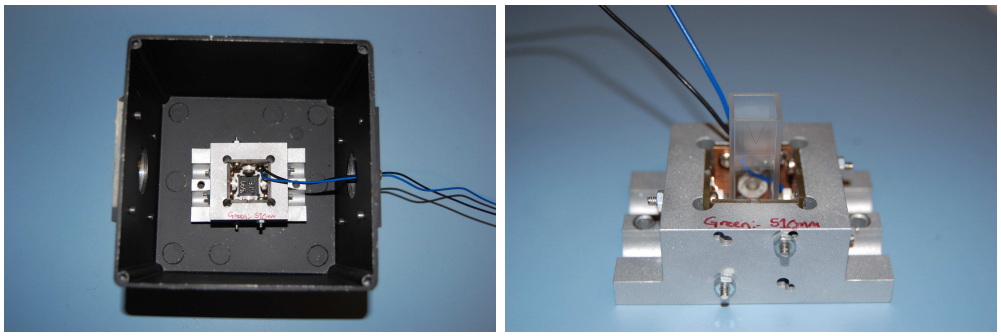

Figure 5.3: Photographs of an LED reactor for synthesis of silver nanoparticles. The reactor is designed to allow a single cuvette of nanoparticle solution to be placed as close as possible to the four LEDs, to allow maximum use of the LED irradiance. The left photograph shows the container for the reactor, which is sealed during a growth procedure to prevent any background light interfering.

ticle detection macros in ImageJ. This consisted of thresholding via user input, then detecting particles with areas no larger than 15nm^2 (for sphere, this corresponds to particles approximately 4.4nm in diameter) which were

typically not possible to distinguish from noise in the images. Using the particle analysis macro, the area of the thresholded region of the particles was taken as seen in figure 5.4 (b), as well as both rectangular bounding box fitting and ellipse fitting (figure 5.4 (d)).

As the noise in the images at high resolution causes the particle borders to become blurred, the area taken from the threshold will be an underestimate of the true value. However, in most cases the area is a good approximation to the particle size. The particle diameters were estimated from the area for particle with aspect ratio close to unity. For elongated nanoparticles, a fitted ellipse was used for width and length estimates, from which the aspect ratio can be calculated.

An image containing the labeled outlines of the particles detected was also

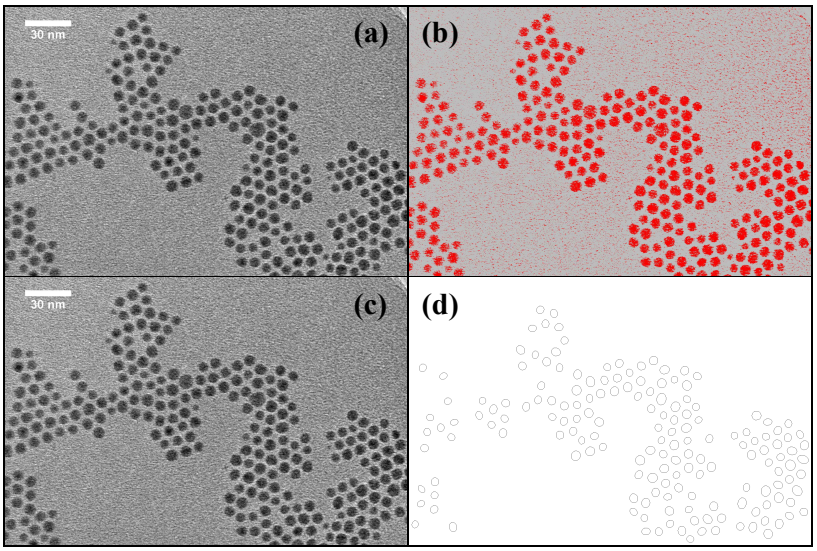

Figure 5.4: Stages in the analysis of TEM images of silver nanoparticles. Original image shown in (a) is manually thresholded to produce a binary image shown in (b). Particle detection and size analysis is then performed using built-in ImageJ routines, and an outline of the detected particles is shown in (c) (overlayed onto the original image for comparison.). Other analysis can be performed, such as fitting ellipses to detected particles, as shown in (d).

produced for each image included in the analysis, as seen in the example shown in figure 5.4 (c). This labeling allowed each data point to be linked back to the exact particle measured.

It should be noted that due to the simplicity of the particle thresholding and analysis, images in which particles are aggregated, or very closely packed together were difficult to analyze. In these cases, images were selected in which most particles did not overlap, and had good contrast against the background. Further work could be performed on the images omitted in this analysis, by using advanced edge detection and segmentation procedures.

5.2 Size and Shape Control

5.2.1 Preparation of Nanoparticle Seeds

SM1 Protocol

The first seed-based method investigated was that proposed by Zhang et. al. in [71] (referred to as SM1). Here, small spherical seeds with PT defects are produced by irradiating a precursor solution under a UV lamp. The SM1 initial solution is composed of 19 mL of de-ionized water, 0.4 mL of 0.01 M $AgNO_3$, 0.4 mL of 0.01 M bis(p-sulfonatophenyl)–phenylphosphine dihydrate dipotassium salt (BSPP), 0.2 mL of 0.1 M trisodium citrate and 1 mL of 0.1 M sodium hydroxide (NaOH). This was combined in a quartz round-bottomed flask and irradiated with a hand-held UV lamp (peak wavelength 254nm) for 30 minutes to induce the formation of the seeds, with the solution turning a bright yellow color when this was successful. Following this, the particles were centrifuged at 15,000 rpm for 60 minutes to separate out the desired small seeds, which were then re-dispersed in 20 mL de-ionized water.

This was repeated as described above, with a Harrier 1880 centrifuge used for the separation of the seeds. However, due to the high centrifugation speed and time, the full process was performed in multiple shorter 10-15

minute steps due to overheating of the equipment. The centrifuge chamber was cooled to 10°C to delay the overheating. No visible changes to the nanoparticle solutions were seen when cooled to this temperature.

Initially the seeds were investigated using APTES-coated silicon-window

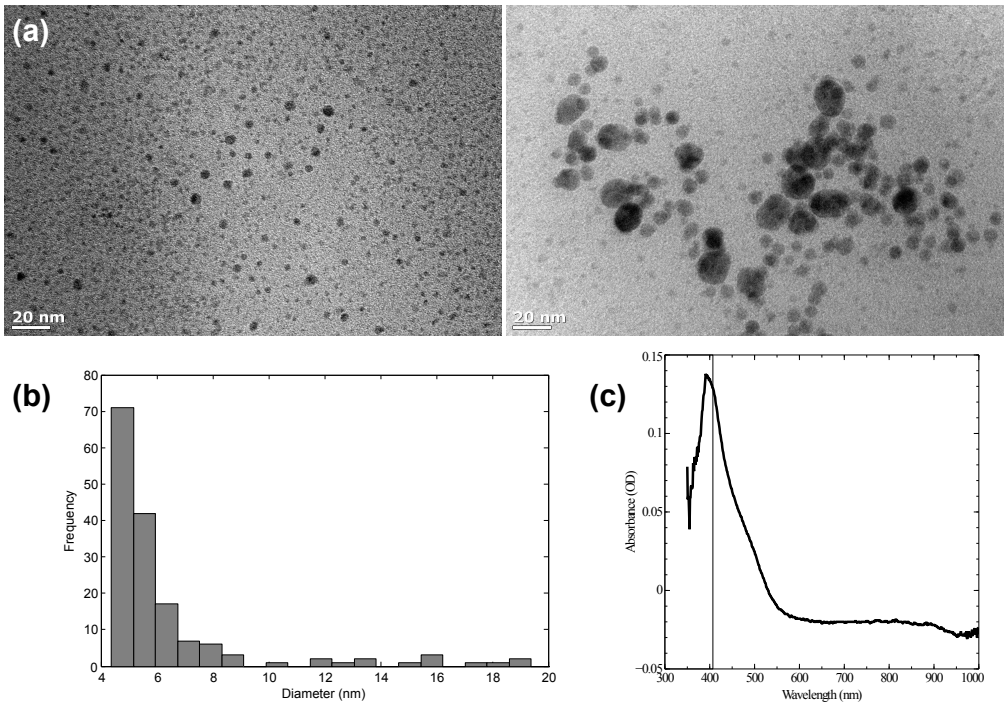

Figure 5.5: Seeds prepared by the SM1 protocol using 254nm UV light and deposited onto APTES coated silicon grids without centrifugation. Typical examples of TEM images are shown in (a), and a histogram of particle diameters is shown in (b). The corresponding UV-vis spectrum of the solution is shown in (c).

TEM grids, in order to match the substrate properties to those of the AFM tips used previously. Figure 5.5 shows nanoparticles prepared without centrifugation. It can be seen from the TEM images and histogram that there is no average particle size above the detectable limit, but that the majority of particles are less than 10nm in diameter and roughly spherical.

In contrast to this, figure 5.6 shows spherical particles with a highly monodisperse size after being centrifuged at 15,000 rpm for 15 minutes four times. This matches the results presented by Zhang et. al. closely. However in the TEM images presented in figure 5.6 it is difficult to confirm

that the seeds have a PT structure. Also, it should be noted that the dipolar plasmon peak in the UV-vis spectrum at 405nm is also much sharper than that of the seeds before centrifugation.

The results shown in figures 5.5 and 5.6 used silicon-window TEM sam-

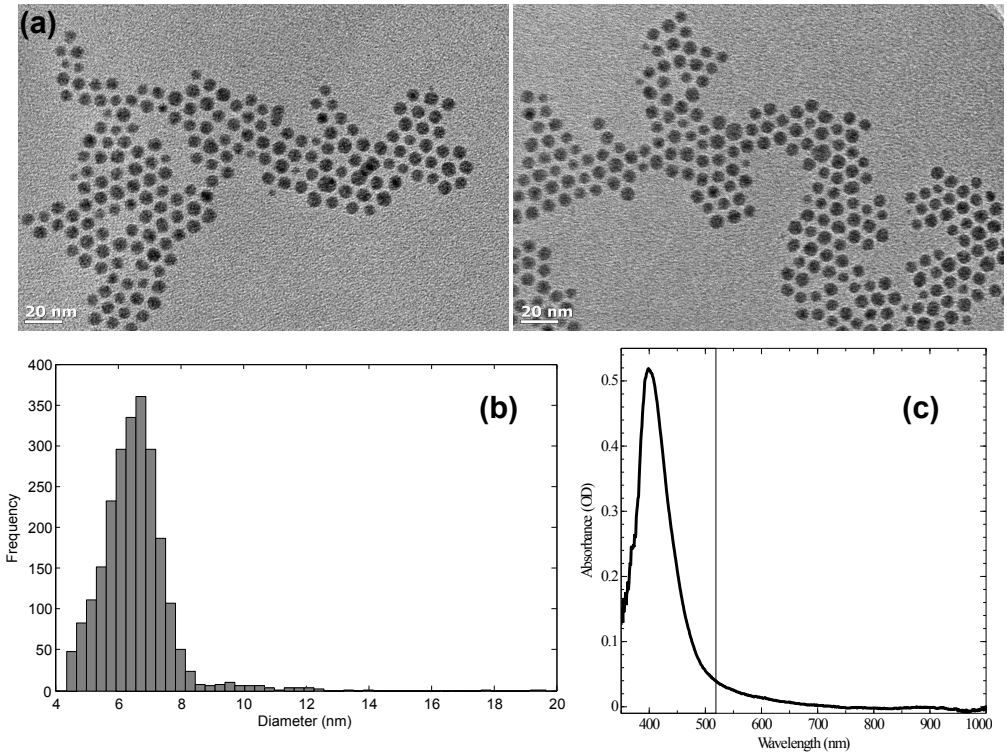

Figure 5.6: Seeds prepared by the SM1 protocol and deposited onto APTES coated silicon grids after centrifugation for 1 hour. Typical examples of TEM images are shown in (a), and a histogram of particle diameters is shown in (b). The corresponding UV-vis spectrum of the solution is shown in (c).

ple grids. However these were found to break easily, and for the analysis of dried particle solutions, these sample grids were not necessary. All further TEM results were performed on holey carbon film copper sample grids which were more suitable for this purpose.

The transformation of the solution from the initial mixture of components through the UV–light–mediated formation of PT seeds was investigated next. Figure 5.7 shows TEM images of the dried initial solution containing large aggregates of particles. When irradiated with UV-light, these larger

particles are thought to break down providing silver ions for the formation of seeds.

Following this, the initial solution was exposed to two different UV light

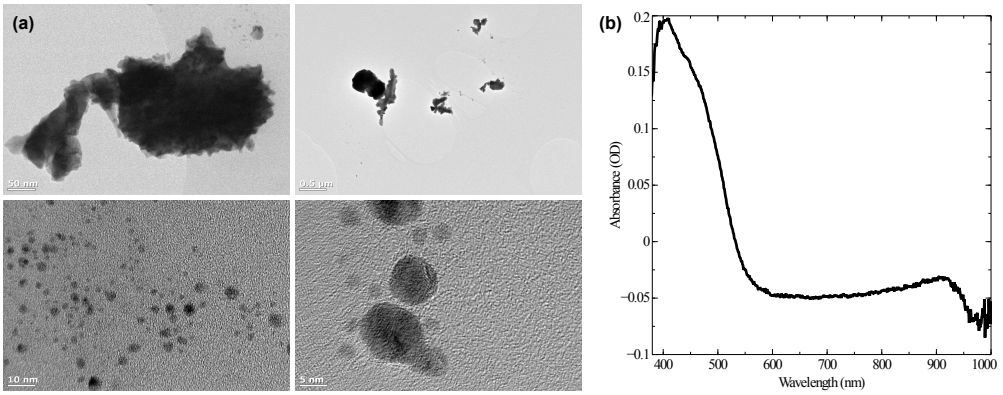

Figure 5.7: SM1 solution before any irradiation. TEM images (left) show large (>100nm) aggregates in addition to smaller particles. The corresponding UV-vis spectrum is shown on the right (note: negative values of optical density are due to a calibration error).

wavelengths, 254nm and 365nm, for varying lengths of time. The results in figures 5.8 and 5.9 indicate similar results, with the majority of particles observed in all TEM images having diameters less than 30nm, and which increase slightly with increased exposure time. Also, it can be seen in both results that a significant number of particles with the required PT defects are present. The majority of particles are also roughly spherical, with the exception of the 15 hour exposure with 365nm UV light which produced triangular plates and other non-spherical particles. These other particles are thought to be produced due to the presence of longer wavelength light in the output of the lamp over longer irradiation times.

In addition to confirmation of the seed particle's PT structure, the effect of centrifugation time was investigated. The protocol in [71] gives no justification for the length and centrifugation speed used. Thus it is desirable to investigate if a shorter centrifugation time will provide a suitable nanoparticle sedimentation for practical use. Figures 5.11 and 5.12

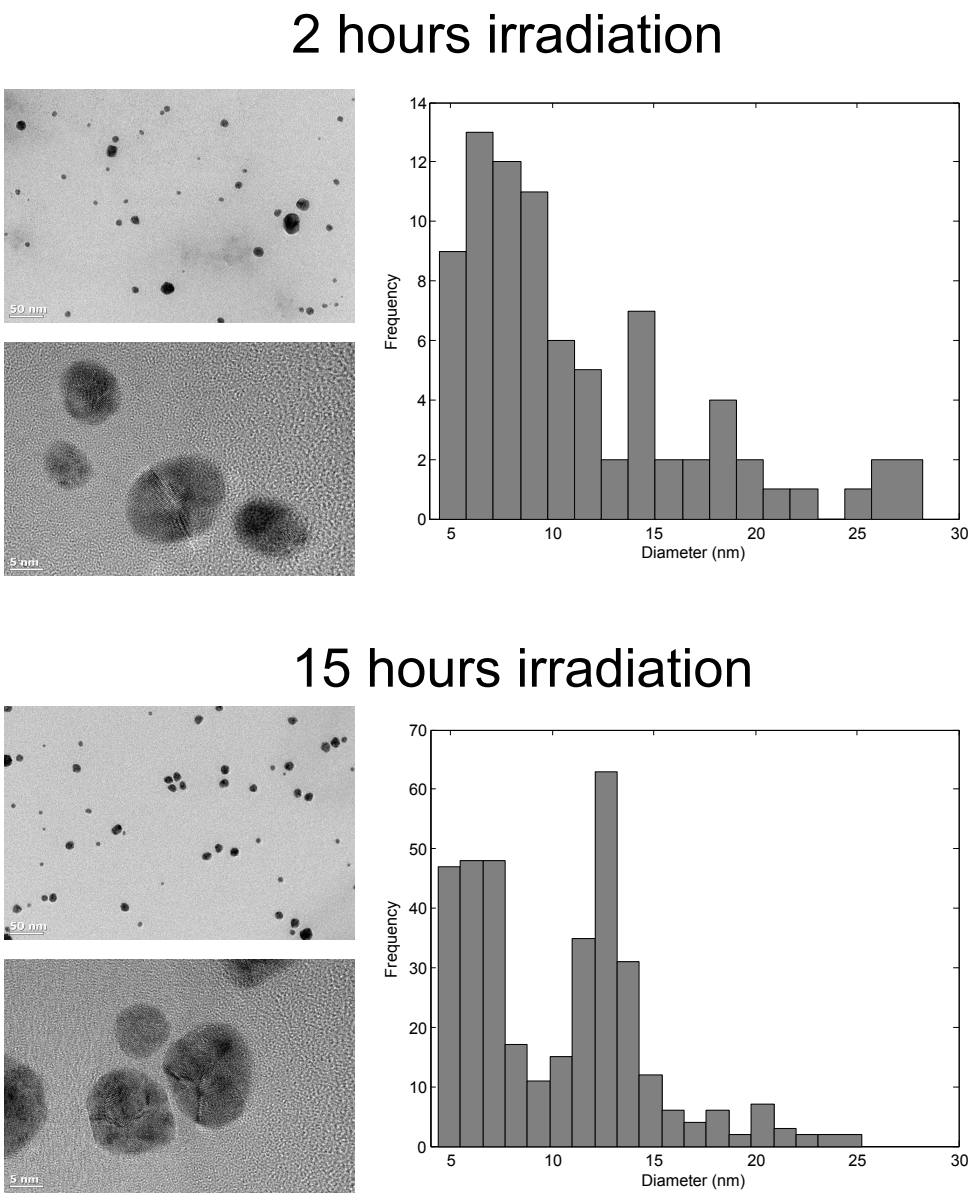

Figure 5.8: Solutions prepared using the SM1 method exposed to 254nm UV light for 2 or 15 hours with TEM images and particle diameter histograms.

show the supernatant and re-dispersed sedimented particles for various centrifuge times (using freshly prepared SM1 seeds prepared under 254nm UV irradiation). After 15 minutes, the supernatant and sediment particle size histograms have no clear difference. However, after two separate 15 minute

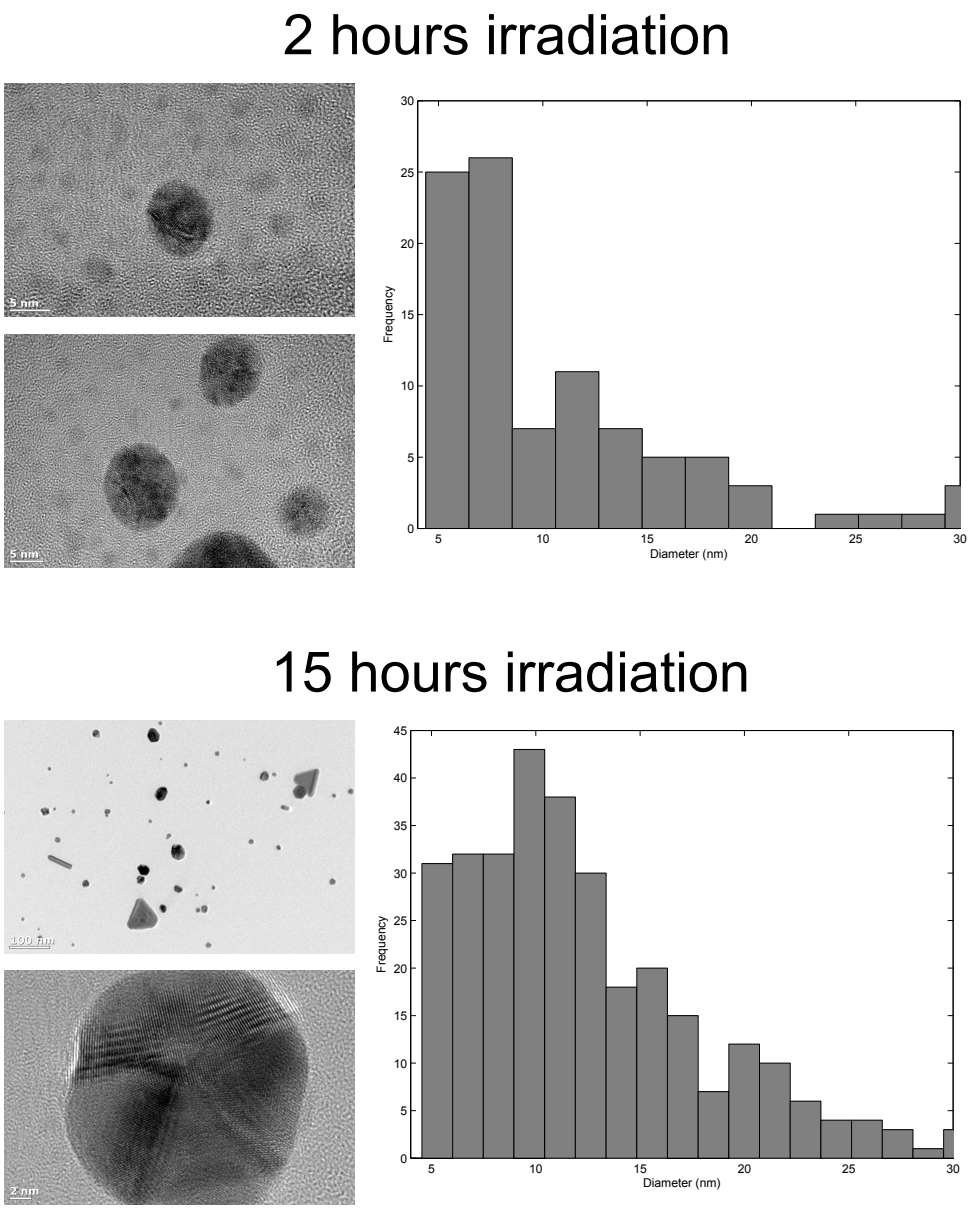

Figure 5.9: Solutions using the SM1 method exposed to 365nm UV light for 2 or 15 hours with TEM images and particle diameter histograms.

centrifugation processes (without removing the sediment in between), it can be seen that the sedimented particles have a broad peak in the size distribution around 8–10 nm. This indicated that a full hour of 15,000 rpm centrifugation may not be necessary, and that a sufficient sedimentation of

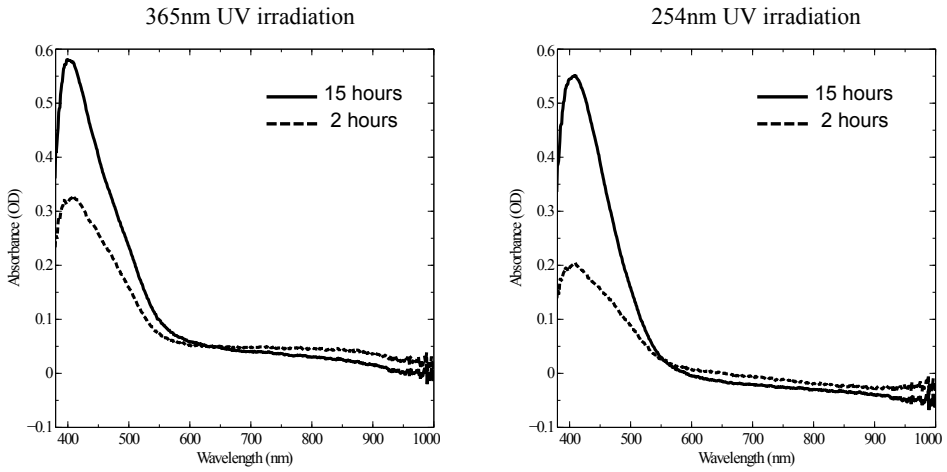

Figure 5.10: UV–vis spectra of particles prepared with the SM1 method after different irradiation times.

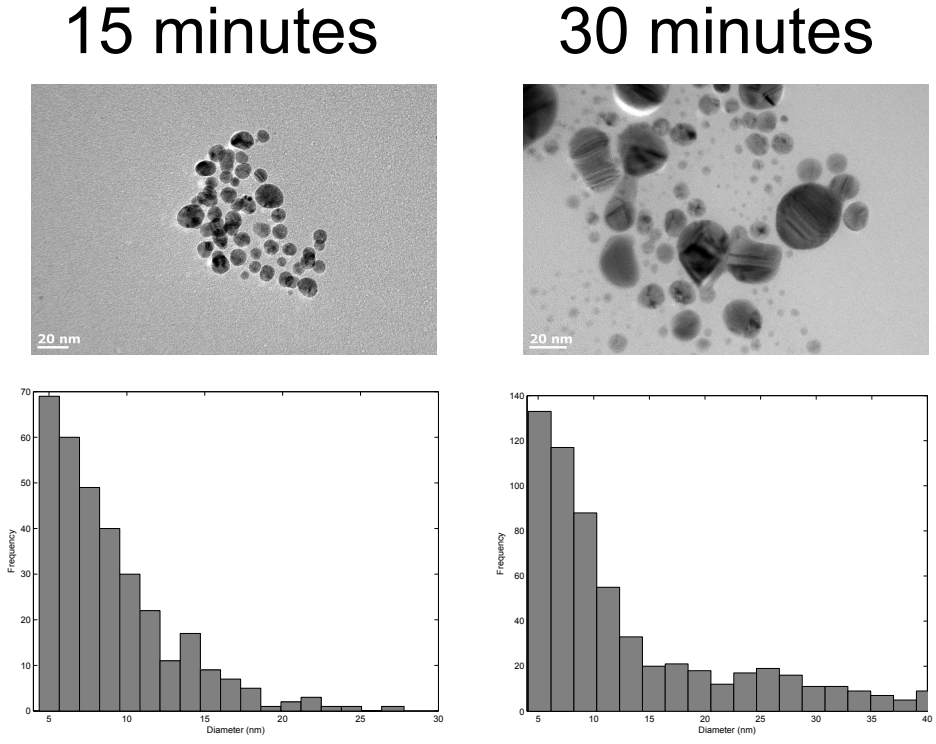

Figure 5.11: Supernatant solution from seeds prepared using SM1 method and 254nm UV-light.

nanoparticles occurs after 30 minutes.

Another possible separation experiment could be tested whereby the sedi-

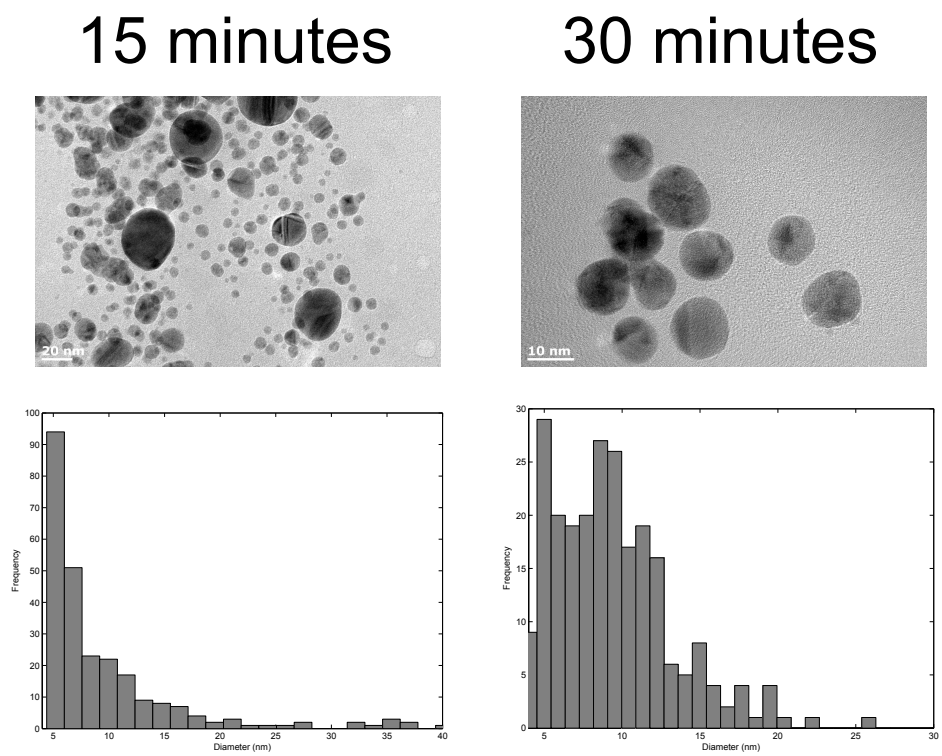

Figure 5.12: Re-dispersed sediment solution from seeds prepared using SM1 method and 254nm UV-light.

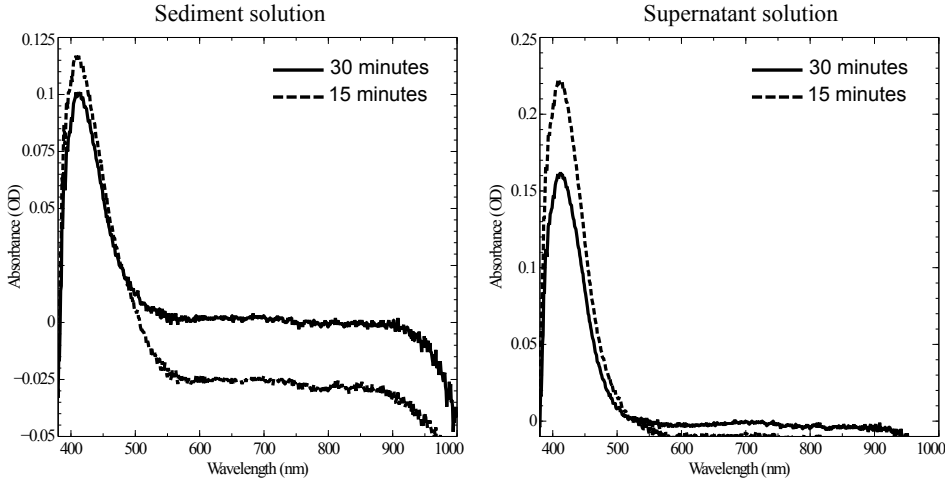

Figure 5.13: UV–vis spectra of nanoparticles prepared with the SM1 method after different centrifugation times.

ment and supernatant of the solution are separated every 15 minutes, and the centrifugation process repeated. This was not done due to the low con-

centration of sediment observed and the small volume of the nanoparticle solution it was possible to centrifuge simultaneously.

SM2 Protocol

An alternative method for producing decahedral nanoparticles was demonstrated by Pietrobon et. al.[68], and in a similar method by Zheng et. al.[70] This involved combining 0.5 mL of 0.05 M sodium citrate, 0.015 mL of 0.05 M PVP, 0.050 mL of 0.005 M l-Arginine, 0.2000 mL of 0.005 M $AgNO_3$, and 7.0 mL of de-ionized water. The resulting yellow solution was stirred using a magnetic stirrer until changing to a darker yellow color. Following this, the solution was exposed to high intensity light, with the wavelength dictating the size of the final particles. The method by Pietrobon et. al. used a 400W lamp with filters, and that by Zheng et. al. used high-power LED irradiation.

The seeds prepared by these methods are larger than those given by Zhang et. al. in [71]. The chemicals used in the processes also differ, with the exception of the silver nitrate and trisodium citrate. Whereas the initial solutions before light irradiation previously contained large aggregates of particles, figure 5.14 shows that the SM2 process begins with the majority of particles with diameters less than 10nm. These particles appear to be of mixed crystallinity, with no preference for PT structure observed prior to light irradiation.

Initially, the solutions were irradiated with a UV lamp in a replication of the experiment described in the previous section for the SM1 method. The results shown in figures 5.15 and 5.16 indicate that the smaller particles from the initial solution (figure 5.14) grow larger with increasing light exposure time. The particle diameter histograms developed a peak between 6-10nm after 15 hours which was not present after 2 hours irradiation. The particle diameters also increased under 365nm irradiation, with a signifi-

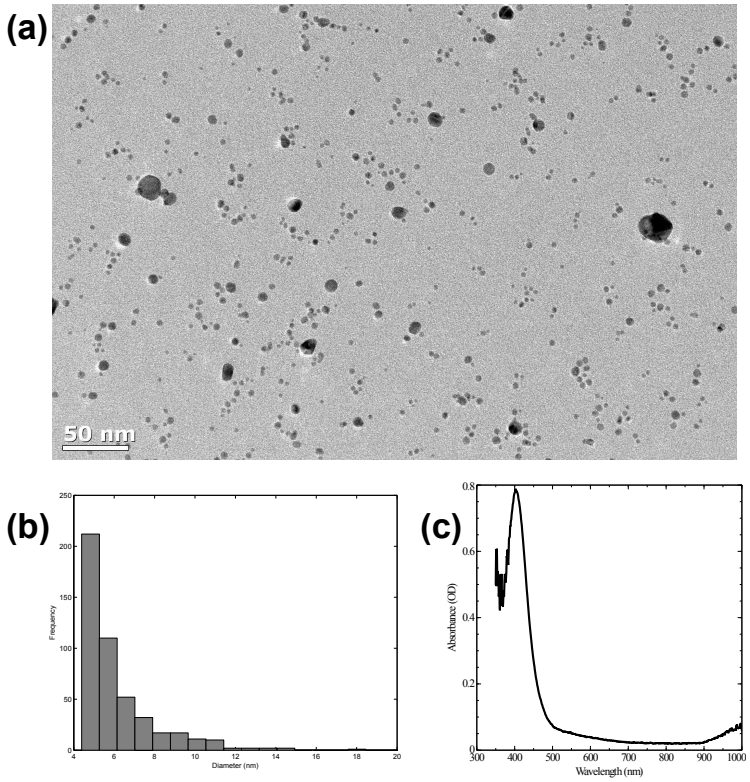

Figure 5.14: SM2 method solution after mixing, prior to light irradiation. TEM image (top), particle diameter histogram (bottom left) and UV-vis extinction spectrum (bottom right) all indicate the majority of particles are less than 10nm in diameter.

cant number of particles with size between 20-40 nm. This supports the dependance of wavelength on final seed particle size as stated by Zheng et. al.[70]

Also observed was the apparent increase in particle crystallinity, with a larger majority of PT particles present after light irradiation. The relative proportions are difficult to quantify using automated particle detection methods, as the PT particles are roughly spherical and of similar diameter to other twinned/crystalline particles. The small changes in particle size also explains the UV-vis spectra which retain the dipolar plasmon peak at 400-420nm. It would be expected that the particles irradiated with 365nm UV-light, which have sizes approaching 20-40nm, to produce a different UV-vis spectrum. However the majority of particles in this solution are

still below 10nm in diameter, and will be the largest contributor to the absorbtion in figurefig:kitSeeds365nm.

In order to investigate the wavelength dependence of this growth pro-

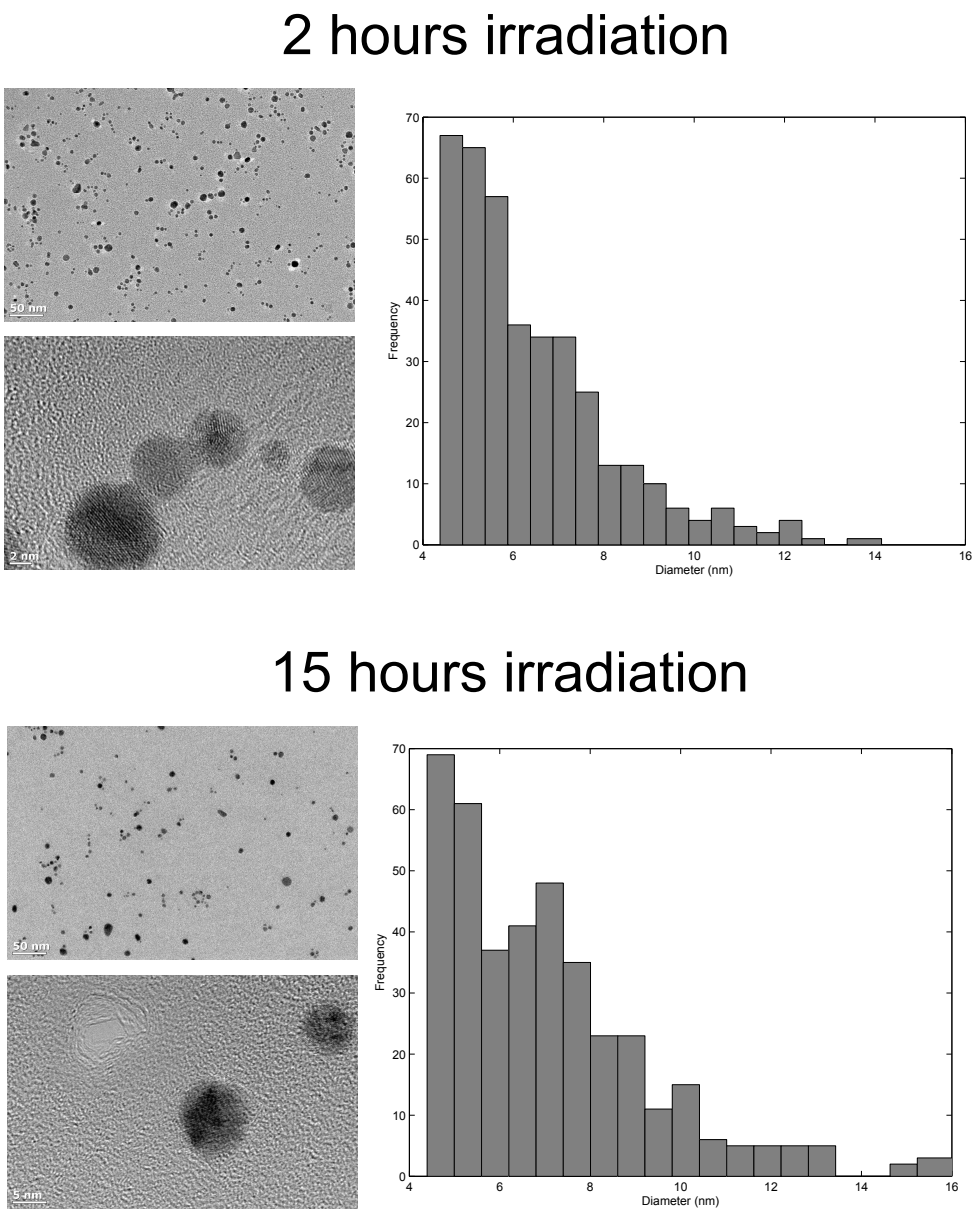

Figure 5.15: Solutions prepared using the SM2 method exposed to 254nm UV light for 2 or 15 hours with TEM, particle diameter histograms and UV-vis spectra. The solid line corresponds to 15 hours, and the dotted line to 2 hours irradiation time.

cess further, a set of high-power LED reactors were constructed with peak

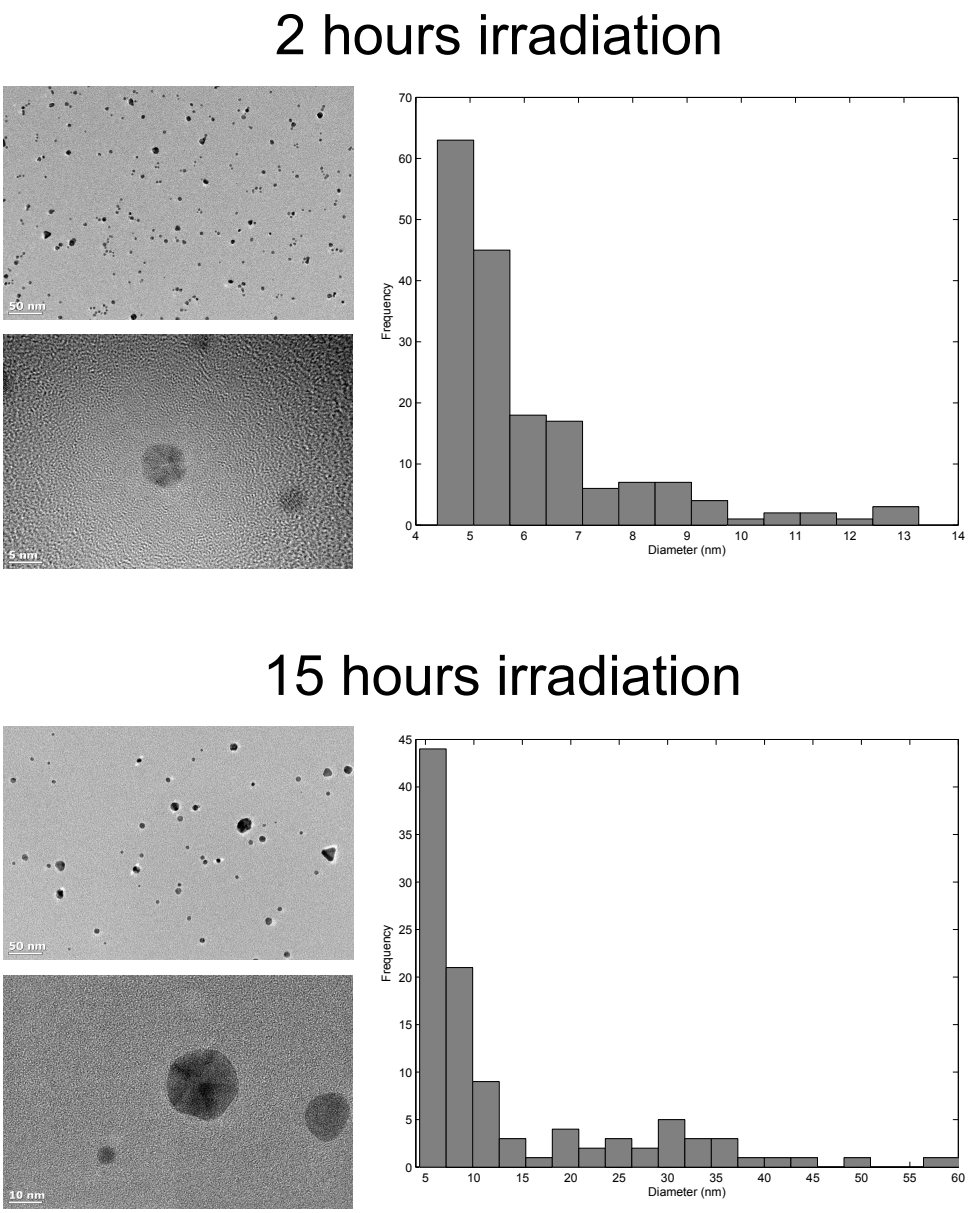

Figure 5.16: Solutions prepared using the SM2 method exposed to 365nm UV light for 2 or 15 hours with TEM, particle diameter histograms and UV-vis spectra. The solid line corresponds to 15 hours, and the dotted line to 2 hours irradiation time.

output wavelengths of 450nm, 510nm, 627nm and 720nm. Zheng et. al. used a similar setup, and found that irradiation wavelengths above 520nm produced a majority of nanoplate particles instead of decahedra. Thus for this section, the seeds were investigated using only the 450nm and 510nm

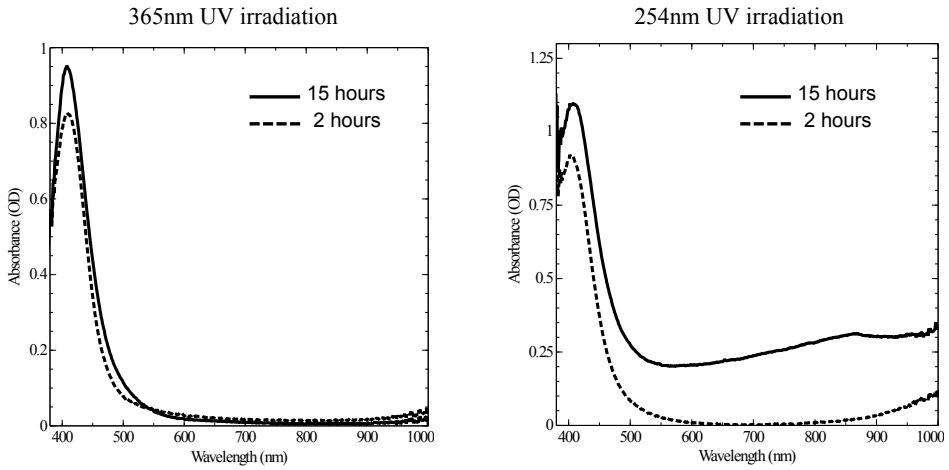

Figure 5.17: UV–vis spectra of particles prepared with the SM2 method after different irradiation times.

LEDs. The longer wavelength LED reactors were used to test the regrowth of rods, and will be discussed in the latter sections of this chapter.

Figure 5.18 shows the results of the SM2 solution when exposed to the 450nm LED light for 16 hours. Particles have a clear Dh shape with PT defects. Additionally, there are also a high proportion of large truncated triangular nanoplates which appear to have single-crystalline structure. The average diameter of particles is noticeably larger than in the previous experiments using UV-light. The particle diameter histogram indicates a broad peak from 30-120nm across all particles. However this is the diameter of both the Dh and plate-like particles. It can be seen that the diameters of the plates are typically larger than the Dh. Pietrobon et. al. state that when a 500nm filter was used, the particle sizes were typically between 35-45nm diamter. Thus it would be expected that the particles irradiated with 450nm light would be slightly smaller than this. While many particles could be classified into this size range, there are also many particles between 50-100nm in diameter. Further analysis must be performed in order to separate the size distribution of the decahedral particles out to be able to conclusively determine the average diameter.

The UV-vis spectrum shown in figure 5.18 shows a shift in the dipolar

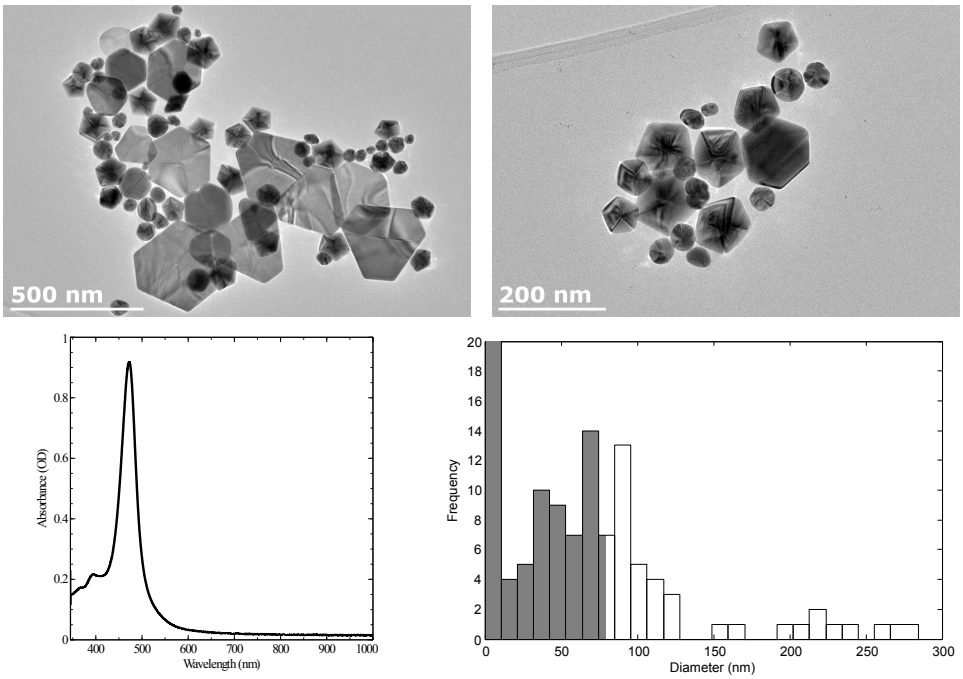

Figure 5.18: Nanoparticles prepared using the SM2 method and LED irradiation at 450nm left overnight. TEM images (top) show a majority of pentagonal twinned particles and truncated triangular plate-particles. The particle size histogram (bottom right) and UV-vis extinction spectrum (bottom left) indicate a noticeable increase in average particle size.

plasmon resonance peak to 480nm. The transition between the yellow initial solutions with their absorption peak at 400-410nm and the final stable peak at 480nm is shown in figure 5.19. The TEM images shown in this same figure are of seeds prepared using the same apparatus, but for a shorter exposure time (330 minutes), and centrifuged for 10 minutes at 15,000 rpm before preparing the TEM samples. The absence of large plate-like particles is noticable, though smaller non-Dh particles are present. This may be due to the difference in exposure time, or the centrifugation process.

Similar experiments using a 510nm LED reactor are shown in figure 5.20. The TEM images again show the presence of larger Dh, however contrary to the results using 450nm, no large plates are observed. This is in disagree-

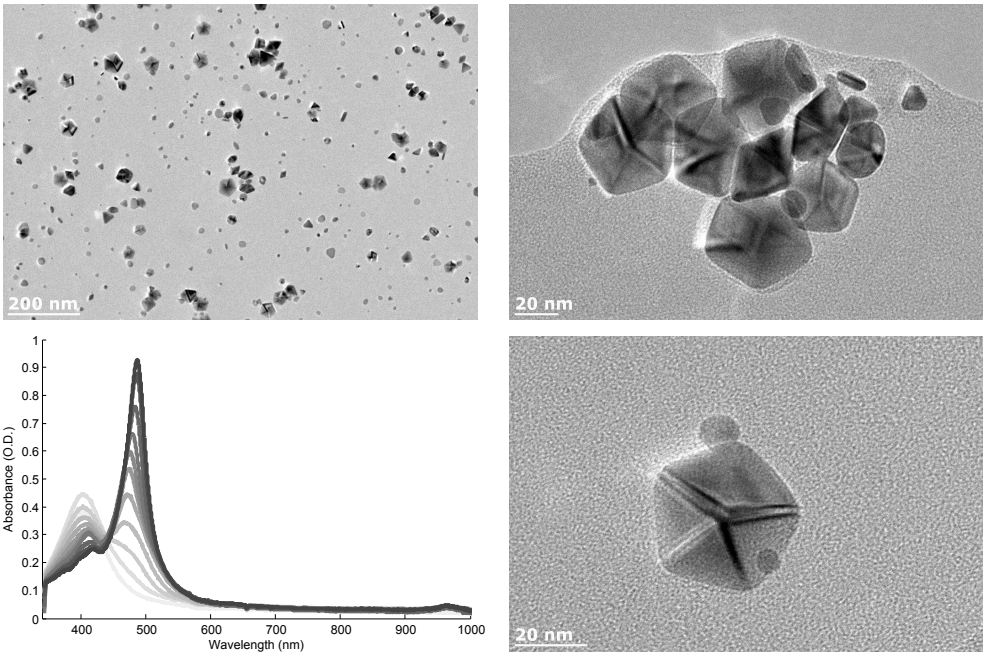

Figure 5.19: Centrifuged SM2 seeds prepared using 450nm LED reactor. TEM images at different scales show a majority of large decahedral particles. The UV-vis time-lapse spectra (bottom left) show the transition from initial seeds to decahedra (Increasing darkness of line indicates increasing time. Final time is 330 minutes.)

ment with the results shown by Zheng et. al. who observe an increase in the proportion of plate-like particles when using 519nm excitation. This may be explained by the inclusion of L-Arginine in the SM2 method, which is absent in the method used by Zheng et. al. The exact role of this chemical is not specified, but it contains amine groups which are thought to bond to the carboxyl group on the protective citrate layers of nanoparticles. Similar chemicals are used in controlled aggregation/modification procedures of nanoparticles.[94] The UV-vis spectrum shown in figure 5.20 shows the final absorption peak to be centered at 530nm, which indicates a larger average particle size. This is supported by the particle diameter histogram which shown a large number of particles with between 40-90nm. Unlike the previous case where there are many plate-like particles, this distribution range appears to be contributed to by mainly decahedral particles.

The time-lapse UV-vis spectra shown in figure 5.21 show the same final po-

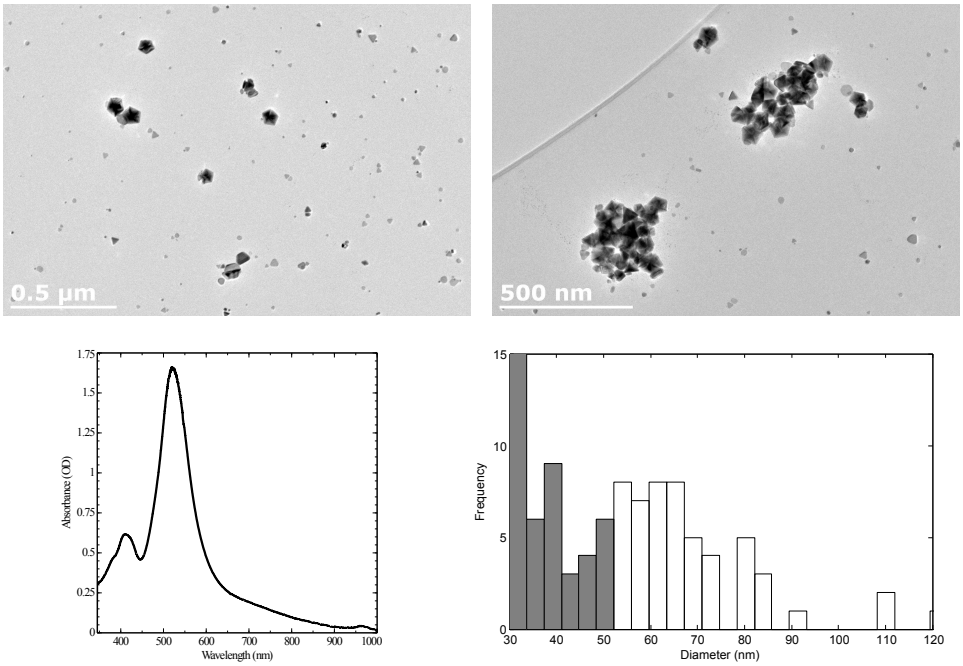

Figure 5.20: Nanoparticles prepared using the SM2 method and LED irradiation at 510nm left overnight. TEM images (top) show a majority of pentagonal twinned particles and smaller mixed-shape particles. The particle size histogram (bottom right) and UV-vis extinction spectrum (bottom left) indicate a noticeable increase in average particle size.

sition for the absorption peak as in figure 5.20. However, the TEM images of the particles centrifuged for 10 minutes at 15,000 rpm show a presence of triangular plate-like particles in contrast to those seen in figure 5.20. This may be due to the different exposure times or other conditions between the two experiments. However a significant proportion of Dh particles are still present, with similar sizes to those seen in the previous experiment using 510nm LEDs. It should be noted that the time-lapse UV-vis spectra of the solutions under different LED irradiation wavelengths showed different approaches to the final stable state. For the 450nm LED irraditaion (figure 5.19), the absorption band shifts from left to right with increasing optical density. However for the 510nm irradiation, the initial peak increases while the other increases from right to left. As the plasmon resonance wavelength

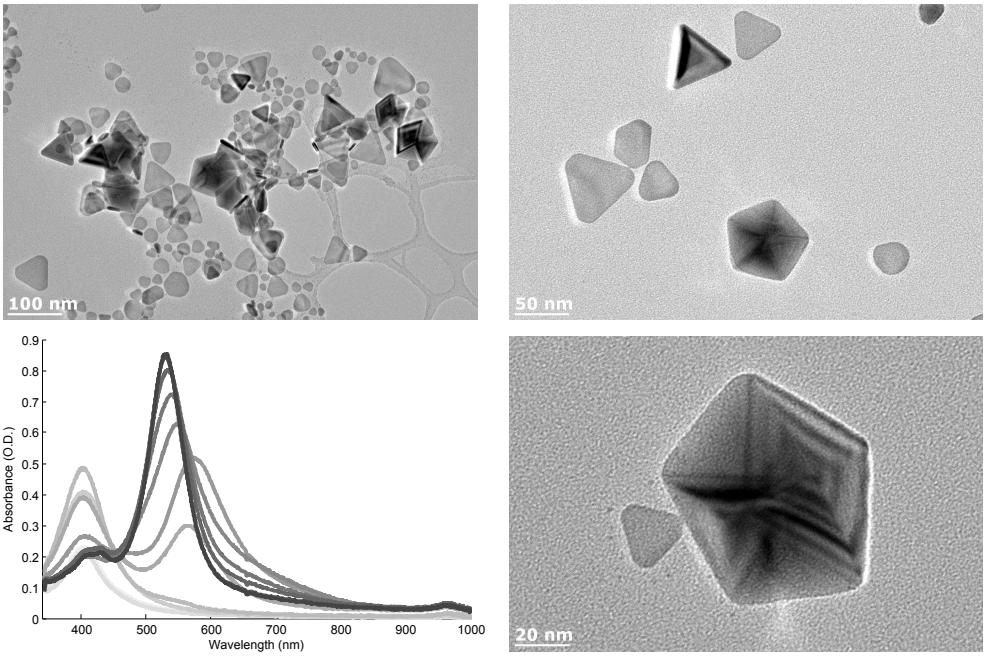

Figure 5.21: Centrifuged SM2 seeds prepared using 510nm LED reactor. TEM images at different scales show a mix of both Dh and plate-like particles. The UV-vis time-lapse spectra (bottom left) show the transition from initial seeds to Dh (Increasing darkness of line indicates increasing time. Final time is 960 minutes.)

is dependant on the particle size, it can be understood that the resonance peak will shift to higher wavelengths as the particle increases in size in the case of growth with 450nm LEDs. The right–to–left shift of the plasmon band doesn't fit with this explanation, but may be due to the presence of other plate-like particles.

5.2.2 Preparation of Silver Nanorods from Seeds

SM1–PI Rod Growth Protocol

The SM1 seeds described in section 5.2.1 were used to produce AgNRs by irradiation with particular wavelengths of light between 600-750nm. This involved preparing a solution with 19 mL of de-ionized water, 0.6 mL of 0.01 M $AgNO_3$, 0.3 mL of 0.1 M trisodium citrate and 0.5 mL of the AgNP seeds. The original PI process used a 150W halogen lamp combined with

optical bandpass filters at 600nm, 650nm, 700nm, and 750nm, with each filter having a bandwidth of ±20nm. The excitation wavelength was used to control the aspect ratio of the NRs at the end of the reaction, with a longer wavelength providing larger aspect ratios. Here, the same PI process was followed, as well as alternative light sources which were tested for comparison.

A similar high power light source and filter setup was constructed as described by Zhang et. al. In [71], the PI reaction under light irradiation appears to take between 5-25 hours, with the reactions at longer wavelengths taking longer to complete. The results in figure 5.22 show the results of an experiment using a 600nm light filter, for a growth solution exposed for 20 hours. This was twice as long as the reaction time given by Zhang et. al. for 600nm irradiation. However it can be seen that no AgNRs are present, but instead a large variety of particles are observed. Figure 5.22 also shows the UV-vis spectrum of the solutions before and after the reaction. While there is a change in the spectrum, no additional peaks are seen at higher wavelength, which would be expected for AgNRs.[69] Particle size statistics are not presented due to the large aggregation of particles in these results. Similar results were seen for other wavelengths but are not presented here.

One possible explanation for the failure to reproduce the results of Zhang et. al. is the intensity of the light used for the reaction. In [71], the power is stated to be 0.2W for a 12mm diameter beam at 1cm from the lamp. This was measured for the repeated experiments, and was found to be lower, but within the same order of magnitude of power. Following this, experiments using the LED setups described in the previous section were attempted using 627nm and 720nm irradiation, with the power output of these LEDs being greater than that given by Zhang et. al. However, similar results were seen for this case (not shown here), with large aggregates formed, and no AgNRs observed.

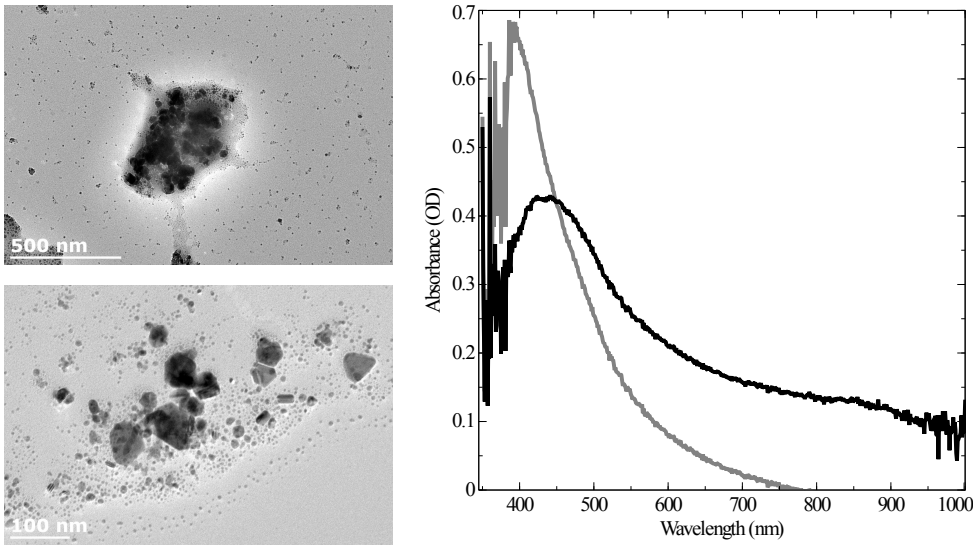

Figure 5.22: SM1–PI method solution irradiated by 600nm light for 20 hours. TEM images (left) and UV-vis absorption spectrum (right). The grey line is the initial solution, and the black line the solution after 20 hours.

SM2–PI and SM2–TH Protocols

The larger PTNPs shown in section 5.2.1 were used by Pietrobon et. al. as the seeds for synthesizing AgNRs in a temperature-controlled reaction. [69] The process involved centrifuging a solution of the seeds to separate the Dh particles, and re-dispersing in de-ionised water to a concentration of 0.33 M. Details of the centrifugation conditions were not given, but attempts using 15,000 rpm for 10 minutes were tried and appeared to give suitable solutions (see figures 5.19 and 5.21). Following this, a mixture of 2.0 mL de-ionised water, 0.400 mL of 0.05 M trisodium citrate and 0.066 mL of 0.05 M PVP were combined and heated to 95° in a glass vial on a magnetic stirrer. Once the solution had reached this temperature, 1 mL of Dh solution was added at the same time as varying amount of silver nitrate (between 0.15–0.20 mL of 0.005 M solution). After 10–15 minutes, this reaction is shown to produce AgNRs with aspect ratio of 4-5. Larger AgNRs can be produced by incrementally adding 0.1 mL of the same silver

nitrate solution every 10 minutes to produce rods with aspect ratios up to 12. Larger aspect ratio rods (up to 40) could be produced by centrifuging the rod solutions and repeating the growth procedure again.

This process was attempted using both the original temperature controlled reaction described above (SM2–TH), and again by using longer wavelength LEDs (SM2–PI). The results using 627nm LEDs are shown in figure 5.23. It can be seen that there are a large number of flat, single-crystalline particles present, as well as smaller spherical particles. The particle diameter histogram in figure 5.23 indicates the smaller spherical particles are roughly 10-30 nm in size, and the plate like particles are distributed between 40-140 nm. This is reflected in the UV-vis spectrum which has a large, broad peak at 760nm at the end of the reaction, thought to originate from the larger nanoplates. A smaller peak is also still present close to 410nm, which is likely to originate from the smaller spherical particles. Similar results were observed for both 510nm and 720nm LED irradiation.

The presence of nanoplates could be explained using the results observed by Zheng et. al. who observed the formation of triangular plates when using longer wavelength light. The silver nitrate solution added to the solution, intended to be used as a source for regrowth of AgNRs, could instead preferentially form these plate structures. The Dh particles added to the solution are likely to be the smaller spherical particles observed.

Following this, the SM2–TH procedure for forming AgNRs was tested. The same procedure as described above was carried out, with 1-3 repetitions of the growth process carried out using SM2 seeds grown with 510nm LED irradiation. TEM results from one stage of growth appeared not to contain a significant number of AgNRs (results not shown here). However, after three repetitions of the growth stages, the solution appeared to change in color and became more turbid. The TEM results shown in figure 5.24 show this solution contains a significant number of AgNRs, with varying aspect

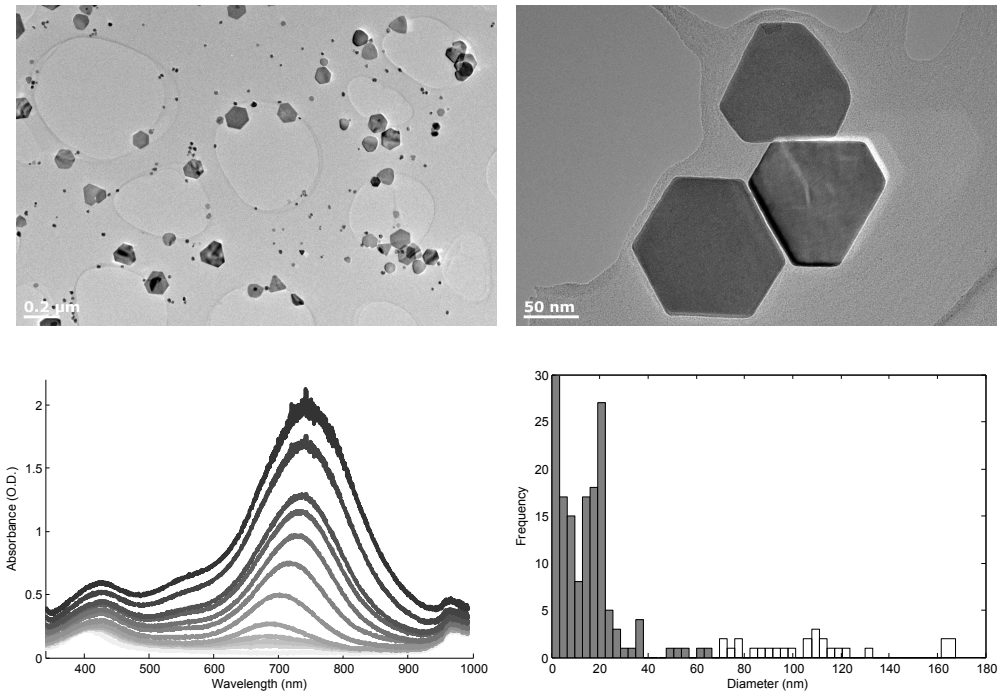

Figure 5.23: SM2–PI rod-growth solution using 627nm LED irradiation. TEM images (top) show the presence of both small spherical particles and larger flat truncated triangular particles. The UV-vis absorption time-lapse (bottom left) shows the evolution of the seeds to the initial solution (darker lines indicate increasing time). Particle diameter histogram (bottom right).

ratios. The nanorods shown in these TEM images were not centrifuged after the thermal growth process, and represent the solution immediately after growth.

The particle size analysis of these rods involved fitting an ellipse to each detected particle, and taking the minor and major axis as a rough estimate of the width and length of the rods respectively. It can be seen in figure 5.25 that most particles have a width (minor axis) between 20–80 nm, which suggests this is determined by the initial size of the decahedral particles, in agreement with Pietrobon et. al. The length (major axis) has a less uniform distribution, with lengths between 40–300 nm. In accordance with this, the aspect ratio histogram only contains significant numbers up to an aspect ratio of 8-10. The UV-vis spectrum of this solution shows a broad

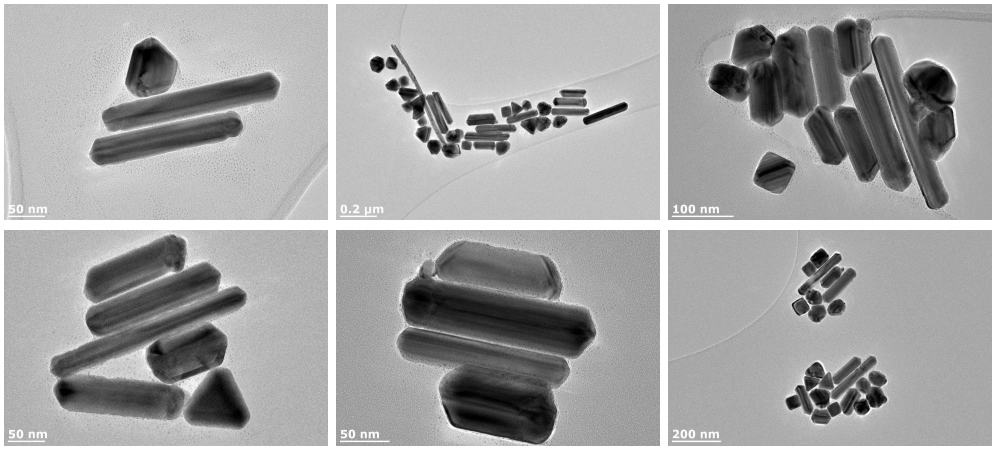

Figure 5.24: Various TEM images from the SM2–TH method solution after three repetitions of the incremental thermal growth process.

extinction peak, explaining the turbid appearance of the solution.

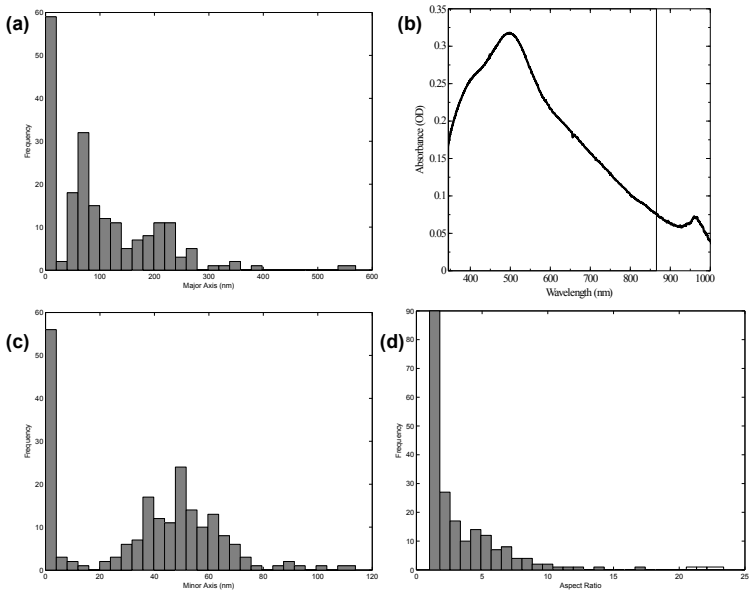

Figure 5.25: AgNR particle statistics and UV-visible spectrum (top right) corresponding to the nanoparticle solution after three repetitions of the growth process.

5.3 Summary and Discussion

The results presented in this chapter indicate a controllable synthesis of PT nanoparticle seeds using light-induced reactions is possible. The size of the seeds can be controlled by appropriate selection of the wavelength and centrifugation. However, the subsequent regrowth of these seed particles into AgNRs using PI processes was not successful. Thermal regrowth of seed particles into rods using the SM2–TH method appears to be successful, though the application of this to an *in-situ* growth process of TERS tips would be more difficult to implement.

One possible problem with the SM1–PI rod growth may be the solution of BSPP, which was observed to degrade after several days, indicated by a change from a transparent solution to light yellow. The role of this chemical in the process is not entirely understood, but it has been used in previous photochemical nanoparticle experiments forming other nanoparticle geometries by Zhang et. al. as a photo–reactive ligand. Understanding the role of BSPP in these experiments may be useful for understanding the failings of the SM1–PI synthesis of AgNRs.

Other problems with this method are the difference in energy between the excitation wavelength (typically red to infra–red wavelengths) and the plasmon resonance of the particle seeds at 400–410 nm. The long-wavelength light will have a negligible absorption when incident on these nanoparticle seeds. It is not understood how the red light causes a plasmon-mediated reaction to form AgNRs using the SM1–PI method, as the energy transfer between the light and nanoparticles will be negligible. This may again be dependent on the photo–reactive BSPP compound.

PI growth using the seeds produced using the SM2 procedure resulted in the formation of nanoplates, which can be explained by the results seen in [70]. However, replication of the SM2–TH growth procedure was suc-

cessful for producing rods. The procedure required three repetitions of the silver nitrate addition step before AgNRs were formed, which is not in agreement with Pietrobon et. al. This may be due to the use of larger seeds prepared by the 510nm LEDs, which would require a larger volume of silver ions to be added to the solution before noticeable growth into rods. These results pose several questions when considering their application to TERS probes. PI synthesis is attractive for growth *in-situ*, but growth using rods appears to be difficult. While the Dh particles would be feasible for use as TERS probes, they would lack the desired aspect ratio for providing the additional lightning-rod enhancement effect.

An alternative method could use the SM2–TH growth of rods, which are then controllably attached to AFM tips. As the ends and sides of the AgNRs are thought to have different protective ligands, it may be possible to exploit this for controlled orientational attachment of the nanorods to surfaces. An alternative method may be to first attach the seeds followed by thermal growth into rods.

Future work should focus on controlling the attachment of the nanoparticles to substrates using controlled surface modification, as well as improving the final solution of nanorods prepared thermally. The latter could be done using the suggestion in [69] of adding 10 μL of 0.1M KOH prior to the addition of the seed particles, which improved the yield of the rods. Two suggested approaches are shown in Figure 5.26.

Another potential experiment is the investigation of multiple switched-wavelength irradiation of solutions to produce nanorods. As already mentioned, the SM1–PI method for producing rods used wavelengths far from the plasmon resonance of the particles. If the growth was initiated by light of a wavelength slightly higher that of the plasmon resonance band, the particle should grow and the resonance wavelength would increase. As

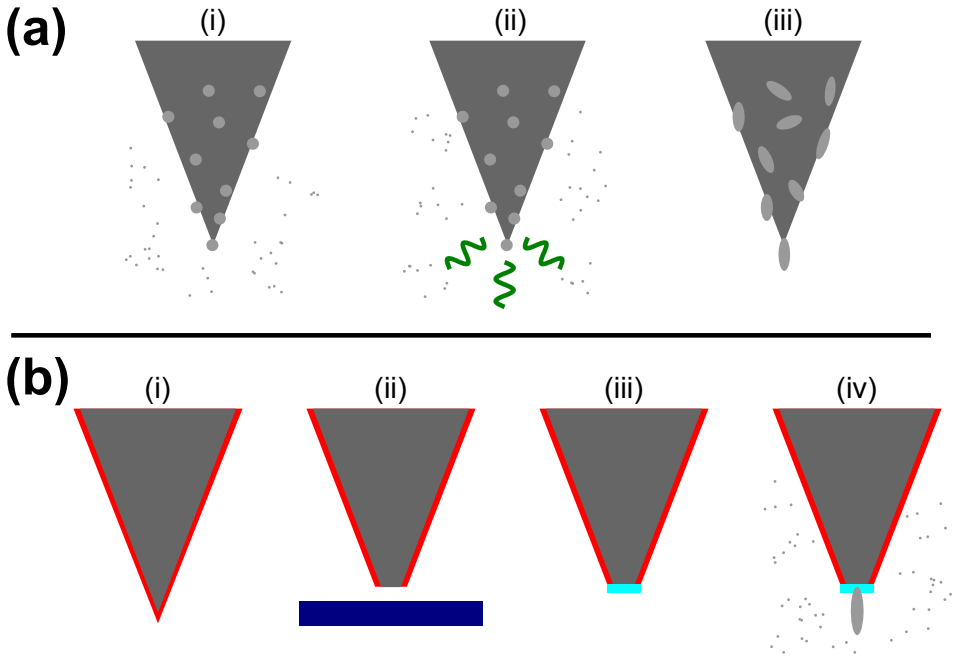

Figure 5.26: Two suggested pathways for attaching nanoparticles to AFM tips for TERS. (a) shows the in–situ growth of attached particles into rods by light (though the mechanism in (a-ii) could equivalently be a thermally induced reaction. (b) suggests a mechanism whereby a substance used to repel nanoparticles is first applied to the tip in (b-i), and then the tip apex blunted by harsh AFM scanning (b-ii). Following this, the exposed region at the end of the tip can be coated with a nanoparticle promoting surfactant, and subsequently ready–prepared nanoparticles can be attached from solution.

this occurs, the initial light could be switched off, and a higher wavelength switched on, continuing the growth. However this may simply produce larger spherical particles as there is no orientation preference in solution. However, with the anisotropic nature of the PT seeds and appropriate, well understood selective protective ligands, it may be possible to preferentially produce AgNRs via regrowth.

6. The mechanical properties of FF tubes studied by PRMS-AFM

6.1 Introduction

Nanoscale structures are prevalent across biology, and are required for many of the most basic functions of life. Since the invention of the first microscope, the natural world at a small scale has been accessible for study, and has facilitated major developments in medicine with the discovery of viruses, bacteria and other cellular organisms. As technology has progressed, microscopy has become more sophisticated and complemented by other techniques. In addition to observation, samples can be controllably perturbed and their response measured. This allows properties such as mechanical strength and elasticity to be measured, which can be useful not only for applications, but fundamental understanding of these structures.
Proteins are an important class of biomolecules fundamental to the operation of living cells. Their conformation is determined by structure at different length scales, the so called primary and secondary (and higher order) structures. The primary structure refers to the sequence of any of the 20 amino acids that form a linear chain which has a repeated "peptide backbone" molecular structure seen in Figure 6.1. The secondary structure depends on the nature of the side chain groups 'R' in the peptide chain, and how they interact with other peptide strands. The Ramachandran angles shown in Figure 6.1 are often used to determine this secondary structure. Note that the angle θ almost never varies between peptide chains, thus

only ψ and ϕ are required. The two most common secondary structures

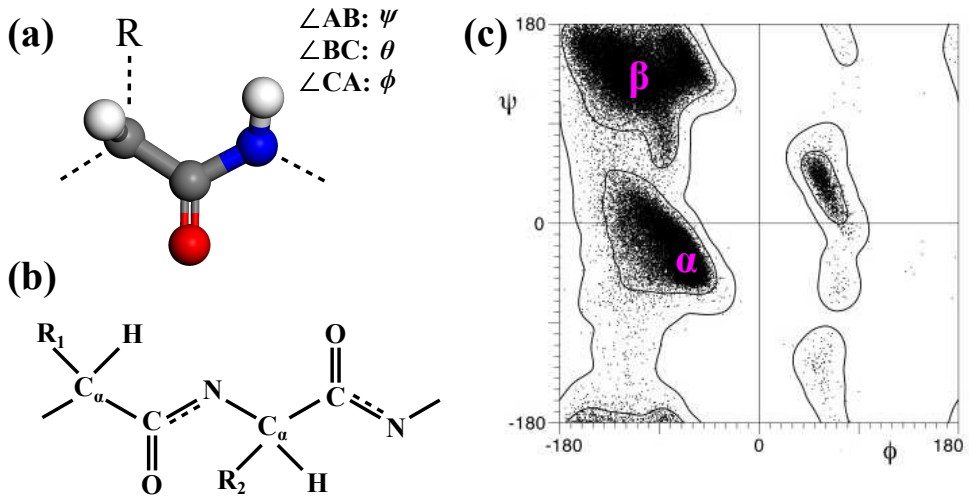

Figure 6.1: Schematic of peptide backbones. (a) shows the basic backbone unit, with 'R' being a functional group defining one of the 20 amino acids. The angles between the three planes A, B and C are known as the Ramachandran angles, and define the secondary structure. (b) shows a repeated backbone unit, with different side groups labelled R_1 and R_2. Note that the carbon atom in the backbone attached to the side chain is commonly referred to as C_α. (c) shows a Ramanchandran plot of ψ vs. ϕ for general proteins (modified from [95]). The two most common secondary structures, α–helices and β–sheets are marked in the plot.

are α–helix and β–sheet, the Ramachandran angles for which are shown in figure 6.1 (c). The β–sheet conformation occurs in two conformations called parallel and anti-parallel, shown in figure 6.2. These are distinguished by observing the relative directions of the peptide backbones between the two strands, for example the N–C_α–C chain repeats in the same direction for parallel, whereas anti–parallel repeats N–C_α–C for one strand and N–C–C_α in the other. As a peptide backbone is typically linear, a β–sheet peptide chain will often turn back on itself in order to form such conformations.

The peptide backbones are hydrogen-bonded between the carboxyl and amine groups for β–sheet conformations. Additional bonds may occur due to the side-chains R, depending on their properties, which can affect the way in which the peptides assemble in different environments (pH, different solvents etc.). These properties define the typical roles of particular amino

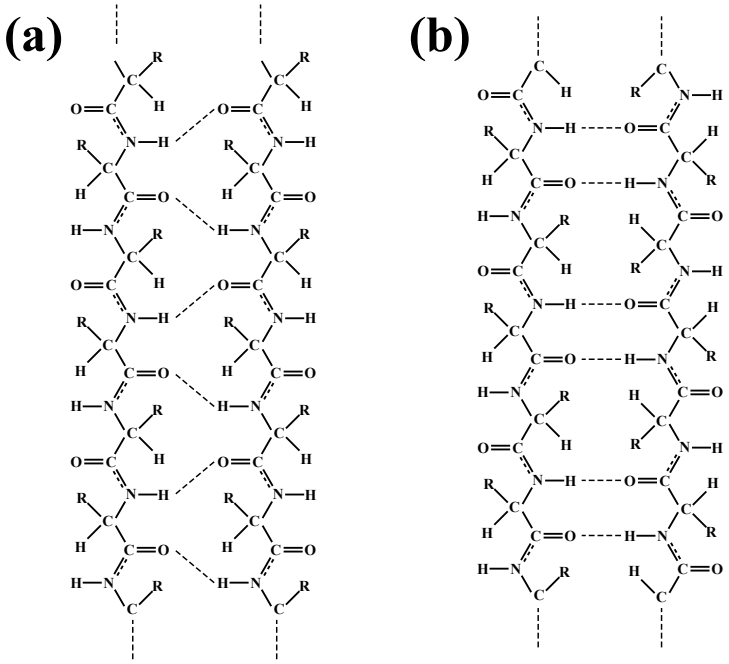

Figure 6.2: β–sheet peptide conformations: (a) parallel–sheet and (b) anti-parallel–sheet.

acids in a protein, for example non–polar hydrophobic groups are typically found at the interior of proteins, and are responsible for their structure, while polar side chains are usually found on the outside of proteins, and dictate their metabolic and reactive properties.

Proteins are ubiquitous in living cells, as they are versatile and can be used for a variety of cellular functions such as membrane receptors, cytoskeleton anchors and enzymes for catalyzing chemical reactions. An important set of structures are the amyloid proteins, which are insoluble non–branching fibrous aggregates with a β–sheet secondary structure.[96] These are often linked with diseases such as Alzheimer's, Parkinson's and Huntingdon's disease, but are also studied for their unique material properties. In particular, the amyloid–β (Aβ) structures are one of the most mechanically rigid biomaterials known. The two most common forms of Aβ consists of a sequence of 40 or 42 amino acids (called Aβ_{40} and Aβ_{42} respectively),

which self-assemble into a polypeptide fibril. It has been suggested that a key component of this sequence for the self-assembly is the aromatic diphenylalanine (FF) segment (A$\beta(19-20)$).[97] Synthetic FF peptides can self-assemble into fibrils, which have been increasingly studied as they have a wide range of potential applications as Aβ models, and as rigid biologically compatible nanomaterials.[98]

X–Ray diffraction has been used to study the self-assembled FF fibril structure on large scale aggregates.[99] Polarized Raman microspectroscopy (PRMS) has also been used to study the structure for smaller FF micro– and nanotubes (with the tube size measured by AFM), which found the structure to be in agreement with the X–Ray data.[87, 88] The work presented in this chapter will present work utilizing the PRMS system combined with AFM to measure and explain the origin of the rigidity of the FF tubes.

6.2 Literature Review

6.2.1 Diphenylalanine peptide tubes

Diphenylalanine molecules can be made to self-assemble into tubes using the fluorinated polar solvent 1,1,1,3,3,3-hexafluoro-2-propanol (HFIP), which will dissolve the hydrophobic FF powder crystals. The self-assembly of the tubes can be induced by mixing the HFIP–FF mixture with de–ionized water, a process which happens in several seconds. The resulting mixture can be seen in figure 6.3 (a), and subsequently dried onto a glass slide in (b) and it can also be seen that the tubes have a large persistence length compared with their diameter.

The structure of large crystalline aggregates has been studied by X-Ray diffraction[99] which suggested that the FF molecules form a circular chain of six FF molecules, with the phenyl rings facing out and the peptide backbone facing inwards, as seen in figure 6.4 (b). These form a single

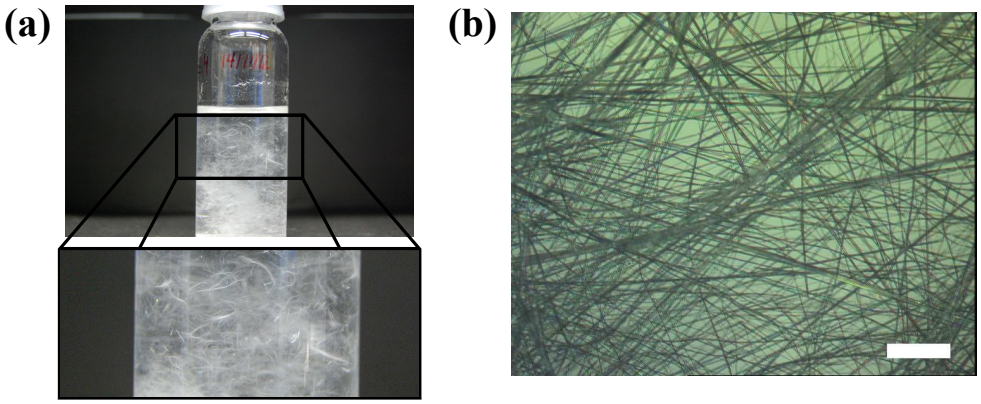

Figure 6.3: Diphenylalanine peptide nanotubes. (a) shown as white fibrous strands in aqueous solution. (b) micrograph of solution in (a) dried onto a glass coverslip (scale bar 130 μm).

nanotube when this ring is repeated in the direction perpendicular to the plane of the circle and held together by hydrogen bonds, as seen in 6.4 (c). Larger tubes can be produced by packing individual nanotubes together hexagonally, bonded by aromatic interactions between the phenyl rings. The X–Ray study was performed using a 0.540×0.020×0.018 mm FF fiber at 105 K.[99] To determine if the structure of smaller micro– and nano–tubes was the same, PRMS studies were performed by Lekprasert et. al. which allows the orientation distribution function of certain vibrational modes to be measured. In particular the amide I and amide III modes of vibration (shown in figure 6.5), found at 1690 cm^{-1} and 1249 cm^{-1} respectively, were analyzed. The peak positions of these bands in the Raman spectra suggested that the N–H, not the C=O was involved in hydrogen bonding. Various applications have been suggested and demonstrated for FF tubes. They were first demonstrated as a nanoscale "cast" for making nanowires by reducing silver ions inside the channels of the tubes[101]. The FF material could then be removed through the use of an enzyme, leaving silver nanowires as shown in figure 6.6. As FF tubes are relatively rigid but also biologically compatible, they have been suggested for various uses

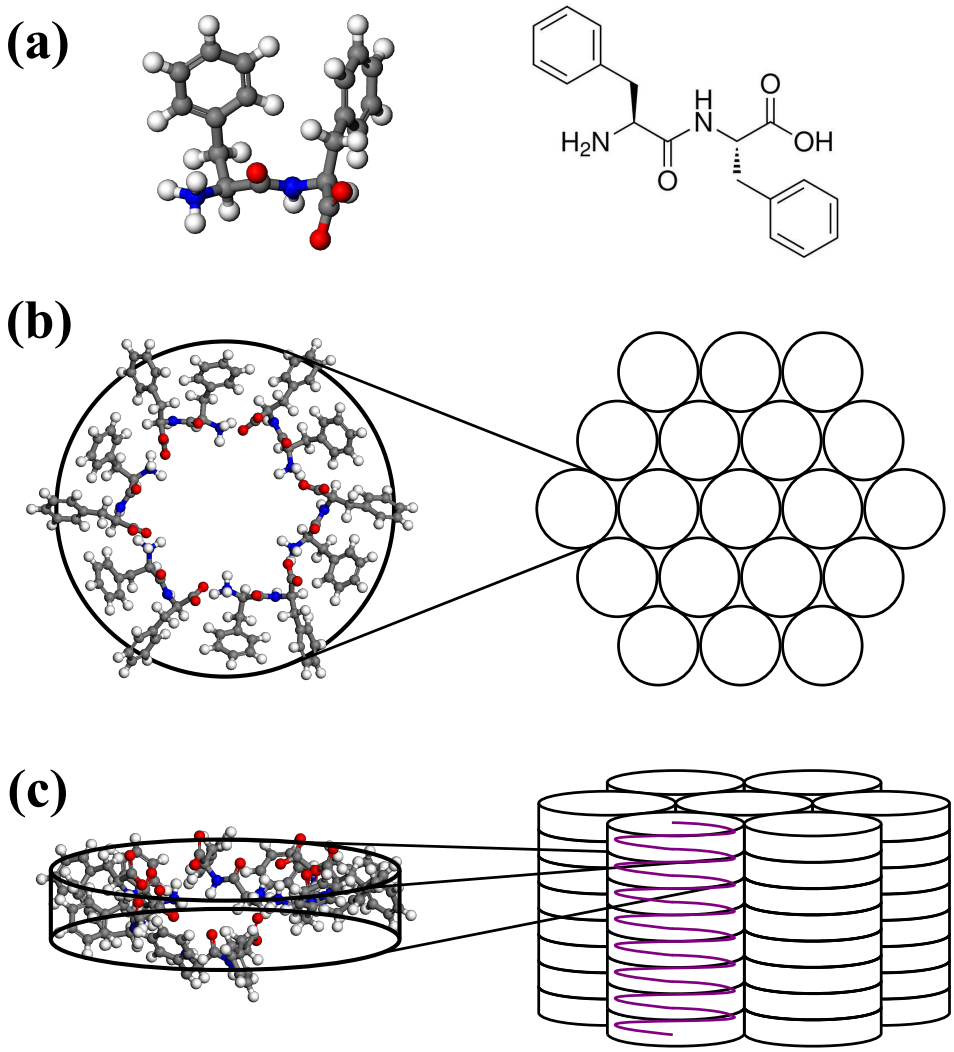

Figure 6.4: Schematic of the proposed structure of self-assembled FF tubes. (a) shows both a ball and stick and line-angle diagram of the L–Phe–L–Phe molecular structure. (b) shows the circular structure formed by six FF molecules, and how each one hexagonally packs together. (c) shows a different angle of the ring, and how it stacks together along the tube axis.

in bioengineering. One example is for use as a cell scaffold in tissue engineering, which has been demonstrated by Jayawarna et al.[102] where a self-assembled FF peptide hydrogel (see figure 6.6 (c)) was shown to support living chondrocyte cells. FF tubes may also be applicable in novel forms of cell transport. It was shown by Yan et al. that FF tubes with electrostatically bound DNA can be converted to vesicles which are readily

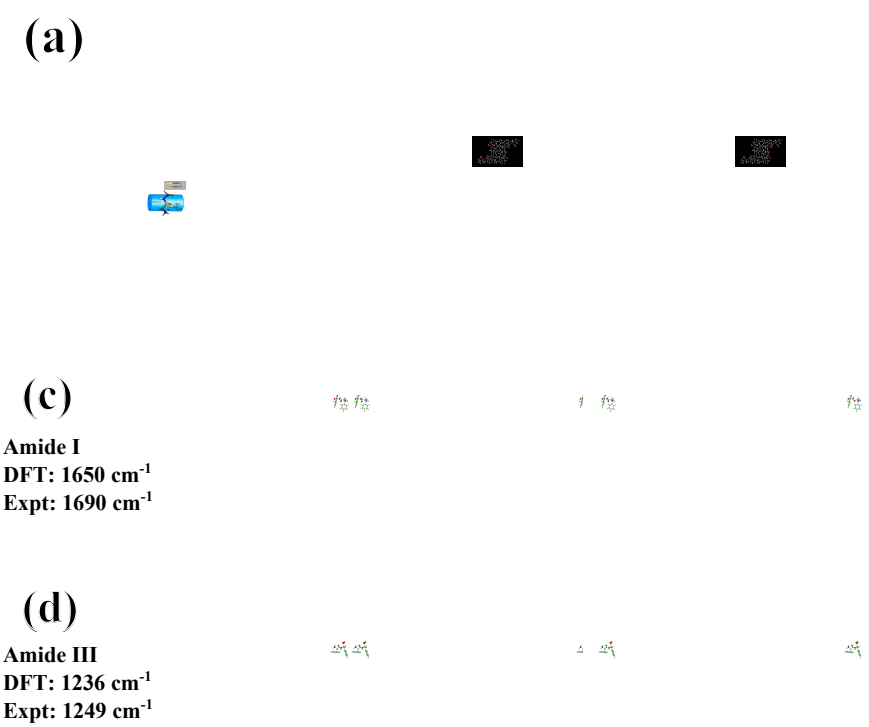

Figure 6.5: (a) Results of PRMS measurements used to determine the orientation distribution function of the amide I and III bands from nano– and micro–tubes (modified from [88])(b) Crystal unit cell for FF tubes as determined from X-Ray diffraction (atomic co-ordinates taken from supplementary information of [100] which uses the X–Ray data). The lattice parameters are $|\vec{a}| = |\vec{b}| = 23.89$Åand $|\vec{c}| = 5.38$Å. . Snapshots from animations of the DFT simultation (left to right) carried out by Lekprasert et al. in [88] of the amide I and III modes ((c) and (d) respectively).

absorbed by cells (see figure 6.6)[103].

6.2.2 Measurement of the strength of FF tubes

As FF tubes have a variety of potential applications, it is important not only to understand their molecular structure but their response under various physical conditions. One important property of the tubes is their mechanical rigidity, quantified by their elastic or Young's modulus, which is the ratio of an applied stress, σ, to the resulting strain, ϵ, produced along

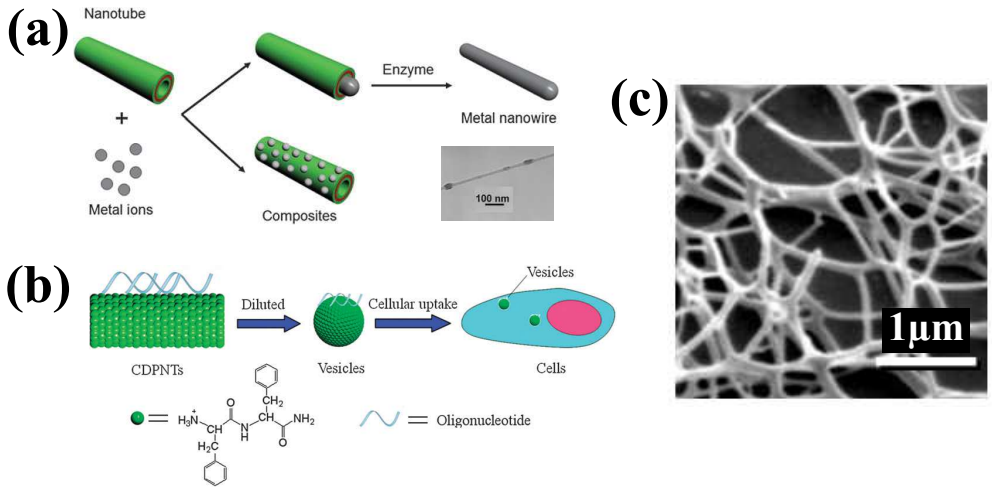

Figure 6.6: Applications of FF nanotubes. (a) shows a schematic for casting silver nanowires using FF tubes (modified from [98]). (b) shows the use of FF tubes for conversion into vesicles which are used for intracellular transport of oligonucleotides/DNA (modified from [103]). (c) shows an SEM image of an FF tube hydrogel for use as a cell scaffold(modified from [102]).

an axis

$$E = \frac{\sigma}{\epsilon} = \frac{F/A}{\Delta L/L_0} \tag{6.1}$$

where the symbols shown above refer to those displayed in figure 6.7 (a). It can be seen that materials with a higher E will be more rigid as for a fixed stress, as E is inversely proportional to the strain. In material sciences there exist a multitude of instruments which are used to measure the stress/strain relationship for macroscopic materials, however these are not suitable for individual micro– and nano–scale structures. As AFM involves a physical probe which can not only be used for imaging but for manipulation, it is a useful tool for studying materials in these circumstances. In the case of FF tubes, two approaches utilizing AFM have been demonstrated, one using indentation measurements with a stiff cantilever shown by Kol et al.[104], and the other using a bending beam theory applied to a suspended tube which is pressed by the AFM tip by Niu et al.[105].

The indentation method involves measuring the spring constant of the can-

tilever, and then acquiring force spectra on the peptide tubes. The combination of the cantilever and the elastic response of the tube can be modeled as two linearly coupled springs, the contributions of which can be separated if the cantilever spring constant (k_{can}) is known, and the combined spring constant (k_{meas}) measured from force spectra. The equation for the nanotube spring constant k_{nano} is then $k_{nano} = k_{can} \cdot k_{meas}/(k_{can} - k_{meas})$. To convert k_{nano} to Young's modulus, finite element simulations were used to measure the constant of proportionality between k_{nano} and E (assuming a linear relationship between them). This resulted in $E =\approx 19$ GPa as an upper limit, with models of hollowed–out peptide tubes clearly having moduli lower than this.[104]

The method which utilizes a bending beam theory for FF tubes, derived from the more generally applicable Timoshenko beam theory[106], concerns the deflection of a beam suspended across a gap which is subject to stress at a specified point. This theory incorporates both bending and shear deformations (δ_B and δ_S respectively) into a total deflection $\delta = \delta_B + \delta_S$ measured by AFM (see figure 6.7). The bending beam model was used by Niu et al, to measure the Young's and shear moduli for individual FF tubes [105]. This was done by depositing already-assembled tubes onto an AFM calibration grid which consists of arrays of square holes of well-defined size. AFM topography can be measured for suspended tubes, and the tip then positioned above the midpoint of the tube for force spectra acquisition. The total deflection will be a combination of tip and tube deflection, thus reference force spectra must be used, taken on the tube at the fixed points of the grid, in order to measure the deflection due to the tube only. The applied force is controlled by the setpoint, which can be calibrated using force spectra acquired on a hard (e.g. glass coverslip) sample, and the contact region fitted linearly to find the sensitivity (measured in nm/V). Subsequently the thermal response of the cantilever in free space can be

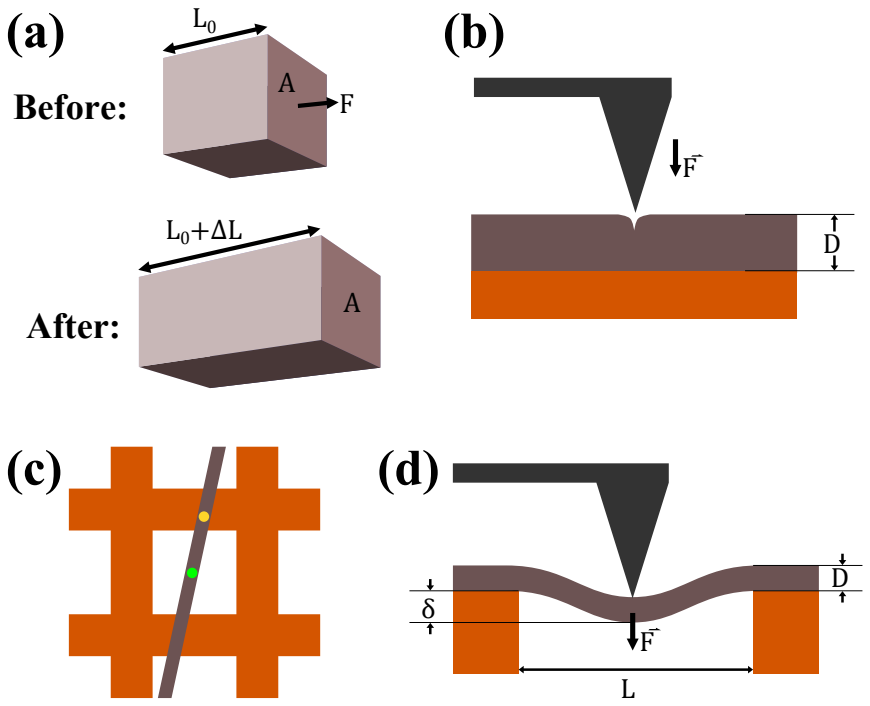

Figure 6.7: Elastic measurements of peptide nanotubes. (a) shows a diagram illustrating the elastic deformation of a material unit with relevant quantities for defining the elastic modulus. (b) shows a schematic for indentation experiments on single nanotubes described in [104]. (c) shows a top down schematic of a nanotube in a bending beam experiment, with a green and yellow circle showing locations for the location of force spectra on and off the suspended portion of the tube respectively. (d) shows a side-view of the suspended beam experiment with the relevant parameters displayed for extracting the Young's and shear moduli from the bending beam theory.

measured, and the resonance used to find the spring constant. This then allows the force setpoint to be expressed in nano–Newtons. The results of the bending beam experiment on FF tubes obtained $E = 27 \pm 4$ GPa, and $G = 0.21 \pm 0.05$ GPa, which are significantly higher than the measurements by indentation. However this value was for a solid tube, and the indentation assumes a hollow tube. The bending beam experiment can also incorporate effects of hollow tubes through the expression for the second moment of area $I_s = \pi(D - D_0)/64$, which will result in a decreased value of E for an increasing inner diameter D_0.

6.2.3 Modeling the mechanical properties of peptide fibrils

The AFM–based techniques for measuring the Young's modulus treat the FF tubes as a linearly elastic continuous medium. However, figure 6.4 shows that at the molecular scale FF tubes clearly have an anisotropic structure, which may affect the validity of such assumptions. In general, peptide fibrils are expected to have anisotropic molecular structures, in the case of amyloid-like fibrils a cross–β sheets structure is prevalent, which is essentially layers of β–sheets (seen in figure 6.2) stacked together. Molecular dynamics and density functional theory simulations can be used to model these structures in greater detail, but are computationally intensive for complex molecular structures. A simple method was suggested by Knowles et al.[107] which uses a coarse-grained model for modeling the strength of peptides. This involves separating interaction contributions due to the peptide backbone and the amino acid side–chains, the former of which is due to hydrogen bonding in most peptide fibrils. The elastic modulus contribution due to these hydrogen bonds along the backbone was modeled using the equation

$$E_{BB} = \delta_\beta \xi k_H \tag{6.2}$$

where δ_β is the inter–sheet spacing, ξ is the bond density and k_H is the bond spring constant. For amyloid fibrils, the values of $\delta_\beta = 4.8$ Åand $\xi = 1/(10 \times 3.5)$ Å^{-2} are fixed, leaving k_H as a remaining adjustable parameter, which was extracted from infrared spectroscopic data of particular amyloid fibrils. Raman spectroscopy has previously been used to investigate hydrogen bonding in FF tubes, and has also previously been used to obtain force constants from peptides more generally by Moore and Krimm in the 1970s.[108–110] Thus Raman spectroscopy may be a useful tool in obtaining information about the force constants in single microscopic fib-

rils for use with this theory. The side–chain contribution to the peptide

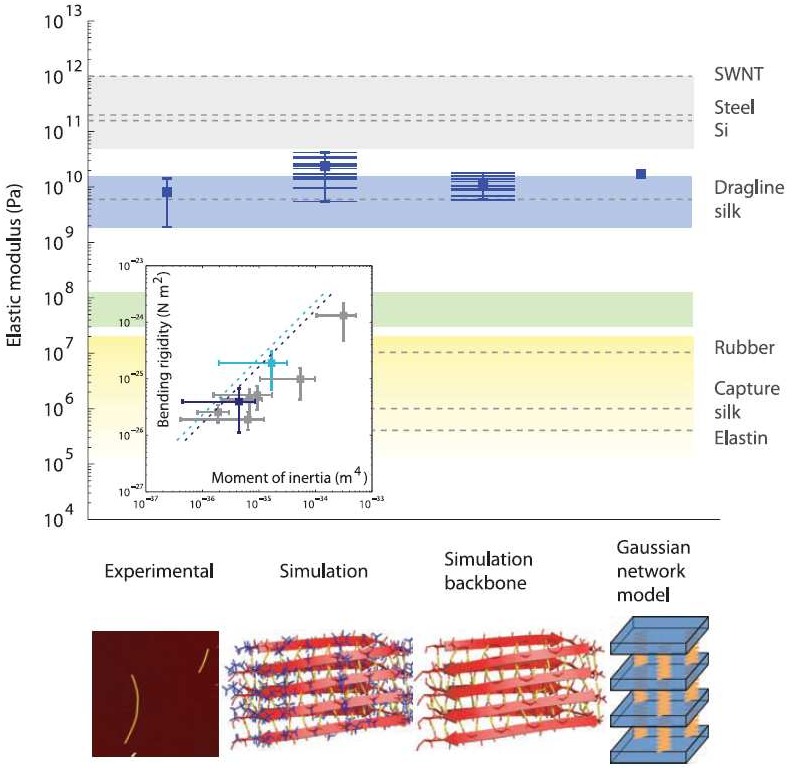

Figure 6.8: Illustration adapted from [107] showing a comparison between experimental measurements of elastic moduli for protein nanofibrils, and different theoretical modeling techniques. The two different theoretical models utilize molecular dynamics (central columns labeled 'simulation') and a simplified coarse-grained Gaussian network model. The elastic modulus for other materials is also shown to illustrate the relative rigidity of protein fibrils.

strength was shown to be two orders of magnitude lower than the contributions from the backbone by modeling the combined interactions between layers as a surface–tension–like effect. The total modulus could then be calculated as

$$E = E_{BB} + E_{SC} \tag{6.3}$$

where E_{SC} is the side-chain contribution to the modulus.

The work by Knowles et al. measured the values of the Young's modulus using AFM, by extracting the profiles of the fibrils along their full length. The mean squared displacement could thus be measured, and related to

the estimated modulus by a theory which assumes the persistence length of a fibril will be dependent on the strength of the bonds holding the fibril together along it's long axis. This was shown to be a simple and effective method of obtaining the Young's modulus for amyloid fibrils. For the FF tubes however, as the persistence length is typically very long (much greater than the length of the lateral scanning range of many AFMs), this technique is difficult to apply directly. However, measurement of the mechanical properties can be measured by other force-based AFM techniques, as described earlier. A combined polarized Raman and AFM instrument could thus be used to attempt to measure mechanical properties of the tubes using Knowles' theory (which used force constants from vibrational spectroscopy), and AFM-force measurements to determine the elastic modulus.

6.3 Experiments

6.3.1 Overview

The experiments in this section are composed of two parts, which can be applied to a single isolated suspended FF tube using an integrated AFM-Raman microscope. The first is simply the bending beam experiment as performed by Niu et al. as described in the previous section, except using an empty copper TEM grid window instead of an AFM calibration grid. This difference is required for compatibility with the inverted optical microscope allowing access to the sample from below. The second part of the experiment exploits this difference, by allowing Raman measurements to be performed whilst AFM force spectra are obtained on the suspended tube.

6.3.2 Sample preparation and instrumentation

All peptide solutions were prepared by initially solubilising lyophilised L-diphenylalanine (FF) peptide (Sigma Aldrich) in HFIP (Sigma Aldrich) to give a stock solution of 100mg/ml. Stock solutions were further diluted to a working concentration of 2 mg/ml using de–ionized water. Copper transmission electron microscope (TEM) grids with window size of 19×19 lm (G1000HS, Gilder grids, UK), which have empty windows, were utilized as a support for the tubes. Using tweezers, the TEM grids were pulled gently through a solution of FF tubes so that tubes attached on one side. Immediately after this, the grids were deposited onto a quartz microscope slide (SPI supplies) and air-dried. All measurements were performed using the combined instrument shown in figure 4.1, with the addition of polarizer optics. These include a linear film polarizer oriented in the direction of polarization of the laser output, and a half-wave plate to controllably rotate the polarization direction of the laser. Also included is a Glan–Thomson (GT) polarizer after the notch filter leg of the optical train, which selects a polarization for the Raman scattered light to be observed at. In order to remove any polarization effects from the spectrometer grating, a quarter–wave plate is also included to convert to circularly polarized light after the GT polarizer.

The instrument allows for co-localised force spectroscopy and polarised Raman spectroscopy measurements for individual FF tubes. Each AFM tip (AC240TS, Asylum) was calibrated for the sensitivity [nm/V] by acquiring a force curve from a clean glass coverslip and linearly fitting the contact region. The spring contact of the cantilever [N/m] was subsequently determined by fitting a Lorentzian curve to the thermal resonance of the tip away from a surface. This calibration allows the voltage setpoint for the AFM to be converted to an equivalent force setpoint. The Raman spectra

were recorded while force measurements were performedŮduring which the tip was kept at the corresponding force setpoint value for 50 s, while the Raman spectra were recorded for 45 s within this time window.

6.3.3 Bending beam experiment

As described by Niu et al., the Young's and shear moduli of a single tube can be determined by pressing sections of a tube at the half-way point of the suspended length L, and calculating the bending modulus

$$\frac{1}{E_b} = 192\frac{\delta I_s}{FL^3} \tag{6.4}$$

from the force F, diameter D, and deflection δ which are all measured by AFM (note: the cross-sectional area A and second moment of area I_s are both functions of D). By balancing the bending moments, the bending modulus can be written in tems of the elastic/Young's modulus and shear modulus as

$$\frac{1}{E_b} = \frac{1}{E} + \frac{48 f_s I_s}{GA}\frac{1}{L^2} \tag{6.5}$$

where f_s is the form factor of the tube (assumed to be 10/9 indicating a circular cross–section.).

For each section of a suspended tube, an AFM image was acquired in order to measure L, D and δ for a fixed value of $F = 60$ nN. The deflection was obtained by finding the difference in the piezo-stage z-position for the same force setpoint (60 nN) between measurements on and away from the midpoint of the suspended tube, as seen in Figure 6.7(c). Effects due to deformation and indentation have been excluded, as these been shown to occur only at sufficiently elevated temperatures.[111] The diameter of the tubes was measured by taking averaged cross–sections at locations where the tube was resting on the copper grid, as shown in figure 6.9.

In order to measure the Young's and shear modulus using equation 6.5,

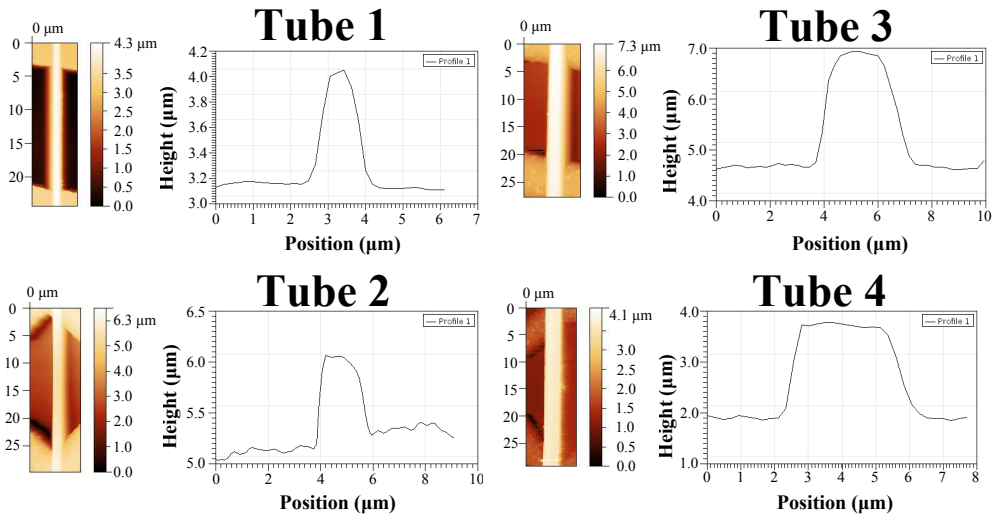

Figure 6.9: Averaged line profiles of the four suspended tubes used in the experiment. The region where the tube is resting on the copper grid were used to measure the averaged line profiles (between 5-10 lines). The diameter of the tubes was taken as the height with respect to the linear baseline of the profiles. In this case, two of the tubes were $\approx$ 800nm, and the other two are $\approx 2\mu$m in diameter.

each tube must be measured at several values of L. Due to the geometry of the $19 \times 19\mu\text{m}^2$ grids, this is limited to a maximum of $\sqrt{2} \times 19\mu\text{m} \approx 27\mu\text{m}$ (for a tube suspended from one corner of the square window to the opposite corner). However, in order to get a range of values for L, the tube should be at an angle to the sides of the grid. Figure 6.10 shows a composite micrograph of Tube 2 suspended across many square windows. The angle is such that L spans a range from 9.7 μm to 25.9 μm, as shown in the AFM topographies accompanying the composite micrograph. Figure 6.10 also shows the force spectra corresponding to the suspended tube segments, with the deflection indicated by a line between the setpoint position of the force spectra at the two tube locations. All force spectra were baseline substracted and offset–adjusted to the contact point. For each location, five repeated force spectra were performed, and the deflection measured as the difference between the average of the setpoint positions. The force spectra in Figure 6.10 are arranged with increasing suspended length, to highlight the expected increase of δ. While shorter suspended segments than S6

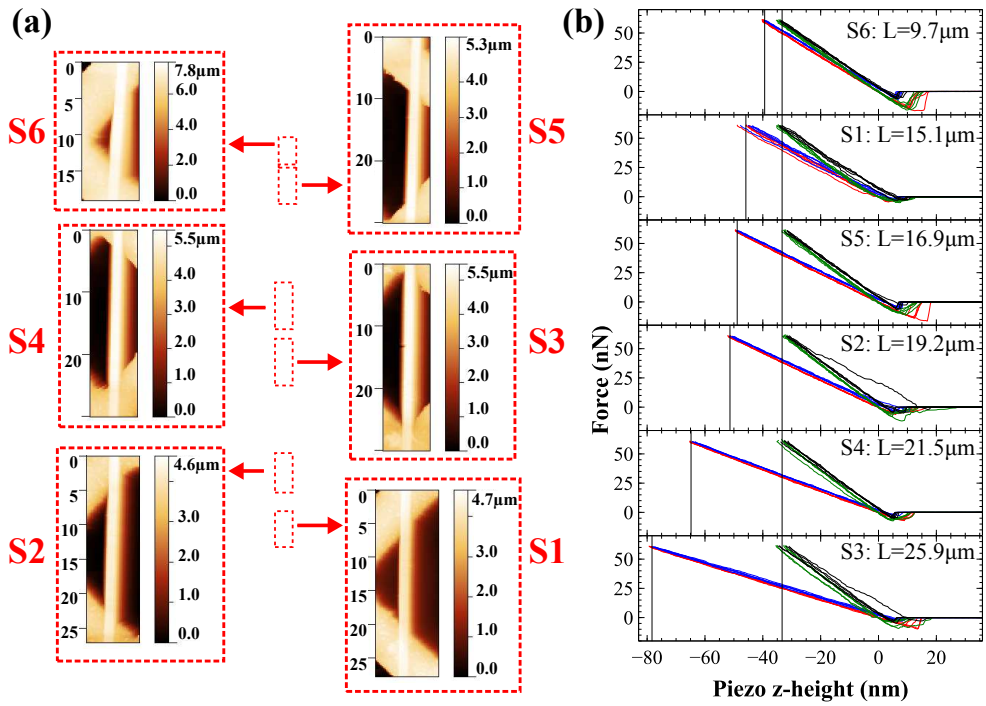

Figure 6.10: Results of the bending beam experiment for an 800nm diameter FF tube (Tube 2 of Figure 6.9) measured at six different segments. On the left, a composite optical micrograph of the tube over a large region of the copper grid with dotted red boxes indicating regions where AFM topographs of suspended segments were obtained. On the right, the accompanying force spectra for the segments where green/black corresponds to the extend/retract curves on the tube over the grid, and red/blue to the extend/retract for the midpoint of the suspended length of tube.)

(9.7μSm) were available, these regions were avoided because the assumption in the bending model that the fixed end is straight and perpendicular to the tube axis is weakened. This can be seen to some degree in all six of the AFM images, most notably in S6 where the length at the edge of the window with the tube in contact becomes comparable to L.

Another example of force spectra are shown in Figure 6.11 for four segments of Tube 3. Here, it can be seen that this particular tube did not vary considerably in length from segment to segment, remaining at roughly 16–17μm, due to the orientation of the tube axis with respect to the grid. It can also be seen that due to the increased diameter of the tube, the applied force is insufficient to measurably deflect the suspended segments, and the

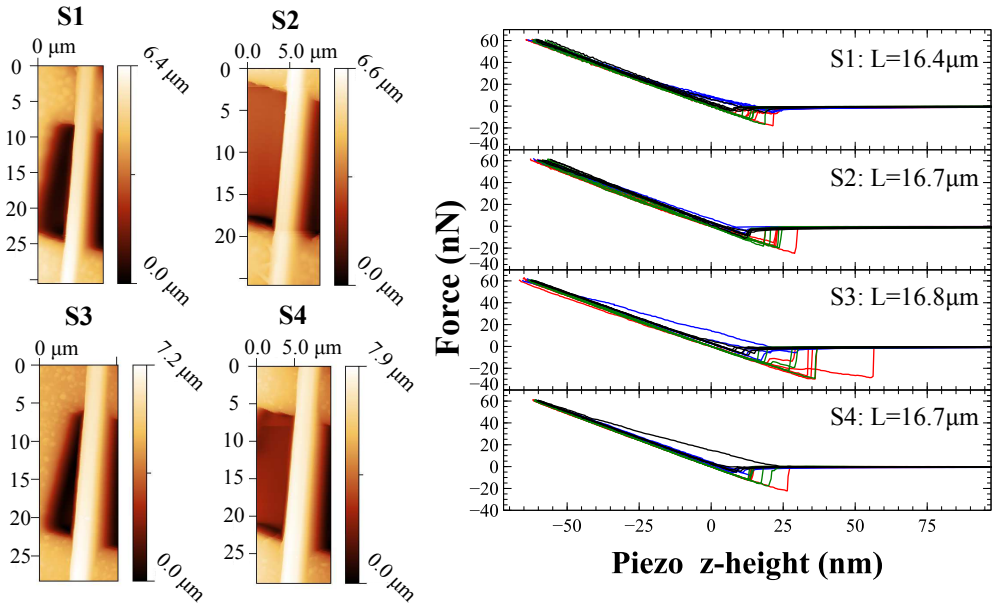

Figure 6.11: Force curves for Tube 3 of Figure 6.9 for four segments ($D \approx 1800$ nm).

force spectra at the midpoint and fixed ends overlap. Similar observations were made for Tube 4. For this reason, measurements of the Young's and shear modulus were not possible for Tubes 3 and 4. For tube 2, the data collected from the bending beam experiments were sufficient to allow plotting $1/E_b$ vs. $1/L^2$, as shown in Figure 6.12. The standard errors for each measurement were calculated by propagating errors in the variables measured by AFM according to equations 6.4 and 6.5. The dominant source of errors was the measurement of D, as the copper TEM grid surface had significant roughness and also the fact that a $D^4 \propto I_s$ term is present in the equations. A linear fit was applied to the data, and the value and standard error for E and G were obtained from the intercept and gradient respectively. The results of $E = 25 \pm 4$ GPa and 0.21 ± 0.01 GPa are in agreement with those of Niu et al[105].

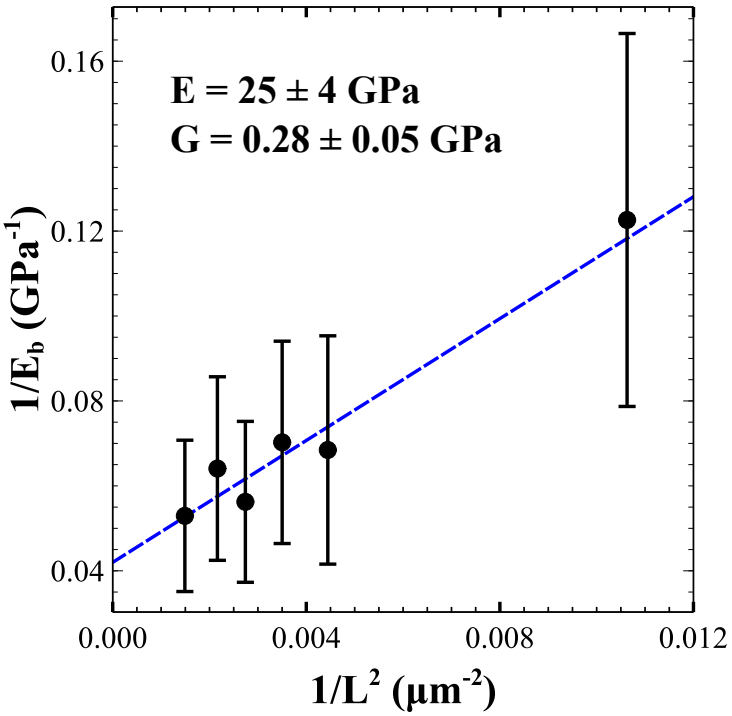

Figure 6.12: Plot of $1/E_b$ vs. $1/L^2$ for the six suspended lengths of the 800nm diameter tube shown in Figure 6.10, with a linear fit (dotted blue line). The inset shows the values of E and G obtained from this data.

6.3.4 Co-localized PRMS-force spectroscopy

Polarized Raman measurements combined with AFM force spectroscopy on suspended tubes is only possible with the clear windows of the TEM grids, allowing access from below in the inverted setup. The grids also fulfil the requirement of being thin enough such that the working distance of a high NA objective is within reach when positioned on a thin quartz coverslip, as shown in the schematic in Figure 6.13. For the combined AFM-Raman force measurement, instead of using a single applied force over many segments, as in the bending beam measurements, only one segment is investigated at various force setpoints. For each of the four tubes in Figure 6.9, polarized spectra in the XX, XZ, ZX and ZZ configurations were obtained, and repeated three times at each value of the force setpoint (twelve total spectra

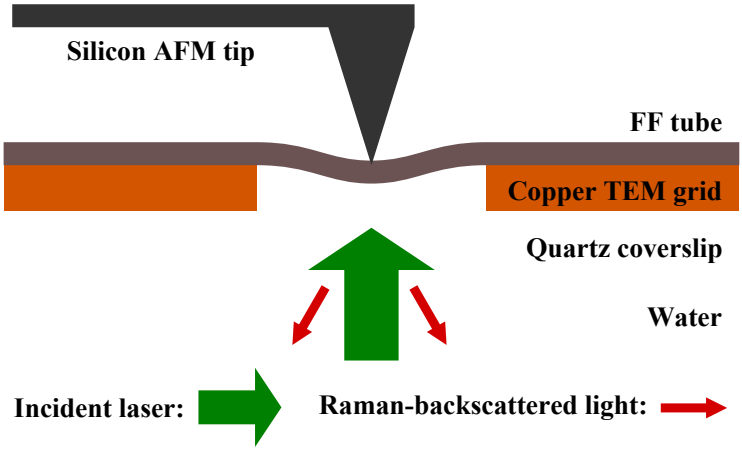

Figure 6.13: Schematic of the co-localized polarized Raman–AFM force spectroscopy experiment. A time delay between the extend and retract portions of the force curve is instigated to allow the acquisition of Raman spectra from the tube being pressed.

at each force). Initially this was done with no force applied, then increasing force in steps of 60 nN, up to 240 nN (with the exception of Tube 1 which was destroyed during the experiment at 180 nN). Figure 6.14 shows the results for the combined experiments on Tube 2 where the tip is held at the setpoint force for the duration of the laser exposure for inducing Raman scattering. The spectra for all tubes were collated and analyzed using principal component analysis for each polarization configuration, the first seven of which are shown in figure 6.15. This was to attempt to observe any subtle changes that may occur in the spectra as a result of bending. The first principal component picks up the large contribution from the silicon Raman peak originating from the AFM tips. Other than regular spectral features, other principal components also show effects due to slight changes in spectrometer grating position (sharp negative/positive features where peaks occur). However, when the reconstructed spectra are displayed against force as seen in Figure 6.14, no changes in spectra could be observed. Higher forces were unable to be used as they were not permitted by the AFM control software. Using the MATLAB functions developed

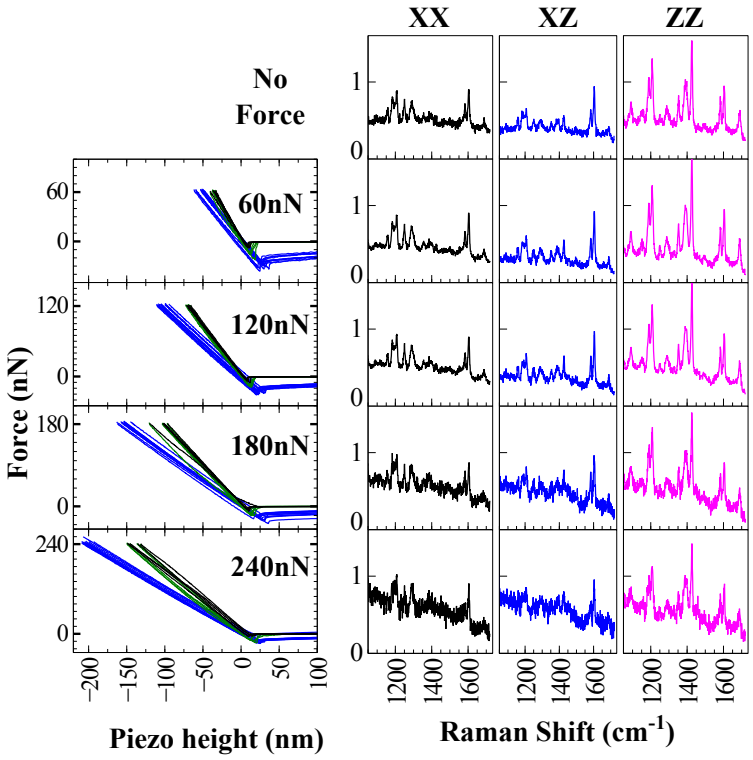

Figure 6.14: Results of the combined polarized Raman–AFM force spectroscopy experiment on Tube 2. Forces from 0–240 nN in intervals of 60 nN were applied to the midpoint of the tube, with corresponding force spectra shown in blue on the left, and reference force spectra in green/black taken at the fixed region of the tube prior to the Raman experiment. On the right, the corresponding normalized principle-component-reconstructed Raman spectra (first seven components used) for different polarization configurations (note: XZ = ZX) are shown for different forces. The amide I (1690 cm^{-1}) and amide III (1249 cm^{-1}) bands are highlighted blue and green respectively.

by B. Lekprasert[1] for the orientation distribution function analysis of FF tubes using the amide I and III Raman modes, the orientation parameters were obtained from the reconstructed spectra and observed as a function of force applied, also showing no trend (not shown).

The lack of any change in the spectra can be understood by considering the relative length scales of the experiment in a simple manner. The suspended length L is of the order 10–30 μm, while δ is typically of the order 10–50 nm. When considering the typical extension from during pressing (assuming the tube is fixed at the grid), the change in length ΔL will be of the order of a few angstroms. As the typical length of an FF unit along the

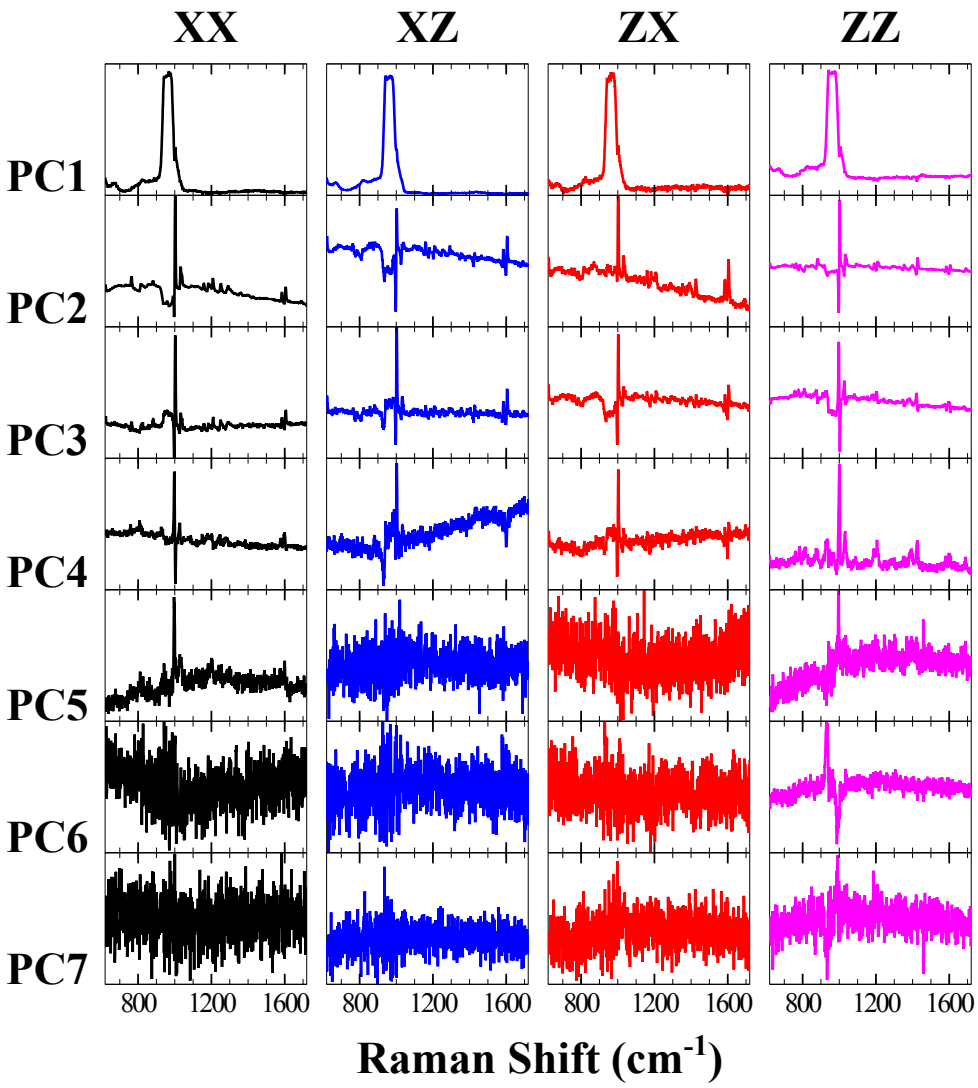

Figure 6.15: Principal components 1–7 for the four polarization configurations of all four FF tubes measured in the co-localized experiment.

tube is ≈ 5 Å, the number of units along L can be estimated (of the order of tens of thousands). Thus the average change in bond length will be of order $\approx 1 \times 10^{-4}$ Å, which is not sufficient to produce shifts in Raman spectra.

6.4 Discussion of the origin of the mechanical strength of FF tubes

6.4.1 Separation of contributions to the Young's modulus in FF tubes

As FF tubes are highly ordered and have a relatively large Young's modulus, they are somewhat unusual compared to other peptide fibrils. While FF tubes are highly ordered crystallites, they still exhibit a peptide structure involving hydrogen bonding and side–chain interactions. DFT modeling of the FF structure using X–Ray data was used by Azuri et. al. to measure the mechanical properties in different symmetry axes of the tubes[100]. It was found that the modulus along the tube axis was significantly larger than that perpendicular to it. The interactions studied the difference in DFT models, with dispersive interactions showing an increase in the moduli in both directions (more fo perpendicular to the tube), thought to be an effect of the "zipper–like" effect of the phenyl interactions.

While the co-localized experiment did not show any Raman spectral changes, the spectra themselves may still be useful for obtaining information about the contributions to bonding strength from Knowles' et al. theory[107], when combined with a knowledge of the structure from X-Ray studies. Figure 6.16 shows the structure of a tube through the cross section (built in Avogadro software using the molecular .xyz files from the supporting information in [100]), with various segments highlighted, each of which will be studied using the theory.

6.4.2 Contribution from backbone interactions

The band assignment for the Raman spectra of FF nanotubes has been reported earlier based on experimental and density functional theory[88].

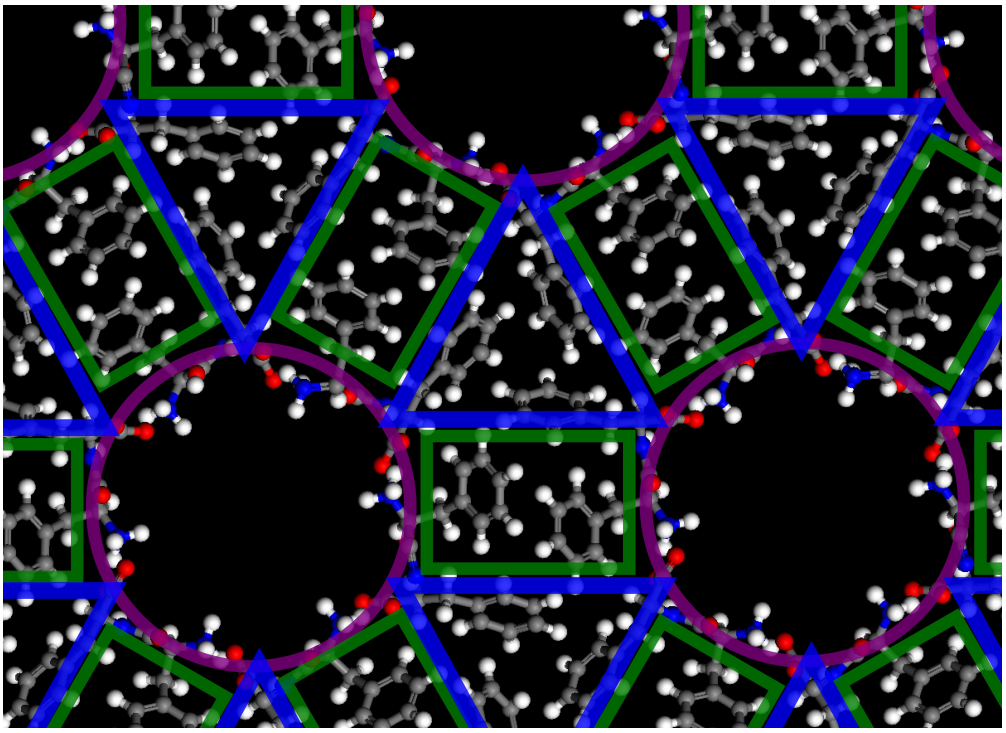

Figure 6.16: Molecular schematic of FF tubes for use with Knowles' theory. The purple segment highlights the peptide backbone region, while the blue triangle and green rectangle regions are the side-chain regions, which have been separated to aid visualization.

In particular, the 1249 cm^{-1} Raman band was assigned to the amide III band, which corresponds to the combination of C-N stretching and N-H in plane bendings.[112,113] The polarization dependence of the amide III band is noticeable in Figure 6.14 as the intensity in the XX configuration is higher than in the ZZ configuration, indicating that the principal axis of the Raman tensor of the amide III vibration is oriented perpendicular to the axis of the nanotubes . The frequency of the amide III band depends on the properties of the backbone, peptide bond, and conformation of peptides (Ramachandran angles) as well as hydrogen bonding at the N-H and C=O. Theoretical studies have showed that hydrogen bonding at N-H site can increase the vibration frequency of the amide III band by ≈22 cm^{-1}. [114] Experimental evidence of blue-shifting of the amide III band upon H

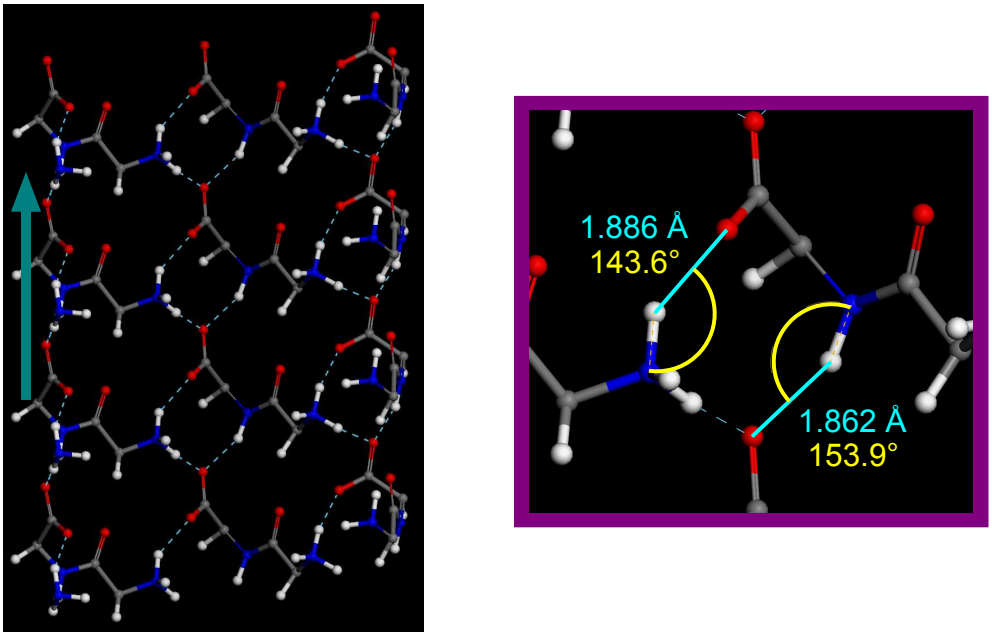

Figure 6.17: Hydrogen bond network schematic. This corresponds to a prism of the purple region highlighted in Figure 6.16 along the tube axis (indicated by arrow). For clarity, the side chains have been removed and the prism bisected along the tube axis.

bonding at the N-H site has been reported, both for α-helical and β-sheet polypeptides. In addition, comparison between experimental and theoretical calculations of the Raman spectra of polypeptides allows the estimation of the force constants corresponding to hydrogen bonds based on the frequency of the amide III band.[108–110] Theoretical calculations showed that for β–sheet polypeptides, such as β-$(\mathrm{Ala})_n$, strong hydrogen bonds (N–H...O angle $\approx$165°, H...O distance $\approx$1.76 Å) led to amide III band at $\approx$1243 cm^{-1}, which corresponds to a force constant of 15 Nm^{-1}.[109,110] A lower frequency of the amide III band in the Raman spectrum of β–$(\mathrm{GlyI})_n$ (1234 cm^{-1}) was correlated with weaker H bonding (N–H...O angle $\approx$134°, H...O distance $\approx$2.12 Å) and a lower value of the force constant of $\approx$12.5 Nm^{-1}. FF tubes have no hydrogen bonds at the C=O sites, therefore the amide III band at 1249 cm^{-1} indicates strong hydrogen bonding corresponding to an estimated force constant of $f_{Am} = 15$ Nm^{-1}. These results agree with the geometrical results obtained from X-ray data for the FF

crystals indicating a N-H...O angle of ≈154° and H...O distance of ≈1.86 Å. The fact that no shifts were observed during the co-localized Raman–force spectroscopy experiment indicates that bending of the FF tubes did not change the force constants associated to the H bonding, suggesting a strong contribution of the H bonding network to the mechanical properties of the tubes. Apart from the hydrogen bonds associated to the N–H sides of the amide bonds, there are an additional six hydrogen bonds per unit cell associated with the head–to–tail interactions NH_3^+...–OOC, as shown in Figure 6.17. Based on the X-ray data of FF crystals, these bonds are characterized by a ≈144° N–H...O angle and ≈1.89 ÅH...O distance, suggesting a lower force constant, of $f_{HT} = 13.87$ Nm^{-1} compared to the hydrogen bonds corresponding the amide bonds. Using these values for the force constants and equation 6.2, the contribution of the hydrogen bonding network to the Young's modulus of FF nano- and micro-tubes can be calculated

$$E_{HB} = f_{Am} h \xi_{Am} + f_{HT} h \xi_{HT} = 17.6\text{GPa} \tag{6.6}$$

where $h = 5.38$ Åis the distance between the ring-like structures of six molecules (or the unit cell along the tube axis), $\xi_{Am} = \xi_{HT} = 6/(23.89 \times 23.89)$ $Å^{-2}$ is the density of the H bonds. This value of ≈ 17.6 GPa for the hydrogen bonding contribution is in close agreement to the theoretically estimated value of ≈ 17 GPa attributed to the back-bone hydrogen bonding network in other cross–β amyloids.[107]

6.4.3 Contribution from side-chain interactions

In addition to hydrogen bonding interactions, interactions between the phenyl rings may also produce a measurable contribution to the elastic modulus. It is known that the benzene dimer can form two distinct stable configurations, commonly termed T–shaped and parallel–offset inter-

actions.[115] Figures 6.18 and 6.19 show the arrangement for the side–chain regions along the FF tube axis. The interactions can be interpreted as combinations of T–shaped and parallel–offset interactions in both groups of phenyl rings.

The interaction strength can be estimated from potential curves for ben-

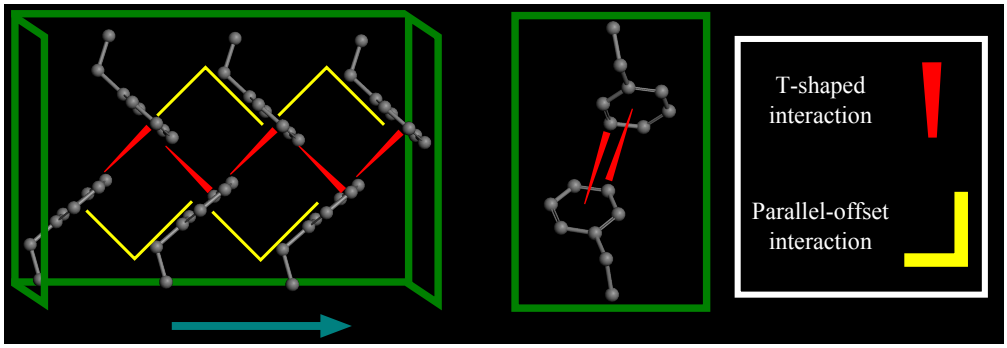

Figure 6.18: Phenyl interaction schematic corresponding to a prism of the green rectangle region highlighted in Figure 6.16 along the tube axis (indicated by arrow). Hydrogen atoms have been omitted for clarity.

zene dimers[116] and using the fact that there are 12 phenyl side chains in the unit cell, 6 in a green box region and 6 in the blue triangular region. For the T–shaped interactions in the green boxed regions, the equilibrium potential and separation (measured from molecular model) are -2.1 kcal mol^{-1} and $h_{T-green} = 5.0$ Å, respectively. Modeling the interaction as a harmonic oscillator gives a spring constant of $f_{T-green} = 0.11$ N m^{-1}. Similarly, for the phenyl rings in the blue triangular regions, the equilibrium potential and separation are -2.6 kcal mol^{-1} and $h_{T-blue} = 4.6$ Å, leading to a force constant of $f_{T-blue} = 0.17$ N m^{-1}.

For the parallel-offset configuration of the phenyl rings, the energy can be estimated using the potential function reported by McGaughey et al. [117], for a centroid distance measured to be $h_{offset} = 5.38$ Å(similar to the green and blue boxed regions). This leads to an energy of -0.4 kcal mol^{-1}, which in turn gives a force constant of $f_{offset} = 0.048$ N m^{-1}.

Using these values, the contribution of the $\pi - \pi$ interactions to the Young's

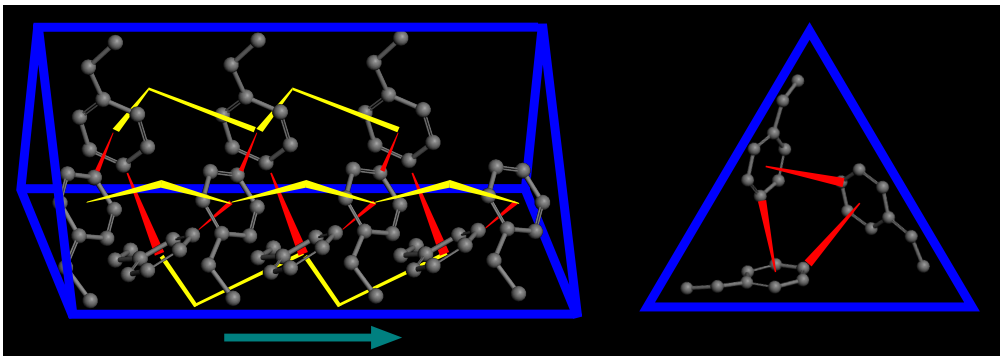

Figure 6.19: Phenyl interaction schematic corresponding to a prism of the blue triangle region highlighted in Figure 6.16 along the tube axis (indicated by arrow). Hydrogen atoms have been omitted for clarity.

modulus is then

$$E_{SC} = \frac{(6h_{T-green}f_{T-green} + 6h_{T-blue}f_{T-blue} + 12h_{offset}f_{offset})}{A} = 0.20\text{GPa} \tag{6.7}$$

where $A = 23.89 \times 23.89$ Åis the area of the unit cell. From the T–shaped interactions, the Young's modulus is 0.15 GPa, and the contribution of the parallel offset interactions is 0.05 GPa, providing a total contribution to the Young's modulus of FF tubes of 0.20 GPa. Knowles et al. estimated the range of the side-chain contributions to the Young's modulus for other cross–β amyloid fibrils using a surface-tension model, which resulted in a range of 0.03–0.13GPa. The value of 0.20GPa calculated here is significantly higher than the upper limit specified for amyloid fibrils. However, this contribution is still almost two orders of magnitude lower than the contributions from the intermolecular hydrogen bonding in FF tubes.

6.4.4 Comparison of calculated and measured FF tube modulus

The estimated Young's modulus of 17.8 GPa from the Knowles' theory is significantly lower than the experimentally measured modulus of 25±4 GPa using the integrated AFM–Raman microscope. Neglecting the anisotropy of the material may cause the bending beam model to give an overestimate

of the Young's modulus, and the calculations of the backbone and side–chain interactions may not take into account all aspects of intermolecular interactions contributing to the elastic moduli, such as, for example, the residual water molecules inside the pores, which simulations have shown to be stabilizing.[118] Table 6.1 shows all values of the Young's modulus

Method	**Elastic modulus (GPa)**
Indentation Kol et al. [104]	19
Bending beam Niu et al. [105]	27 ± 4
DFT theory Azuri et al. [100]	$E_x = 8.75$ $E_z = 15.85$
Bending beam Sinjab et al. [119]	25 ± 4
Knowles theory Sinjab et al. [119]	17.8

Table 6.1: Summary of elastic moduli of FF tubes as measured in various works in the literature, including those measured here (published in [119]).

measured here and in the literature. While the values range from $\approx$ 16–27 GPa, all samples were measured by very different methods and prepared independently in different laboratories. Both values measured by the bending beam model are consistently higher than other values. Indeed, if the bending beam values are omitted, the range reduces significantly to $\approx$ 16–19 GPa, indicating a good agreement.

The DFT and Knowles' theory in particular offer extra information about the anisotropy of the mechanical properties in different ways. From first principles, Azuri et al.'s DFT measurements found the modulus along the tube axis is almost double that perpendicular to it. The value of 17.8 GPa measured here using a simple method with several assumptions about the bonding geometry produces a remarkably close result to this, and also indi-

cated a similar mechanical anisotropy along the tube axis (though differing in relative magnitude).

6.5 Conclusion and future work

This chapter has highlighted the versatility of the combined AFM-PRMS system for studying the mechanical properties of peptide fibrils. Measurements with the AFM, in particular the bending of suspended tubes allowed the Young's and shear moduli to be obtained, while information from Raman spectra of the force constants relating to the hydrogen bonding can be used in conjunction with other X-Ray data and theoretical models to allow not only an estimation of the Young's modulus, but reveal the origin of the mechanical properties at the molecular scale. Co-localized polarized Raman and AFM-force measurements were also possible using this system, so that any potential stress-dependent effects of the Raman spectra can be observed on individual tubes. In the case of the FF tubes, no changes were detected in the fingerprint region of the spectra for forces up to 240 nN. This is due to the small deflections relative to the dimensions of the tube, which while measurable by AFM, do not produce a large enough change in bonding length to affect the positions of the associated Raman peaks.
Difficulty in sample preparation is a major drawback of these experiments yielding a low throughput of samples. The tubes must be isolated, completely suspended on one side of the copper grid and should be long enough such that several suspended segments of different lengths are available for measurements. Even when this is achieved, the size of a tube may be too large or small for force experiments, and the orientation of the tube relative to the grid may result in a low variance between the suspended lengths of the tube. Manipulation of the tubes prior to the experiment may be possible to obtain the desired arrangement, although this may be cumbersome

and risks damaging the tube.

This system could be extended in several ways to try new combined Raman-AFM measurements. The majority of drawbacks mentioned above relate to the preparation of suspended tubes, which are only necessary for bending the tube. Indentation experiments were not used for the co-localized experiment due to the much smaller volume of the tube which would be exerted to these forces compared to the Raman sampling volume. However, force experiments can be performed using a large spherical particle instead of a sharp tip, which increases the contact area at the sample. This may allow for combined Raman measurements without the need to suspend the tube across a grid. Furthermore, the ability to perform Raman mapping whilst putting local stress on a tube may reveal how the pressure is distributed along the tube. This is not possible with the current setup as the stage cannot be moved whilst the tip is in contact with the sample. Nevertheless, several AFM-Raman systems exist on the market which have a separate stage for positioning the microscope objective itself, which could in principle be used for Raman mapping with a tip in contact with the sample. This could also be combined with polarized Raman to observe if the depolarization ratio of particular vibrational modes varies spatially across the tube. Another possibility is to observe the so called "low-wavenumber" ($<200\text{cm}^{-1}$) region of the Raman spectrum, which typically provides information about lower energy intermolecular vibrations. Historically this has been a difficult technique due to the available filter technology, however high–performance modern filters are available now which have cutoff edges less than 10cm^{-1} from the laser line. This allows Raman spectra at energy scales an order of one to two orders of magnitude lower than the vibrations observed in the fingerprint region, such as intermolecular aromatic interactions. FF tubes have not been investigated by low-frequency Raman spectroscopy, and could reveal or confirm details about the interactions between the phenyl

ring side-chains. This may even allow the force constants for these particular side-chain interactions to be obtained experimentally, rather than from DFT–simulated interactions.

7. Conclusions

"... without encroaching upon grounds appertaining to the theologian and the philosopher, the domain of natural sciences is surely broad enough to satisfy the wildest ambition of its devotees. In other departments of human life and interest, true progress is rather an article of faith than a rational belief; but in science a retrograde movement is, from the nature of the case, almost impossible. Increasing knowledge brings with it increasing power, and great as are the triumphs of the present century, we may well believe that they are but a foretaste of what discovery and invention have yet in store for mankind. ... The work may be hard, and the discipline severe; but the interest never fails, and great is the privilege of achievement."

- Excerpt from a speech by Lord Rayleigh in 1884.

The work detailed in this thesis demonstrates the potential of an integrated AFM–Raman spectroscopy instrument for a wide range of different possible experiments on nano– and micro– scale biomaterials. TERS was demonstrated on FF nanotubes for which confocal Raman microspectroscopy was unable to detect any signal (diameter $<$ 100 nm). This was carried out using a novel method for fabricating TERS tips which may have several advantages over current methods, as the tips are prepared *in–situ* via a photochemical reaction. While TERS was possible with such tips, reproducibility was still an issue, though the complexity of the fabrication process was reduced.

The next step investigated pathways to controlling the nanoparticle growth. Photochemical methods capable of producing high yields of decahedral

particles, and thermal methods capable of producing rod particles were investigated, with analysis by TEM and UV-vis spectroscopy. Using light–mediated reactions, highly mono-disperse decahedral particles were produced, but nanorods were unable to be fabriacted by such a reaction. However, rods were produced using an alternative thermal reaction. The different approaches to producing well–characterized nanoparticles for TERS suggest different potential routes for fabricating TERS probes. Instead of directly growing the nanoparticles on a tip in an uncontrolled manner, particles may first be synthesized in solution, where they can be well characterized, and then attached to a tip using chemical surface modification. Preliminary work with Dr. M. Larraona–Puy investigated several such pathways (unpublished).

A different approach to using the combined system was also investigated, aimed at investigating the mechanical properties of FF peptide tubes. A bending beam experiment was performed utilizing the force spectroscopy capabilities of the AFM, allowing the Young's modulus to be estimated. Subsequently a co–localized experiment was carried out where the tube was exerted to various forces from the AFM tip whilst polarized Raman spectra were obtained. The lack of spectral changes with increasing force suggests the range of deflections induced by force spectroscopy measurements are not sufficient to produce the stress needed to cause such changes – an indication of the rigidity of the peptide tubes. Whilst no changes were observed, the data agreed with previous works on polarized Raman spectroscopy of FF tubes used to consolidate the hydrogen bonding structure. This fact was used to estimate the modulus of the FF tubes using a model for amyloid fibril strength, which utilized the Raman spectral data, X–ray structural data from the literature as well as theoretical force fields in the case of the phenyl ring interactions. This allowed a second value for the modulus to be measured, with the addition that the relative contributions

from different interactions could be estimated. It was found that the hydrogen bonding network had a much larger contribution (17.6 GPa) than the phenyl ring side–chains (0.2 GPa), which is in agreement with analysis of other amyloid–β fibrils using the same method. The combined instrument could continue to be developed in several directions, which can be discussed by addressing different sections of the instrument setup. First, the optical setup between the microscope and the Raman spectrometer has the greatest scope for extension, as many removable optical components can be incorporated for a particular desired technique, as demonstrated by PRS.

Low–wavenumber Raman spectroscopy could be incorporated using the latest notch filter technology, allowing spectra to be obtained to below 10 cm^{-1}, a spectral regime offering information related to intermolecular vibrations, as briefly mentioned in the conclusion of chapter 6. This may not only be interesting when applied to the FF tubes, but indeed interesting for studying the intra-particle properties of nanoparticle aggregates[120], which may be useful for further characterization of TERS–relevant nanoparticles, or indeed other nanoparticles in general.

The system could also be modified to incorporate optical tweezing, a field which has recently been combined with Raman spectroscopy, mainly for investigating single cells[121]. While optical tweezing is certainly more restricted regarding the possible samples that could be investigated, the technique is continually developing to incorporate different methods for more general microscale manipulation. Such a technique may also provide complementary mechanical information to that obtained by AFM.

The AFM–PRS system itself could be upgraded, by incorporating stepper–motor control of the two polarizers used allowing software to assign polarization directions, which would allow higher experimental throughput, creating the possibility of fast polarized Raman hyper-spectral imaging.

This would be needed for more complex samples with a range of components aligned in different orientations relative to the lab axis such as fibrils inside biological cells and tissues.

The AFM system used in the integrated system is versatile, and can be used for imaging samples in liquids. This potentially allows studies on live cells with AFM, combined with Raman spectroscopy. These techniques have been applied to cells individually for some time, however their combination has been less utilized. This may allow for more than just combined measurements; AFM could be used to find the topographic profile of the cell and find regions of interest, which are then probed by Raman spectroscopy. This could be taken even further with polarized Raman spectral imaging, where AFM could first be used to find anisotropic features on the surface, and used to assign a lab frame for polarized Raman measurements in the same region. Such an advanced microscopy technique would allow unprecedented detail in the measurement of live cells and their components.

References

[1] B. Lekprasert, *Investigations of the supramolecular structure of individual diphenylalanine nano- and microtubes by polarised Raman microspectroscopy*. PhD thesis, Physics and Astronomy, University of Nottingham, 2012.

[2] M. Diem, *Introduction to modern vibrational spectroscopy*, vol. 543. Wiley New York, 1993.

[3] S. W. Hell, "Far-field optical nanoscopy," *Science*, vol. 316, no. 5828, pp. 1153–1158, 2007.

[4] A. Hartschuh, "Tip-enhanced near-field optical microscopy," *Angewandte Chemie International Edition*, vol. 47, no. 43, pp. 8178–8191, 2008.

[5] B.-S. Yeo, J. Stadler, T. Schmid, R. Zenobi, and W. Zhang, "Tip-enhanced raman spectroscopy - its status, challenges and future directions," *Chemical Physics Letters*, vol. 472, no. 1–3, pp. 1 – 13, 2009.

[6] D. W. Pohl, W. Denk, and M. Lanz, "Optical stethoscopy: Image recording with resolution lambda/20," *Applied Physics Letters*, vol. 44, no. 7, pp. 651–653, 1984.

[7] E. Synge, "Xxxviii. a suggested method for extending microscopic resolution into the ultra-microscopic region," *Philosophical Magazine Series 7*, vol. 6, no. 35, pp. 356–362, 1928.

[8] E. Betzig and J. K. Trautman, "Near-field optics: microscopy, spectroscopy, and surface modification beyond the diffraction limit," *Science*, vol. 257, no. 5067, pp. 189–195, 1992.

[9] A. Dazzi, R. Prazeres, F. Glotin, and J. Ortega, "Local infrared microspectroscopy with subwavelength spatial resolution with an atomic force microscope tip used as a photothermal sensor," *Optics letters*, vol. 30, no. 18, pp. 2388–2390, 2005.

[10] A. Dazzi, R. Prazeres, F. Glotin, and J. Ortega, "Subwavelength infrared spectromicroscopy using an afm as a local absorption sensor," *Infrared physics & technology*, vol. 49, no. 1, pp. 113–121, 2006.

[11] C. Mayet, A. Dazzi, R. Prazeres, F. Allot, F. Glotin, and J. Ortega, "Sub-100 nm ir spectromicroscopy of living cells," *Optics letters*, vol. 33, no. 14, pp. 1611–1613, 2008.

[12] I. Rajapaksa, K. Uenal, and H. K. Wickramasinghe, "Image force microscopy of molecular resonance: A microscope principle," *Applied physics letters*, vol. 97, no. 7, p. 073121, 2010.

[13] I. Rajapaksa and H. K. Wickramasinghe, "Raman spectroscopy and microscopy based on mechanical force detection," *Applied physics letters*, vol. 99, no. 16, p. 161103, 2011.

[14] D. L. Jeanmaire and R. P. Van Duyne, "Surface raman spectroelectrochemistry: Part i. heterocyclic, aromatic, and aliphatic amines adsorbed on the anodized silver electrode," *Journal of Electroanalytical Chemistry and Interfacial Electrochemistry*, vol. 84, no. 1, pp. 1–20, 1977.

[15] J. Wessel, "Surface-enhanced optical microscopy," *J. Opt. Soc. Am. B*, vol. 2, pp. 1538–1541, Sep 1985.

[16] Y. Inouye and S. Kawata, "Near-field scanning optical microscope with a metallic probe tip," *Opt. Lett.*, no. 19, pp. 159–161, 1994.

[17] J. Grausem, B. Humbert, A. Burneau, and J. Oswalt, "Subwavelength raman spectroscopy," *Applied Physics Letters*, vol. 70, no. 13, pp. 1671–1673, 1997.

[18] D. A. Smith, S. Webster, M. Ayad, S. D. Evans, D. Fogherty, and D. Batchelder, "Development of a scanning near-field optical probe for localised raman spectroscopy," *Ultramicroscopy*, vol. 61, no. 1–4, pp. 247 – 252, 1995.

[19] C. L. Jahncke, M. A. Paesler, and H. D. Hallen, "Raman imaging with near-field scanning optical microscopy," *Applied Physics Letters*, vol. 67, no. 17, pp. 2483–2485, 1995.

[20] V. Deckert, D. Zeisel, R. Zenobi, and T. Vo-Dinh, "Near-field surface-enhanced raman imaging of dye-labeled dna with 100-nm resolution," *Analytical Chemistry*, vol. 70, no. 13, pp. 2646–2650, 1998.

[21] R. M. Stöckle, Y. D. Suh, V. Deckert, and R. Zenobi, "Nanoscale chemical analysis by tip-enhanced raman spectroscopy," *Chemical Physics Letters*, vol. 318, no. 1–3, pp. 131 – 136, 2000.

[22] N. Hayazawa, Y. Inouye, Z. Sekkat, and S. Kawata, "Metallized tip amplification of near-field raman scattering," *Optics Communications*, vol. 183, no. 1-4, pp. 333 – 336, 2000.

[23] M. S. Anderson, "Locally enhanced raman spectroscopy with an atomic force microscope," *Applied Physics Letters*, vol. 76, no. 21, pp. 3130–3132, 2000.

[24] T. Deckert-Gaudig and V. Deckert, "Tip-enhanced raman scattering (ters) and high-resolution bio nano-analysis-a comparison," *Phys. Chem. Chem. Phys.*, vol. 12, pp. –, 2010.

[25] M. Sackrow, C. Stanciu, M. A. Lieb, and A. J. Meixner, "Imaging nanometre-sized hot spots on smooth au films with high-resolution tip-enhanced luminescence and raman near-field optical microscopy," *ChemPhysChem*, vol. 9, no. 2, pp. 316–320, 2008.

[26] S. Quabis, R. Dorn, M. Eberler, O. Glöckl, and G. Leuchs, "Focusing light to a tighter spot," *Optics Communications*, vol. 179, no. 1Ű6, pp. 1 – 7, 2000.

[27] K. A. Chan and S. G. Kazarian, "Tip-enhanced raman mapping with top-illumination afm," *Nanotechnology*, vol. 22, no. 17, p. 175701, 2011.

[28] C. Ropers, C. Neacsu, T. Elsaesser, M. Albrecht, M. Raschke, and C. Lienau, "Grating-coupling of surface plasmons onto metallic tips: a nanoconfined light source," *Nano letters*, vol. 7, no. 9, pp. 2784–2788, 2007.

[29] S. Berweger, J. M. Atkin, R. L. Olmon, and M. B. Raschke, "Adiabatic tip-plasmon focusing for nano-raman spectroscopy," *The Journal of Physical Chemistry Letters*, vol. 1, no. 24, pp. 3427–3432, 2010.

[30] S. Kharintsev, G. Hoffmann, A. Fishman, and M. K. Salakhov, "Plasmonic optical antenna design for performing tip-enhanced raman spectroscopy and microscopy," *Journal of Physics D: Applied Physics*, vol. 46, no. 14, p. 145501, 2013.

[31] L. Novotny, "Effective wavelength scaling for optical antennas," *Phys. Rev. Lett.*, vol. 98, p. 266802, Jun 2007.

[32] I. Notingher and A. Elfick, "Effect of sample and substrate electric properties on the electric field enhancement at the apex of spm

nanotips," *The Journal of Physical Chemistry B*, vol. 109, no. 33, pp. 15699–15706, 2005.

[33] W. Zhang, Cui, B.-S. Yeo, T. Schmid, C. Hafner, and R. Zenobi, "Nanoscale roughness on metal surfaces can increase tip-enhanced raman scattering by an order of magnitude," *Nano Letters*, vol. 7, no. 5, pp. 1401–1405, 2007.

[34] D. Roy, J. Wang, and C. Williams, "Novel methodology for estimating the enhancement factor for tip-enhanced raman spectroscopy," *Applied Physics Letters*, vol. 105, no. 1, p. 013530, 2009.

[35] R. L. Agapov, A. V. Malkovskiy, A. P. Sokolov, and M. D. Foster, "Prolonged blinking with ters probes," *The Journal of Physical Chemistry C*, vol. 115, no. 18, pp. 8900–8905, 2011.

[36] W. Zhang, T. Schmid, B.-S. Yeo, and R. Zenobi, "Near-field heating, annealing, and signal loss in tip-enhanced raman spectroscopy," *The Journal of Physical Chemistry C*, vol. 112, no. 6, pp. 2104–2108, 2008.

[37] N. Hayazawa, T.-a. Yano, and S. Kawata, "Highly reproducible tip-enhanced raman scattering using an oxidized and metallized silicon cantilever tip as a tool for everyone," *Journal of Raman Spectroscopy*, vol. 43, no. 9, pp. 1177–1182, 2012.

[38] R. D. Rodriguez, E. Sheremet, S. Muller, O. D. Gordan, A. Villabona, S. Schulze, M. Hietschold, and D. R. T. Zahn, "Compact metal probes: A solution for atomic force microscopy based tip-enhanced raman spectroscopy," *Review of Scientific Instruments*, vol. 83, no. 12, p. 123708, 2012.

[39] J. Lloyd, A. Williams, R. Rickman, A. McCowen, and P. Dunstan, "Reproducible electrochemical etching of silver probes with a radius

of curvature of 20 nm for tip-enhanced raman applications," *Applied Physics Letters*, vol. 99, no. 14, p. 143108, 2011.

[40] B. Pettinger, B. Ren, G. Picardi, R. Schuster, and G. Ertl, "Nanoscale probing of adsorbed species by tip-enhanced raman spectroscopy," *Phys. Rev. Lett.*, vol. 92, p. 096101, Mar 2004.

[41] J. Stadler, T. Schmid, L. Opilik, P. Kuhn, P. S. Dittrich, and R. Zenobi, "Tip-enhanced raman spectroscopic imaging of patterned thiol monolayers," *Beilstein Journal of Nanotechnology*, vol. 2, pp. 509–515, 2011.

[42] A. Hartschuh, E. J. Sánchez, X. S. Xie, and L. Novotny, "High-resolution near-field raman microscopy of single-walled carbon nanotubes," *Phys. Rev. Lett.*, vol. 90, p. 095503, Mar 2003.

[43] E. Bailo and V. Deckert, "Tip-enhanced raman spectroscopy of single rna strands: Towards a novel direct-sequencing method," *Angewandte Chemie International Edition*, vol. 47, no. 9, pp. 1658–1661, 2008.

[44] R. Zhang, Y. Zhang, Z. Dong, S. Jiang, C. Zhang, L. Chen, L. Zhang, Y. Liao, J. Aizpurua, Y. Luo, *et al.*, "Chemical mapping of a single molecule by plasmon-enhanced raman scattering," *Nature*, vol. 498, no. 7452, pp. 82–86, 2013.

[45] N. Hayazawa, T. Yano, H. Watanabe, Y. Inouye, and S. Kawata, "Detection of an individual single-wall carbon nanotube by tip-enhanced near-field raman spectroscopy," *Chemical Physics Letters*, vol. 376, no. 1-2, pp. 174 – 180, 2003.

[46] K. A. Chan and S. G. Kazarian, "Finding a needle in a chemical haystack: tip-enhanced raman scattering for studying carbon nanotubes mixtures," *Nanotechnology*, vol. 21, no. 44, p. 445704, 2010.

[47] R. Rickman and P. Dunstan, "Enhancement of lattice defect signatures in graphene and ultrathin graphite using tip-enhanced raman spectroscopy," *Journal of Raman Spectroscopy*, vol. 45, no. 1, pp. 15–21, 2014.

[48] J. Chen, W. Yang, K. Dick, K. Deppert, H. Q. Xu, L. Samuelson, and H. Xu, "Tip-enhanced raman scattering of p-thiocresol molecules on individual gold nanoparticles," *Applied Physics Letters*, vol. 92, no. 9, p. 093110, 2008.

[49] B.-S. Yeo, E. Amstad, T. Schmid, J. Stadler, and R. Zenobi, "Nanoscale probing of a polymer-blend thin film with tip-enhanced raman spectroscopy," *Small*, vol. 5, no. 8, pp. 952–960, 2009.

[50] C. Budich, U. Neugebauer, J. Popp, and V. Deckert, "Cell wall investigations utilizing tip-enhanced raman scattering," *Journal of Microscopy*, vol. 229, no. 3, pp. 533–539, 2008.

[51] B. R. Wood, E. Bailo, M. A. Khiavi, L. Tilley, S. Deed, T. Deckert-Gaudig, D. McNaughton, and V. Deckert, "Tip-enhanced raman scattering (ters) from hemozoin crystals within a sectioned erythrocyte," *Nano Letters*, vol. 11, no. 5, pp. 1868–1873, 2011.

[52] D. Cialla, T. Deckert-Gaudig, C. Budich, M. Laue, R. MÃűller, D. Naumann, V. Deckert, and J. Popp, "Raman to the limit: tip-enhanced raman spectroscopic investigations of a single tobacco mosaic virus," *Journal of Raman Spectroscopy*, vol. 40, no. 3, pp. 240–243, 2009.

[53] C. Gullekson, L. Lucas, K. Hewitt, and L. Kreplak, "Surface-sensitive raman spectroscopy of collagen i fibrils," *Biophysical Journal*, vol. 100, p. 1837, APR 6 2011.

[54] D. Kurouski, T. Deckert-Gaudig, V. Deckert, and I. K. Lednev, "Structure and composition of insulin fibril surfaces probed by ters," *Journal of the American Chemical Society*, vol. 134, no. 32, pp. 13323–13329, 2012.

[55] L. Opilik, T. Bauer, T. Schmid, J. Stadler, and R. Zenobi, "Nanoscale chemical imaging of segregated lipid domains using tip-enhanced raman spectroscopy," *Phys. Chem. Chem. Phys.*, vol. 13, pp. –, 2011.

[56] N. Kazemi-Zanjani, H. Chen, H. A. Goldberg, G. K. Hunter, B. Grohe, and F. Lagugné-Labarthet, "Label-free mapping of osteopontin adsorption to calcium oxalate monohydrate crystals by tip-enhanced raman spectroscopy," *Journal of the American Chemical Society*, vol. 134, no. 41, pp. 17076–17082, 2012.

[57] C. Blum, L. Opilik, J. M. Atkin, K. Braun, S. B. Kämmer, V. Kravtsov, N. Kumar, S. Lemeshko, J.-F. Li, K. Luszcz, *et al.*, "Tip-enhanced raman spectroscopy–an interlaboratory reproducibility and comparison study," *Journal of Raman Spectroscopy*, vol. 45, no. 1, pp. 22–31, 2014.

[58] H. Atwater, "The promise of plasmonics," *Scientific American*, vol. 296, pp. 56–62, 2007.

[59] M. Faraday, "The bakerian lecture: Experimental relations of gold (and other metals) to light," *Philosophical Transactions of the Royal Society of London*, vol. 147, pp. 145–181, 1857.

[60] G. Mie, "Contributions on the optics of turbid media, particularly colloidal metal solutions, (1978 translation by patricia newman at sandia national lab, new mexico)," *Annalen der Physik*, vol. 330, no. 3, pp. 377–445, 1908.

[61] E. C. Le Ru and P. G. Etchegoin, *Principles of Surface-Enhanced Raman Spectroscopy and related plasmonic effects*. Elsevier, 2009.

[62] M. Rycenga, C. M. Cobley, J. Zeng, W. Li, C. H. Moran, Q. Zhang, D. Qin, and Y. Xia, "Controlling the synthesis and assembly of silver nanostructures for plasmonic applications," *Chemical Reviews*, vol. 111, no. 6, pp. 3669–3712, 2011.

[63] Y. Xia, Y. Xiong, B. Lim, and S. Skrabalak, "Shape-controlled synthesis of metal nanocrystals: Simple chemistry meets complex physics?," *Angewandte Chemie International Edition*, vol. 48, no. 1, pp. 60–103, 2009.

[64] L. Marks, "Surface structure and energetics of multiply twinned particles," *Philosophical Magazine A*, vol. 49, no. 1, pp. 81–93, 1984.

[65] A. Howie and L. Marks, "Elastic strains and the energy balance for multiply twinned particles," *Philosophical Magazine A*, vol. 49, no. 1, pp. 95–109, 1984.

[66] A. R. Tao, S. Habas, and P. Yang, "Shape control of colloidal metal nanocrystals," *Small*, vol. 4, no. 3, pp. 310–325, 2008.

[67] Y. Sun, B. Mayers, T. Herricks, and Y. Xia, "Polyol synthesis of uniform silver nanowires: a plausible growth mechanism and the supporting evidence," *Nano Letters*, vol. 3, no. 7, pp. 955–960, 2003.

[68] B. Pietrobon and V. Kitaev, "Photochemical synthesis of monodisperse size-controlled silver decahedral nanoparticles and their remarkable optical properties," *Chemistry of Materials*, vol. 20, no. 16, pp. 5186–5190, 2008.

[69] B. Pietrobon, M. McEachran, and V. Kitaev, "Synthesis of size-controlled faceted pentagonal silver nanorods with tunable plasmonic

properties and self-assembly of these nanorods," *ACS nano*, vol. 3, no. 1, pp. 21–26, 2008.

[70] X. Zheng, X. Zhao, D. Guo, B. Tang, S. Xu, B. Zhao, W. Xu, and J. R. Lombardi, "Photochemical formation of silver nanodecahedra: structural selection by the excitation wavelength," *Langmuir*, vol. 25, no. 6, pp. 3802–3807, 2009.

[71] J. Zhang, M. R. Langille, and C. A. Mirkin, "Synthesis of silver nanorods by low energy excitation of spherical plasmonic seeds," *Nano letters*, vol. 11, no. 6, pp. 2495–2498, 2011.

[72] G. Turrell, "Analysis of polarization measurements in raman microspectroscopy," *Journal of Raman spectroscopy*, vol. 15, no. 2, pp. 103–108, 1984.

[73] D. Long, *The Raman effect*. John Wiley & Sons Ltd, 2002.

[74] L. Novotny and B. Hecht, *Principles of Nano-Optics*. Cambridge University Press, 2006.

[75] M. Fox, *Optical Properties of Solids, 2nd Edition*. Oxford Publishing, 2010.

[76] E. Ringe, M. R. Langille, K. Sohn, J. Zhang, J. Huang, C. A. Mirkin, R. P. Van Duyne, and L. D. Marks, "Plasmon length: A universal parameter to describe size effects in gold nanoparticles," *The Journal of Physical Chemistry Letters*, vol. 3, no. 11, pp. 1479–1483, 2012.

[77] G. Binnig, C. F. Quate, and C. Gerber, "Atomic force microscope," *Physical review letters*, vol. 56, no. 9, pp. 930–933, 1986.

[78] R. Jin, Y. Cao, C. A. Mirkin, K. Kelly, G. C. Schatz, and J. Zheng, "Photoinduced conversion of silver nanospheres to nanoprisms," *Science*, vol. 294, no. 5548, pp. 1901–1903, 2001.

[79] R. Jin, Y. C. Cao, E. Hao, G. S. Métraux, G. C. Schatz, and C. A. Mirkin, "Controlling anisotropic nanoparticle growth through plasmon excitation," *Nature*, vol. 425, no. 6957, pp. 487–490, 2003.

[80] M. Maillard, P. Huang, and L. Brus, "Silver nanodisk growth by surface plasmon enhanced photoreduction of adsorbed [ag+]," *Nano Letters*, vol. 3, no. 11, pp. 1611–1615, 2003.

[81] E. J. Bjerneld, K. V. G. K. Murty, J. Prikulis, and M. Käll, "Laser-induced growth of ag nanoparticles from aqueous solutions," *ChemPhysChem*, vol. 3, no. 1, pp. 116–119, 2002.

[82] E. J. Bjerneld, F. Svedberg, and M. Käll, "Laser-induced growth and deposition of noble-metal nanoparticles for surface-enhanced raman scattering," *Nano Letters*, vol. 3, no. 5, pp. 593–596, 2003.

[83] X. Wu, P. L. Redmond, H. Liu, Y. Chen, M. Steigerwald, and L. Brus, "Photovoltage mechanism for room light conversion of citrate stabilized silver nanocrystal seeds to large nanoprisms," *Journal of the American Chemical Society*, vol. 130, no. 29, pp. 9500–9506, 2008.

[84] C. Munro, W. Smith, M. Garner, J. Clarkson, and P. White, "Characterization of the surface of a citrate-reduced colloid optimized for use as a substrate for surface-enhanced resonance raman scattering," *Langmuir*, vol. 11, no. 10, pp. 3712–3720, 1995.

[85] R. G. Freeman, K. C. Grabar, K. J. Allison, R. M. Bright, J. A. Davis, A. P. Guthrie, M. B. Hommer, M. A. Jackson, P. C. Smith, D. G. Walter, and M. J. Natan, "Self-assembled metal colloid monolayers: An approach to sers substrates," *Science*, vol. 267, no. 5204, pp. 1629–1632, 1995.

[86] T. Umakoshi, T.-a. Yano, Y. Saito, and P. Verma, "Fabrication of near-field plasmonic tip by photoreduction for strong enhancement in tip-enhanced raman spectroscopy," *Applied Physics Express*, vol. 5, no. 5, p. 2001, 2012.

[87] B. Lekprasert, V. Sedman, C. J. Roberts, S. J. Tedler, and I. Notingher, "Nondestructive raman and atomic force microscopy measurement of molecular structure for individual diphenylalanine nanotubes," *Optics letters*, vol. 35, no. 24, pp. 4193–4195, 2010.

[88] B. Lekprasert, V. Korolkov, A. Falamas, V. Chis, C. J. Roberts, S. J. Tendler, and I. Notingher, "Investigations of the supramolecular structure of individual diphenylalanine nano-and microtubes by polarized raman microspectroscopy," *Biomacromolecules*, vol. 13, no. 7, pp. 2181–2187, 2012.

[89] C. S. Sweetenham and I. Notingher, "Combined atomic force microscopy-raman mapping of electric field enhancement and surface-enhanced raman scattering hot-spots for nanosphere lithography substrates," *Journal of Nanophotonics*, vol. 5, no. 1, pp. 059504–059504, 2011.

[90] W. Zhang, X. Cui, B.-S. Yeo, T. Schmid, C. Hafner, and R. Zenobi, "Nanoscale roughness on metal surfaces can increase tip-enhanced raman scattering by an order of magnitude," *Nano letters*, vol. 7, no. 5, pp. 1401–1405, 2007.

[91] T. Deckert-Gaudig, E. Rauls, and V. Deckert, "Aromatic amino acid monolayers sandwiched between gold and silver: A combined tip-enhanced raman and theoretical approachĘ," *The Journal of Physical Chemistry C*, vol. 114, no. 16, pp. 7412–7420, 2009.

[92] C. Blum, T. Schmid, L. Opilik, N. Metanis, S. Weidmann, and R. Zenobi, "Missing amide i mode in gap-mode tip-enhanced raman spectra of proteins," *The Journal of Physical Chemistry C*, vol. 116, no. 43, pp. 23061–23066, 2012.

[93] A.-I. Henry, J. M. Bingham, E. Ringe, L. D. Marks, G. C. Schatz, and R. P. Van Duyne, "Correlated structure and optical property studies of plasmonic nanoparticles," *The Journal of Physical Chemistry C*, vol. 115, no. 19, pp. 9291–9305, 2011.

[94] R. Sperling and W. Parak, "Surface modification, functionalization and bioconjugation of colloidal inorganic nanoparticles," *Philosophical Transactions of the Royal Society A: Mathematical, Physical and Engineering Sciences*, vol. 368, no. 1915, pp. 1333–1383, 2010.

[95] S. C. Lovell, I. W. Davis, W. B. Arendall, P. I. de Bakker, J. M. Word, M. G. Prisant, J. S. Richardson, and D. C. Richardson, "Structure validation by cα geometry: ϕ, ψ and cβ deviation," *Proteins: Structure, Function, and Bioinformatics*, vol. 50, no. 3, pp. 437–450, 2003.

[96] J. D. Sipe, M. D. Benson, J. N. Buxbaum, S.-I. Ikeda, G. Merlini, M. J. Saraiva, and P. Westermark, "Amyloid fibril protein nomenclature: 2010 recommendations from the nomenclature committee of the international society of amyloidosis," *Amyloid*, vol. 17, no. 3-4, pp. 101–104, 2010.

[97] E. Gazit, "A possible role for π-stacking in the self-assembly of amyloid fibrils," *The FASEB Journal*, vol. 16, no. 1, pp. 77–83, 2002.

[98] X. Yan, P. Zhu, and J. Li, "Self-assembly and application of diphenylalanine-based nanostructures," *Chemical Society Reviews*, vol. 39, no. 6, pp. 1877–1890, 2010.

[99] C. H. Görbitz, "The structure of nanotubes formed by diphenylalanine, the core recognition motif of alzheimer's β-amyloid polypeptide," *Chemical communications*, no. 22, pp. 2332–2334, 2006.

[100] I. Azuri, L. Adler-Abramovich, E. Gazit, O. Hod, and L. Kronik, "Why are diphenylalanine-based peptide nanostructures so rigid? insights from first principles calculations," *Journal of the American Chemical Society*, vol. 136, no. 3, pp. 963–969, 2014.

[101] M. Reches and E. Gazit, "Casting metal nanowires within discrete self-assembled peptide nanotubes," *Science*, vol. 300, no. 5619, pp. 625–627, 2003.

[102] V. Jayawarna, M. Ali, T. A. Jowitt, A. F. Miller, A. Saiani, J. E. Gough, and R. V. Ulijn, "Nanostructured hydrogels for three-dimensional cell culture through self-assembly of fluorenylmethoxycarbonyl–dipeptides," *Advanced Materials*, vol. 18, no. 5, pp. 611–614, 2006.

[103] X. Yan, Q. He, K. Wang, L. Duan, Y. Cui, and J. Li, "Transition of cationic dipeptide nanotubes into vesicles and oligonucleotide delivery," *Angewandte Chemie*, vol. 119, no. 14, pp. 2483–2486, 2007.

[104] N. Kol, L. Adler-Abramovich, D. Barlam, R. Z. Shneck, E. Gazit, and I. Rousso, "Self-assembled peptide nanotubes are uniquely rigid bioinspired supramolecular structures," *Nano letters*, vol. 5, no. 7, pp. 1343–1346, 2005.

[105] L. Niu, X. Chen, S. Allen, and S. J. Tendler, "Using the bending beam model to estimate the elasticity of diphenylalanine nanotubes," *Langmuir*, vol. 23, no. 14, pp. 7443–7446, 2007.

[106] J. Gere and S. Timoshenko, "Mechanics of materials. brooks," *Cole Pacific Grove, CA*, 2001.

[107] T. P. Knowles, A. W. Fitzpatrick, S. Meehan, H. R. Mott, M. Vendruscolo, C. M. Dobson, and M. E. Welland, "Role of intermolecular forces in defining material properties of protein nanofibrils," *Science*, vol. 318, no. 5858, pp. 1900–1903, 2007.

[108] W. H. Moore and S. Krimm, "Vibrational analysis of peptides, polypeptides, and proteins. i. polyglycine i," *Biopolymers*, vol. 15, no. 12, pp. 2439–2464, 1976.

[109] W. H. Moore and S. Krimm, "Vibrational analysis of peptides, polypeptides, and proteins. ii. β-poly (l-alanine) and β-poly (l-alanylglycine)," *Biopolymers*, vol. 15, no. 12, pp. 2465–2483, 1976.

[110] J. Rabolt, W. Moore, and S. Krimm, "Vibrational analysis of peptides, polypeptides, and proteins. 3. α-poly (l-alanine)," *Macromolecules*, vol. 10, no. 5, pp. 1065–1074, 1977.

[111] V. L. Sedman, L. Adler-Abramovich, S. Allen, E. Gazit, and S. J. Tendler, "Direct observation of the release of phenylalanine from diphenylalanine nanotubes," *Journal of the American Chemical Society*, vol. 128, no. 21, pp. 6903–6908, 2006.

[112] S. A. Asher, A. Ianoul, G. Mix, M. N. Boyden, A. Karnoup, M. Diem, and R. Schweitzer-Stenner, "Dihedral ψ angle dependence of the amide iii vibration: A uniquely sensitive uv resonance raman secondary structural probe," *Journal of the American Chemical Society*, vol. 123, no. 47, pp. 11775–11781, 2001.

[113] A. V. Mikhonin, S. V. Bykov, N. S. Myshakina, and S. A. Asher, "Peptide secondary structure folding reaction coordinate: Correlation

between uv raman amide iii frequency, ψ ramachandran angle, and hydrogen bonding," *The Journal of Physical Chemistry B*, vol. 110, no. 4, pp. 1928–1943, 2006.

[114] N. S. Myshakina, Z. Ahmed, and S. A. Asher, "Dependence of amide vibrations on hydrogen bonding," *The Journal of Physical Chemistry B*, vol. 112, no. 38, pp. 11873–11877, 2008.

[115] C. A. Hunter and J. K. Sanders, "The nature of. pi.-. pi. interactions," *Journal of the American Chemical Society*, vol. 112, no. 14, pp. 5525–5534, 1990.

[116] M. O. Sinnokrot and C. D. Sherrill, "Highly accurate coupled cluster potential energy curves for the benzene dimer: sandwich, t-shaped, and parallel-displaced configurations," *The Journal of Physical Chemistry A*, vol. 108, no. 46, pp. 10200–10207, 2004.

[117] G. B. McGaughey, M. Gagné, and A. K. Rappé, "π-stacking interactions alive and well in proteins," *Journal of Biological Chemistry*, vol. 273, no. 25, pp. 15458–15463, 1998.

[118] C. Guo, Y. Luo, R. Zhou, and G. Wei, "Probing the self-assembly mechanism of diphenylalanine-based peptide nanovesicles and nanotubes," *ACS nano*, vol. 6, no. 5, pp. 3907–3918, 2012.

[119] F. Sinjab, G. Bondakov, and I. Notingher, "Co-localised raman and force spectroscopy reveal the roles of hydrogen bonds and π-π interactions in defining the mechanical properties of diphenylalanine nano- and micro-tubes," *Applied Physics Letters*, vol. 104, no. 25, p. 251905, 2014.

[120] A. Courty, A. Mermet, P. Albouy, E. Duval, and M. Pileni, "Vibrational coherence of self-organized silver nanocrystals in fcc supracrystals," *Nature materials*, vol. 4, no. 5, pp. 395–398, 2005.

[121] C. Xie, M. A. Dinno, and Y.-q. Li, "Near-infrared raman spectroscopy of single optically trapped biological cells," *Optics letters*, vol. 27, no. 4, pp. 249–251, 2002.